Quasiclassical approach to low-dimensional topological insulators and superconductors

Inaugural-Dissertation

zur

Erlangung des Doktorgrades

der Mathematisch-Naturwissenschaftlichen Fakultät

der Universität zu Köln

vorgelegt von

Patrick Neven

aus Köln

Köln 2015

Berichterstatter: Prof. Dr. Alexander Altland

Priv.-Doz. Dr. Rochus Klesse

Tag der mündlichen Prüfung: 19. 06. 2015

Für Willi

Abstract

In this work we apply the quasiclassical formalism, an established tool in the context of superconducting heterostructures, to topological insulators and superconductors in one and two dimensions, with focus on the former. We derive topological invariants in terms of the quasiclassical Green's function in the regions terminating the disordered one-dimensional wire geometries, and demonstrate the existence of edge modes in the corresponding topologically non-trivial phases. A generalisation to two-dimensional geometries is established by the concepts of compactification and dimensional reduction. The second part of this work is devoted to Majorana fermions in disordered topological quantum wires. We apply the quasiclassical approach developed in the first part of this work to a setup used in recent experiments, where the evidence for Majorana edge modes is drawn from zero-bias peaks in tunnelling experiments. Analytically we derive a formalism that lays the foundation for an efficient numerical method to calculate physical observables. Studying in particular the averaged local density of states, we show that effects arising from disorder may overshadow an unambiguous detection of Majorana edge modes in tunnelling experiments. In the last part of this work we briefly discuss ongoing research on how disorder effects in one-dimensional quantum wires may actually lead to the formation of local topological domains and may stabilise these domains. Based on the numerical method introduced in the second part, we present results that point towards formation of such local domains.

Kurzzusammenfassung

Diese Arbeit beschäftigt sich mit der quasiklassischen Beschreibung – eine bewährte Methodik in der Analyse supraleitender Heterostrukturen – von topologischen Isolatoren und Supraleitern in einer und zwei Dimensionen mit dem Fokus auf eindimensionale Systeme. Wir geben topologische Invarianten in Abhängigkeit der quasiklassischen Greenschen Funktion der Endpunkte des ungeordneten Drahtes. Ferner wird die Existenz von Randmoden in den korrespondierenden topologisch nichttrivialen Phasen bewiesen. Eine Verallgemeinerung für zweidimensionale Geometrien gelingt wird mittels Dimensionsreduktion. Der zweite Teil dieser Arbeit ist Majoranafermionen in ungeordneten topologischen Quantendrähten gewidmet. Wir wenden den im ersten Kapitel erarbeiteten Formalismus auf ein System an, welches kürzlich experimentell realisiert wurde. In entsprechendem Experiment wurde die Existenz von Majoranafermionen anhand von Leitfähigkeitsspitzen in Tunnelexperimenten nachgewiesen. Wir leiten eine analytische Theorie her, die Grundlage für eine effiziente numerische Berechnung von physikalischen Observablen darstellt. Insbesondere berechnen wir die gemittelte, lokale Zustandsdichte und zeigen, dass Unordnungseffekte die eindeutige Identifizierung von Majoranafermionen in Tunnelexperimenten erschweren können. Im letzten Teil dieser Arbeit diskutieren wir kurz die Resultate einer noch andauernden Untersuchung der Formation lokaler topologischer Domänen in Quantendrähten, hervorgerufen durch Unordnung. Auch die mögliche unordnungsbedingte Stabilisierung dieser Domänen wird diskutiert und mit dem numerischen Verfahren, das im zweiten Teil dieser Arbeit präsentiert wird, untersucht.

Contents

—You know I always wanted to pretend I was an architect.

George Costanza

Introduction

Topological order in condensed matter physics presents a new kind of order for characterising phases of matter. Such phases are described by a global quantity independent of details of the system and are therefore not described within Landaus symmetry-breaking theory. Originating from a ground-breaking work by Thouless *et al.* [1] in 1982 explaining the integer quantum Hall effect, topological order has become a very important concept of modern condensed matter theory. The study of insulators with topological order, called topological insulators, is a particularly interesting and very active field of research, [2, 3]. An immediate consequence of the topological order in an insulating system is the presence of gapless edge modes. So while the system is an insulator, i.e. there exists an energy gap that separates the valence band from the conduction band, the surface (or edge) of this insulator shows metallic behaviour. The fact that these effects are of topological origin, and as such are insensitive to local perturbations, ensures their stability. Topological insulators are classified by a topological index which distinguishes insulating phases that are not equivalent, i.e. which cannot be continuously deformed into one another without destroying its defining property, namely the bulk gap. The existence of topological insulators in a given dimension depends on the symmetries present. They are grouped by symmetries according to the Altland-Zirnbauer (AZ) classification, [4]. It turns out that in each dimension, in five of the ten AZ symmetry classes, topological insulators or superconductors can exist, [3, 5]. For a long time, the presence of time-reversal symmetry in a system was believed to prohibit the possibility to construct a topological insulator. And it was only in 2005 when Kane and Mele, [6, 7] showed that a new type of topological phase can be achieved in the presence of time-reversal symmetry. In two dimensions, this new phase is characterised by helical pairs of edge modes propagating on the boundary of the system. Known as the quantum spin Hall effect, this effect was experimentally observed in 2007, [8]. The concept of topological order was naturally extended to superconductors, described by Bogoliubov-de Gennes Hamiltonians, [9]. This extension is based on the fact that the quasi-particle spectrum is gapped by the superconducting pairing. Boundary modes in topological superconductors are Majorana particles, i.e. particles that are their own anti-particles, [10]. These quasi-particles are bound to zero-energy and due to their highly non-local nature, are among the most promising candidates for topological quantum computing, [11]. Very recent experiments claimed the observation of such Majorana fermions in spin-orbit coupled quantum wires in proximity to an s-wave superconductor and subjected to a magnetic field, [12, 13]. These quantum wires are predicted to host Majorana fermions localised at their ends, [14, 15]. Understanding these wires is critical in identifying Majorana fermions and will be a central topic of this thesis.

In chapter one and three, we review the basic concepts topological insulator and super-conductors as well as the emergence of Majorana fermions in condensed matter systems. In the second chapter we investigate topological insulators in one and two dimensions from a quasiclassical point of view. The quasiclassical technique is a well-established tool in the description of mesoscopic superconductivity, [16–18]. By identifying the relevant information needed to describe the phenomena under investigation, and a subsequent removal of the complementary information, the quasiclassical approach drastically simplifies the involved transport equations. With the characteristic length scales of a superconductor exceeding the Fermi wavelength, the quasiclassical approach confines the Green's functions to a regime close to the Fermi points by integrating out higher energies. The quasiclassical approach used in this work relies on the fact that close to a topological phase transition, topological insulators and superconductors can be described by a Dirac Hamiltonian which is linear in momentum. We consider disordered one-dimensional quantum wires connected to two topological insulators or superconductors. We present topological invariants for all five symmetry classes in one dimension and determine the number of zero-energy modes localised at the boundary between two topologically distinct phases. It turns out that these invariants solely depend on the quasiclassical Green's functions at the ends of the quantum wire. In addition, we present the formal solution of the disordered quantum wire, which can be calculated using an efficient numerical method introduced in chapter two. Utilising this approach in chapter four, we show that effects of disorder can lead to signatures which show striking similarities to the ones observed in experiments. We therefore substantiate the scepticism towards the alleged observation of Majorana fermions in the experiments mentioned earlier, [19–21]. Finally, we provide preliminary results on a numerical study regarding the possible formation of topological domain walls due to disorder fluctuations. We consider a one-dimensional quantum wire at criticality and by using the numerical method derived earlier, we investigate the influence of disorder fluctuations on the low-energy properties. In particular, the possible emergence of zero-energy modes, represented by a singularity in the quasi-particle density of states at zero-energy, is explored. These are predicted to form at the boundary between two distinct localised phases.

Part I

Quasiclassical approach to topological insulators and superconductors

1
Topological insulators and superconductors

Topological insulators and superconductors were recently identified as a very important subject of interest among various branches of condensed matter theory. The point of origin, however, is nowadays considered to be the discovery of the topological origin of the quantised Hall conductance of the quantum Hall effect, already described back in 1982 [1]. In topological insulators and superconductors there exists an intimate correspondence between their insulating bulk and exciting effects at the boundary. Indeed, this correspondence is rooted in the topology of the system which ensures a very robust nature of the boundary effects. In particular, metallic modes in one dimension that completely evade Anderson localisation exist on the boundary of certain two-dimensional systems.

In this chapter we review the classification of these systems. The classification is based on the identification of equivalent Hamiltonians that can continuously be deformed into one another without destroying the insulating bulk properties, and is a function of dimensionality of the system as well as symmetries present. Famous examples for different types of topological insulators and superconductors, their non-trivial topology as well as their boundary modes are discussed.

1.1 Definition

We start with a rather generic definition of topological insulators or superconductors [3]: A topological insulator or superconductor is a gapped phase of non-interacting fermion systems[1] which exhibits boundary modes. These boundary modes are gapless and they are topologically protected, i.e. arbitrary perturbations of the Hamiltonian that do not close the

---

[1]Although this restriction can be softened a bit.

bulk gap also do not qualitatively affect these states. However, these perturbations must not render the generic symmetries of the Hamiltonian. A topological insulator or superconductor possesses different phases which are characterised (labelled) by a number, a so-called topological invariant. The nature of this invariant (and therefore their associated phases) depends on the dimensionality and symmetries of the system. It turns out that the invariant either gives an integer or a binary $\mathbb{Z}_2$ quantity. As the name implies, these invariants can only change if the phase is changed which in return can only happen if the bulk gap is closed.

The latter can be understood by a very intuitive argument: Consider two insulators attached to each other, we ignore the trivial case in which both are trivial insulators or topological insulators with the same value of the invariant. The remaining two cases will always be separated by a boundary. This boundary however will host gapless boundary modes, which implies a gap closure. Hence one cannot interpolate between both systems without closing the band gap at the boundary. By the same token, systems with the same invariant are topologically equivalent and can be deformed smoothly into one another without closing the gap.

Simply put, a classification of topological insulators and superconductors has been established by determining the classes of topological insulators and superconductors that can continuously be transformed into one another without closing the gap, and are thus described by the same quantity/invariant.

A frequently used example for such a topological invariant in mathematics is the Euler characteristic. In the simplest case of a closed orientable surface this invariant is a linear function of the number of holes, the genus, within this surface. The Gauss-Bonnet theorem then ensures that smooth deformations (not changing the number of holes) of the surface will leave this characteristic unchanged [22]. An analogy to this theorem will be given later.

1.2 Symmetry classes - The ten fold way

For non-interacting disordered fermion systems there exist a classification due to Altland and Zirnbauer [4, 23]. The classification is based on the presence or absence of three generic symmetries: time-reversal symmetry (T), charge-conjugation (or particle-hole) symmetry (C) and a third, chiral (or sublattice) symmetry (S). The Hamiltonians under consideration are not translationally invariant and the symmetries are represented by anti-unitary operators which commute with the Hamiltonian of the system.[2]

Let H be the N-dimensional first quantised Hamiltonian of our quantum system, represented by a matrix of dimension $N \times N$. For both, time-reversal and charge-conjugation symmetry the anti-unitary operators can be represented as a product of a unitary operator (U_T or U_C, respectively) and an anti-unitary operator. The latter is frequently chosen as

---

[2]Note that translational invariant symmetries, i.e. unitary symmetries that commute with the Hamiltonian have to be excluded. If such a unitary symmetry is present, the Hamiltonian is always block-diagonalisable (reducible). For the classification one thus only considers irreducible representations of the Hamiltonians.

complex conjugation operator K, i.e. $T = K \cdot U_T$ and equivalently for C.

The system is time-reversal invariant if H commutes with the time reversal symmetry operator, i.e.

$$U_T^\dagger H^{\mathrm{T}} U_T = H. \tag{1.1}$$

By the same token, a system is charge-conjugation invariant if

$$U_C^\dagger H^{\mathrm{T}} U_C = -H. \tag{1.2}$$

In addition to the two symmetry operations above, the product of both symmetry operations $S = T \cdot C$ gives rise to a third symmetry. A system possesses chiral symmetry if

$$U_S^\dagger H U_S = -H, \tag{1.3}$$

i.e. if H anti-commutes with the unitary matrix $U_S = U_T \cdot U_C^*$. Note that although the product of both symmetries is a unitary operation, the fact that H and U_S anti-commute spoils the triviality of this symmetry (its reducibility). However, for two distinct time-reversal (charge-conjugation) operators $T_{i=1,2}$ ($C_{i=1,2}$), the subsequent application of two symmetry operations will be a unitary operation that commutes with H, and hence will be discarded.

The products U^*U, for $U = U_C$ or U_T, are at this point not further specified, however they both obviously commute with H. Since we excluded unitary symmetries that commute with H, we are dealing with an irreducible representation of the latter, hence Schur's lemma ensures that the product U^*U of two unitary matrices is the identity up to a sign,

$$U^*U = \pm\mathbb{1}. \tag{1.4}$$

By simply counting the possible combinations we conclude that there are ten different classes (all possible combinations of T and C will lead to nine classes, however in the absence of both, S can still be present filling the missing spot). The ten symmetry classes are comprised in table 1.1, where the 0 entries indicate the absence of a symmetry and ± 1 entries refer to the sign in eq. (1.4).

Having identified the ten possible symmetry configurations the question regarding the exhaustion of this scheme was answered by the authors of refs. [4, 23]. We will address this question together with some physical remarks by further inspecting table 1.1. The first column labels the symmetry classes in a way that will be explained later. One immediately recognises the original Wigner and Dyson classes A, AI and AII for random matrices. These classes are naturally extended by inducing the chiral symmetry and are therefore called chiral classes, AIII, BDI and CII. The remaining four symmetry classes (D, C, DIII, and CI) are found to be realised in disordered superconducting systems described by Bogoliubov-de Gennes Hamiltonians [4].

Label	T	C	S	Hamiltonian	G/H
A	0	0	0	$U(N)$	$U(2n)/U(n) \times U(n)$
AI	+1	0	0	$U(N)/O(N)$	$Sp(2n)/Sp(n) \times Sp(n)$
AII	-1	0	0	$U(2N)/Sp(2N)$	$O(2n)/O(n) \times O(n)$
AIII	0	0	1	$U(N+M)/U(N) \times U(M)$	$U(n)$
BDI	+1	+1	1	$O(N+M)/O(N) \times O(M)$	$U(2n)/Sp(2n)$
CII	-1	-1	1	$Sp(N+M)/Sp(N) \times Sp(M)$	$U(2n)/O(2n)$
D	0	+1	0	$SO(2N)$	$O(2n)/U(n)$
C	0	-1	0	$Sp(2N)$	$Sp(2n)/U(n)$
DIII	-1	+1	1	$SO(2N)/U(N)$	$O(2n)$
CI	+1	-1	1	$Sp(2N)/U(N)$	$Sp(2n)$

Table 1.1: Altland-Zirnbauer classification of random matrix ensembles. Symmetry classes are labelled due to Cartan (first column). The presence or absence of time-reversal (T), charge-conjugation (C) and sublattice symmetry (S) are indicated by ± 1 and 0, respectively. The fourth column lists the symmetric space of $\exp(iH)$, while the fifth column shows the target spaces of the non-linear-sigma-model (see text for explanation). Table taken from [4].

The fourth and fifth column in table 1.1 is related to the completeness of this list of classes. We consider the first quantised Hamiltonian H to be represented as an $N \times N$ matrix and construct the object $X = iH$, as well as $\exp\{X\}$. Formally the former object is an element of an algebra, while the latter is an element of a corresponding coset space [4]. Physically, the latter object can be interpreted as the quantum mechanical time-evolution operator $\exp\{iHt\}$. For each class, the symmetries impose restrictions on the structure of H (and thus the full algebra is restricted to a sub-algebra thereof) and consequently on the time-evolution operator and its coset space. These coset spaces are summarised in the fourth column of the table.

A few simple examples should clarify this point. Consider class A, i.e. since no symmetries are present, H is simply a hermitian matrix. Consequently X is skew-hermitian, i.e. $X^\dagger = -X$. Since X and $X^\dagger$ trivially commute with each other, it follows that $\exp\{X\}\exp\{X\}^\dagger = $ id. Hence $\exp\{x\}$ is an element of the Lie group $U(N)$. It is obvious that upon further restricting our system, the Hamiltonians have to be restricted to subsets. In fact for class AI, the Hamiltonian can be represented as a real symmetric matrix, i.e. $H = H^\mathrm{T}$. The coset space turns out to be given by the quotient $U(N)/O(N)$. To this end, one realises that each hermitian matrix can be decomposed into a real symmetric and skew-symmetric part, $H = H_s + iH_a$. If we construct the likewise skew-symmetric $X_a = iH_a$, it follows that $\exp\{X\}\exp\{X\}^\mathrm{T} = $ id and hence $\exp\{X\} \in O(N)$. The coset space of real symmetric matrices is thus the coset space $U(N)/O(N)$, as indicated in table 1.1. The remaining entries of the classification table are constructed accordingly.

Label /d	0	1	2	3	4	5	6	7	8
A	$\mathbb{Z}$	0	$\mathbb{Z}$	0	$\mathbb{Z}$	0	$\mathbb{Z}$	0	$\mathbb{Z}$
AIII	0	$\mathbb{Z}$	0	$\mathbb{Z}$	0	$\mathbb{Z}$	0	$\mathbb{Z}$	0
AI	$\mathbb{Z}$	0	0	0	$2\mathbb{Z}$	0	$\mathbb{Z}_2$	$\mathbb{Z}_2$	$\mathbb{Z}$
BDI	$\mathbb{Z}_2$	$\mathbb{Z}$	0	0	0	$2\mathbb{Z}$	0	$\mathbb{Z}_2$	$\mathbb{Z}_2$
D	$\mathbb{Z}_2$	$\mathbb{Z}_2$	$\mathbb{Z}$	0	0	0	$2\mathbb{Z}$	0	$\mathbb{Z}_2$
DIII	0	$\mathbb{Z}_2$	$\mathbb{Z}_2$	$\mathbb{Z}$	0	0	0	$2\mathbb{Z}$	0
AII	$2\mathbb{Z}$	0	$\mathbb{Z}_2$	$\mathbb{Z}_2$	$\mathbb{Z}$	0	0	0	$2\mathbb{Z}$
CII	0	$2\mathbb{Z}$	0	$\mathbb{Z}_2$	$\mathbb{Z}_2$	$\mathbb{Z}$	0	0	0
C	0	0	$2\mathbb{Z}$	0	$\mathbb{Z}_2$	$\mathbb{Z}_2$	$\mathbb{Z}$	0	0
CI	0	0	0	$2\mathbb{Z}$	0	$\mathbb{Z}_2$	$\mathbb{Z}_2$	$\mathbb{Z}$	0

Table 1.2: Classification of topological insulators and superconductors. Symmetry classes are again labelled by the Cartan labels and rearranged. Depending on the dimension d, a trivial insulator or superconductor exists ($\mathbb{Z}$ or $\mathbb{Z}_2$) or not (0). The non-zero entries indicate that the topological phases present are characterised by a $\mathbb{Z}_2$ invariant or an integer ($\mathbb{Z}$). Table can be found in [3].

The completeness of this table was established by realising that the entries in the fourth column agree with a set of mathematical objects, called symmetric spaces. Details are not of interest at this point and beyond the scope of this text, however it was shown by Cartan in 1926 [24] that this set includes only ten symmetric spaces. This proves that the classification is exhausted and explains (within this framework) the notation used in the first column of table 1.1. The fifth column is related to the physics of Anderson localisation at long wavelength, which can described by a non-linear-sigma-model. The target space of these systems, again turn out to be given by the ten symmetric spaces.

1.3 Classification table of topological Insulators

Table 1.2 shows the classification table of topological insulators and superconductors. The classification is based on the ten symmetry classes of random Hamiltonians presented in the previous section. The entries $\mathbb{Z}$, $\mathbb{Z}_2$ and 0 indicate whether in the corresponding symmetry class, for a given dimension d, the existing phases are characterized by an integer, a binary quantity or are absent at all, respectively. How the corresponding invariants are constructed in details depends on the specific model chosen. The symmetry classes in table 1.2 are re-organised in a way to reveal its periodicity. The classification shows a regular pattern composed of a sequence of $(2\mathbb{Z}, 0, \mathbb{Z}_2, \mathbb{Z}_2, \mathbb{Z})$, that is periodic (modulo 8) in the dimensionality. This so-called Bott periodicity [25] is closely related to the reappearance of the symmetric spaces and its mathematical origin goes beyond the scope of this work.

Before elaborating on the specific realisations for the different entries of this table, we

will briefly discuss the structure behind it and comment on the genesis of it. Due to the formal nature of this discussion, readers desperately longing for a concrete physical model may unhesitatingly skip the remainder of this section.

Classification schemes

The classification table 1.2 has been derived by various means [3, 5, 26]. All classification schemes are related to the symmetric spaces discussed earlier and have an underlying mathematical framework:

Absence of Anderson localisation at the boundary - NLσM classification

In the definition of a topological insulator or superconductor given at the beginning of this chapter, a basic ingredient was the existence of gapless edge modes at the boundary of the system. Being of topological origin, these states are protected against disorder and other backscattering effects. This obtrudes the interpretation of the $(d-1)$-dimensional boundary of a d-dimensional topological insulator or superconductor, as a metal that evades Anderson localisation. In ref. [26] it was studied what topological terms can be added to the non-linear-sigma-model (NLσM), describing Anderson localisation on the boundary of a topological insulator, which evades this phenomenon. It turns out, that only two types of terms can be added: a Wess-Zumino-Witten or a $\mathbb{Z}_2$-term. This result is determined by the homotopy groups of the target space (again represented by the ten symmetric spaces and presented in the fifth column in table 1.1). The homotopy groups are either $\pi_d = \mathbb{Z}$ or $\pi_{d-1} = \mathbb{Z}_2$, respectively. A classification of topological insulators and superconductors thus breaks down to the well known table of homotopy groups for the symmetric spaces.

Projectors - Grassmanian classification

Given a topological insulator the ground state is given by the filled bands below the Fermi energy in the Brillouin zone. With the eigenstates of the Hamiltonian above and below the Fermi energy well separated by the bulk gap, it is common to *flatten* the bands on both sides of the gap [3, 27]. As long as the bulk gap is not closed, the Hamiltonian can always be continuously deformed into one with unique eigenvalues $+1$ and -1, above and below the gap respectively. This deformed Hamiltonian is usually called *flattened* or *simplified* Hamiltonian. Note that the eigenstates are not changed and since it can be shown that topological properties do not depend on the energies of the occupied bands but only on the eigenstates, the flattened Hamiltonian allows for simplified calculations. The procedure of flattening is illustrated in fig. 1.1.

The flattened Hamiltonian in momentum space is defined as
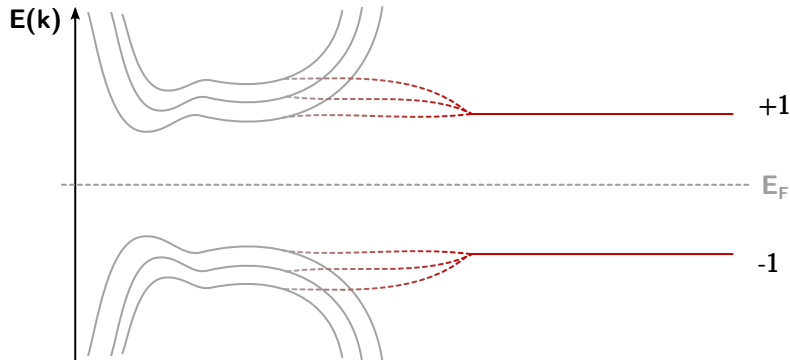
$$Q(k) = 1 - 2P(k),$$

Figure 1.1: Flattening of a generic band insulator. The bands $E_a(k)$ (grey curves) are continuously deformed to $E_\pm = \pm 1$ (red curves) without closing the band gap.

where $P(k) = \sum_a |u_a^-(k)\rangle\langle u_a^-(k)|$ is the spectral projector onto the filled bands, and $\{|u_a^-(k)\rangle\}$ denotes the set of filled Bloch wave functions with (occupied) band index a. We denote by n the number of bands below the gap, i.e. with energy $E_a(k) = -1$ and by m the number of bands above the gap with energies $E_a(k) = +1$. With no symmetries present, the flattened Hamiltonian $Q(k)$ is a map from the Brillouin zone to the set of eigenvectors, i.e. $U(n+m)$. However, there exists an intrinsic gauge symmetry due to the possibility of relabelling the n filled and m empty states. Thus $Q(k)$ is a map from the Brillouin zone to $U(n+m)/(U(n) \times U(m)) =: G_{m,m+n}(\mathbb{C})$, the complex Grassmannian. For a classification of topological insulators and superconductors, two ground states of different classes should not be able to be deformed into one another without closing the gap. Thus, it is again the homotopy group of the target spaces of the flattened Hamiltonian $Q(k)$ that is used to identify the phases.

Considering class A, i.e. no symmetries present, we have already seen that the target space of $Q(k)$ is $G_{m,m+n}(\mathbb{C})$. To find out whether or not the symmetry class in a given dimension is topologically trivial, we rely on well known results on homotopy groups. In the present case it turns out that $\pi_2(G_{n,n+m}(\mathbb{C})) = \mathbb{Z}$ while $\pi_3(G_{n,n+m}(\mathbb{C})) = \{\text{id}\}$, i.e. while in two dimensions there exist $\mathbb{Z}$ topological phases in one dimension higher none exists.

In the presence of symmetries, the space of projectors will be further restricted. In case of a present chiral symmetry (such as in class AIII) the projector can always be brought into block off-diagonal form

$$Q(k) = \begin{pmatrix} & q \\ q^\dagger & \end{pmatrix}.$$

Since $Q^2 = \mathbb{1}$, it follows that q has to be unitary, $q \in U(m)$. The homotopy groups of $U(m)$ are $\pi_{d\in 2\mathbb{N}}(U(m)) = \{\text{id}\}$ and $\pi_{d\in 2\mathbb{N}+1}(U(m)) = \mathbb{Z}$, i.e. trivial in even and non-trivial in odd dimensions.

Subsequently, a complete classification table based on the homotopy groups of the space of projectors can be constructed, which of course is equivalent to tab. 1.2. The reappearance of the ten symmetric spaces is revealed by considering the projectors in a zero-dimensional momentum space, or at invariant points of the Brillouin zone related by time-reversal or charge-conjugation symmetry. In this case, the spaces of projectors again turn out to be exactly the ten symmetric spaces discussed earlier. On passing we note that an equivalent classification was achieved using Clifford algebras and K-theory, revealing the spaces of projectors as the classifying spaces used in K-Theory [5].

The above discussion shows that the nature of the insulator is fully encoded in the projectors $Q(k)$. As a map from the Brillouin zone to some Grassmannian it assigns to each momentum vector k a transformation to the eigenstates. Understanding this transformation implies understanding the topology of the insulator. If this transformation can continuously be transformed to a trivial transformation[3], the insulator is trivial. On the other hand, if the transformation is not homotopic to the identity, the insulator is topologically non-trivial.

1.4 Chern number and the integer quantum Hall effect

Let us continue by introducing a well known model and thereby shine some light on the formal discussion of the previous subsections. We have learned that there exists a classification table which tells us the symmetry class (and dimension) necessary to find topological insulator or superconductor. We were also told by which type of quantity the topological phases are labelled. How this labelling, i.e. the construction of the topological invariant, is done in detail will be explained next using the example of the *integer quantum Hall effect* (IQHE).

Indeed the IQHE is now considered to be one of the first theoretical emergences of a topological insulator. In a seminal work [1], Thouless *et al.*, showed that the transverse Hall conductivity σ_{xy} is quantised. Moreover, the authors realised that the origin of this quantisation was routed in the topology of the bulk of the system. For the IQHE, electrons are confined to a two dimensional plane and subject to a strong magnetic field, thus neither time-reversal nor particle-hole symmetry are present. According to table 1.1 the system is a member of class A, and table 1.2 reveals that in two dimensions the phases are indeed quantised ($\mathbb{Z}$). It turns out that the quantisation of the Hall conductance is described by the (first) Chern number C_1. The Chern number is a topological invariant, hence two Hamiltonians that cannot be continuously deformed into one another without closing the gap, cannot give the same value of the invariant. More precisely, the Hall conductivity is given by

$$\sigma_{xy} = C_1 \, e^2/h.$$

Before we construct the first Chern number explicitly, we should pause and embrace this

---

[3]Notice that we used $\{\mathrm{id}\}$ as the set that contains only the identity element and hence the transformation was trivial.

seemingly innocent result. The Hall conductance can straightforwardly be calculated by means of linear response theory and is a real, measurable quantity [28]. The result above is purely geometrical and hence this quantisation is robust. Thereby, the non-trivial geometry of the topological insulator ensures the robustness of an experimentally measurable quantity, a canonical scheme of topological insulators usually referred to as *bulk-boundary correspondence*.

We now aim to construct the integer invariant and offer two common interpretations of the result. The quantisation of circulating electrons lead to quantised Landau levels $E_n = \hbar\omega_c(n + \frac{1}{2})$, with cyclotron frequency ω_c. Although it is not possible for the states to be labelled with their momentum, a band structure can be constructed by choosing a proper unit cell. This allows for the application of Bloch's theorem and the labelling of the states with a two-dimensional crystal momentum. The energy levels are then given by the Landau levels, $E_n(k) = E_n$. A bulk energy gap is present if, say N of these Landau level are filled while the remaining ones are empty, the band structure is thus equivalent to one of an insulator.

Given the band structure, a flattened Hamiltonian $Q(k)$ is easily defined. The effective Hilbert space is $\mathcal{H}_k \cong \mathbb{C}^{2N}$ if N denotes the total number of Bloch wavefunctions, and the Brillouin zone is a two-dimensional torus $\mathbb{T}^2$. However, since we are interested in the flattened Hamiltonian, we can choose $N = 2$ for simplicity with one occupied and one empty band. We have already learned that $Q(k)$ assigns to each (quasi-)momentum k an eigenvector $|u^-(k)\rangle$ and that these states posses a $U(1)$ gauge-freedom, as they are only defined up to a quantum mechanical phase. A state is thus represented by an equivalence class $[|u^-(k)\rangle] := \{g|u^-(k)\rangle : g \in U(1)\}$. The collection of all $\mathcal{H}_k$ constitutes a mathematical object called *vector bundle*[4] over the base space $\mathbb{T}^2$, denoted by $P(\mathbb{T}^2, U(1))$. The group g acting on the states is called structure group, and acts by left multiplication. The bundle comes with a projection π (see fig. 1.2) whose inverse image maps from the torus to the fibres $[|u^-(k)\rangle]$. Notice that the structure group and the fibres are both (isomorphic to) $U(1)$, and hence the vector bundle is called a principle bundle.

Pictorially speaking, a bundle is called trivial if it can globally be written as a direct product of its base space (in our case $\mathbb{T}^2$) and the fibre. The word globally is very important at this point. A non-trivial bundle although locally a direct product space, cannot be written as one globally.

On this bundle the Berry connection [29][5],

$$a(k) = a_\mu(k)\mathrm{d}k^\mu := i\langle u^-(k)|\mathrm{d}u^-(k)\rangle = -i\langle \mathrm{d}u^-(k)|u^-(k)\rangle,$$

can be constructed, where the exterior derivative is defined as $\mathrm{d} = (\partial_{k^\mu})\mathrm{d}k^\mu$. Note that

---

[4]More precisely a principal bundle [22].

[5]Sloppily speaking, a connection is a unique decomposition of the bundles tangent space into a horizontal and vertical subspace, that allows for directional derivatives of vector fields. Physically, the corresponding form can be thought of as a vector potential.
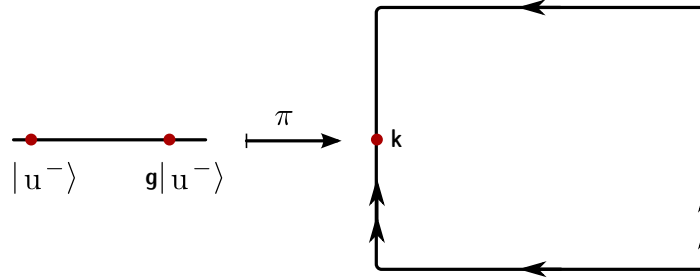
Figure 1.2: Principal bundle over the Brillouin torus $\mathbb{T}^2$. The structure group g acts by left multiplication on elements $|u^-(k)\rangle$ of the fibre $\simeq \pi^{-1}(k)$. The projection π maps from the fibre onto the base space given by the torus T^2.

the Chern number does not depend on the specifically chosen connection. Given the Berry connection a, the Berry curvature is defined as[6]

$$F = \mathrm{d}a = F_{\mu\nu}\mathrm{d}k^\mu \wedge \mathrm{d}k^\nu := i\langle \mathrm{d}u^-(k)| \wedge |\mathrm{d}u^-(k)\rangle. \tag{1.5}$$

At this point we recall the previously mentioned Gauss-Bonnet theorem which connected the integral of the (Gaussian) curvature over a closed surface to an integer (in units of π), which in return was related to the holes in the manifold. The natural generalisation of this theorem identifies the first Chern number

$$C_1 = \frac{1}{2\pi} \int_{\mathrm{BZ}=\mathbb{T}^2} F, \tag{1.6}$$

with an integer. As two manifolds of different genus cannot be continuously deformed into one another without punching or closing a hole, a difference in the Chern number indicates that two systems are topologically distinct and only through closing the band gap can they be transformed into one another.

Two geometrical interpretations of the above statement can be illustrated by conveniently choosing the simplest model of a two-band insulator. The Hamiltonian we consider is given by

$$H(k) = \sum_{i=1}^{3} h_i(k)\sigma_i, \tag{1.7}$$

where the $h_i(k)$ are real, periodic functions and $\sigma_{i=1,2,3}$ are the Pauli matrices representing the (pseudo)-spin degree of freedom. In the above model we ignore trivial contributions

---

[6]If a is interpreted as a vector potential, F would analogously be interpreted as a magnetic field.

proportional to $\sigma_0 = \mathbb{1}$ since they merely lead to a shift in energy. We again denote the eigenstates of the upper and lower band by $|u^{\pm}(k)\rangle$ and the energies of both bands are given by $\epsilon^{\pm} = \pm\sqrt{\sum_i h_i^2} \equiv \pm|h|$. The band gap does not close as long as $|h| \neq 0$. As usual, we concentrate on the lower filled band $|u^-(k)\rangle$. $\hat{h} = h/|h|$ then defines a map from the Brillouin torus to the sphere S^2 and the filled eigenstates take the polar-representation[7] $|u\rangle = (-\sin\Theta/2, \exp[i\phi]\cos\Theta/2)^{\mathrm{T}}$. Let $H(k)$ be given such that at $k = 0$, $\hat{h}$ is pointing at the north pole[8] ($\Theta = 0$) the eigenvector $|u\rangle$ is not well-defined because of the arbitrary phase $\exp[i\phi]$. However, if the vector stays in the southern hemisphere U_S of S^2, the eigenvector $|u_S\rangle = |u\rangle$ is well-defined. A well-defined eigenvector on the northern hemisphere U_N is easily constructed, $|u_N\rangle = \exp[-i\phi]|u_S\rangle$. A natural question to ask is what happens at the equator, i.e. the non-vanishing intersection which surges the northern hemisphere, $\partial U_N = U_N \bigcap U_S \simeq S^1$? At the transition we can define a transition function $g : \partial U_N \to U(1)$ (notice the reappearance of the structure group $U(1)$) that defines the phase change by $g = \exp[i\phi]$. The topology of the bundle can thus be described by the behaviour of the transition function g. If $\hat{h}$ does not cover the whole sphere, the eigenvector of the corresponding hemisphere can be globally defined and the transition function is trivial $g \simeq \mathrm{id}_{S^2}$. If, however, $\hat{h}$ ends up covering the whole sphere, the transition function cannot be transformed to the identity and the topology of the bundle is non-trivial. In the latter case it is not possible to construct a global eigenvector on the whole sphere [30]. Indeed it is straightforward to see that the Chern number (1.6) is given by

$$C_1 = \frac{1}{2\pi i} \int_{\partial \hat{h}^{-1}(U_N)} \mathrm{d}\log(\hat{h}^{\star}g), \tag{1.8}$$

i.e. the winding number of the transition function g. Since the construction of a global eigenvector is only possible if g is homotopic to the identity, the Chern number is vanishing $C_1 = 0$. In contrast, a non-vanishing Chern number $C_1 \neq 0$ indicates a non-trivial transition function g and an obstruction to define a global eigenvector. For the explicit two-band model, the first Chern number can straightforwardly computed by explicitly evaluating eqs. (1.5) and (1.6), and is given by[9]

$$C_1 = \frac{1}{4\pi} \int_{\mathbb{T}^2} h|h|^{-3} \cdot \left(\partial_{k_x} h \times \partial_{k_y} h\right) \mathrm{d}k_x \wedge \mathrm{d}k_y. \tag{1.9}$$

Consider a closed loop in the Brillouin zone, under the map $\hat{h} : \mathbb{T}^2 \to S^2$ this loop will describe a closed surface S in the h_x, h_y plane and since the system is gapped, a winding

---

[7] We drop the superscript since we only consider the lower filled band.

[8] Notice that multiplication by the inverse $\exp[-i\phi]$ would merely shift this singularity to the south pole at $\Theta = \pi$.

[9] We went with a very sloppy yet common notation $\epsilon^{ijk} h_i \mathrm{d}h_j \wedge \mathrm{d}h_k = 2h \cdot (\partial_x h \times \partial_y h)\mathrm{d}k_x \wedge \mathrm{d}k_y$, i.e. we introduced an artificial cross-product in two dimensions. The latter representation is commonly used in literature ignorant of exterior calculus [31].

number around the origin can be associated to it. The Chern number is exactly this winding number defined in eqs. (1.8) and (1.9). If we project the sphere down to $\mathbb{R}^3 \setminus \{0\}$, this winding number counts the number of times the closed surface S wraps around the origin. In case of a trivial system, S does not contain the origin and the winding is thus trivial $C_1 = 0$, which corresponds to the previously discussed scenario in which $\hat{h}$ does not explore the whole sphere but stays in one hemisphere. Whereas in the case of a non-vanishing winding number $C_1 \neq 0$, the map explorers the whole sphere (with a non-trivial transition).

Figure 1.3 illustrates the map $\hat{h}$ and corresponding surface on S^2. In a more physical interpretation eq. (1.6) defines a flux through the Brillouin zone. The source of this flux is revealed by eq. (1.9), since $h|h|^{-3}$ defines the field of a point-like magnetic monopole at the origin $h = 0$. Placed within the torus the flux is non-vanishing, while a monopole outside of the torus contributes to no total flux.
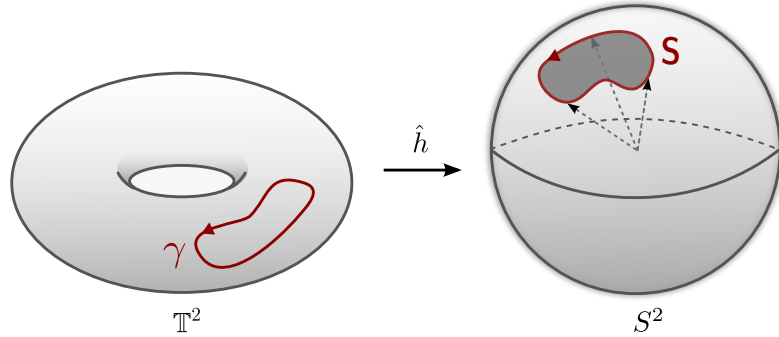
Figure 1.3: Map from the Brillouin torus to the Bloch sphere S^2. A closed loop on $\mathbb{T}^2$ is mapped to a surface S on S^2.

1.5 Dirac Hamiltonians

We return to the generic two-level Hamiltonian

$$H(k) = \hat{h} \cdot \sigma = \sum_{i=1}^{3} \hat{h}_i(k)\sigma_i, \tag{1.10}$$

where we defined the three-dimensional vectors $\hat{h} = (\hat{h}_1, \hat{h}_2, \hat{h}_3)$ and $\sigma = (\sigma_1, \sigma_2, \sigma_3)^{\mathrm{T}}$. The vector $\hat{h}$ again defines a map from the Brillouin zone (the torus $\mathbb{T}^2$) to the sphere S^2, as it was discussed in the previous section.

Possible time-reversal symmetry restricts the choice of $\hat{h}_i$ depending on the nature of σ. If the Pauli matrices constitute a basis for a system with pseudo-spin ($T^2 = +1$), it follows trivially that $\hat{h}_1$ and $\hat{h}_3$ have to be even functions in k, whereas $\hat{h}_2$ has to be odd. According to eq. (1.9), the Chern number has to vanish. For a system with real spin degrees of freedom

($T^2 = -1$), in order to preserve time-reversal symmetry all $\hat{h}_i$ have to odd functions in k. Consequently the system has to be gapless.

In the vicinity of a point of gap closure (such as at time-reversal invariant momenta), the Hamiltonian (1.10) can be linearised leading to a two-dimensional Dirac Hamiltonian. These points are frequently referred to as Dirac points. The generic form of a massive Dirac Hamiltonian is achieved[10] by replacing $\hat{h}_{i=1,2} \to k_{1,2}$ and $\hat{h}_3 \to m$ in eq. (1.10),

$$H(k) = \sum_{i=1}^{2} k_i \sigma_i + m\sigma_3. \tag{1.11}$$

The dispersion $E(k) = \pm\sqrt{k^2 + m^2}$ exhibits a gap of $2|m|$. For the massive Dirac Hamiltonian the Chern number of the filled band is given by

$$C_1 = \frac{1}{2\pi} \int_{T^2} \frac{m}{2} \left(m^2 + k^2\right)^{-3/2} \mathrm{d}k = \mathrm{sgn}\, m/2.$$

Surprisingly the Chern number and thus the Hall conductance turns out to be a half integer, which contradicts our statements earlier. Indeed we cheated in stating that the Chern number always has to be an integer and indeed the linear dispersion of the Dirac Hamiltonian serves as a perfect counter example. The reason behind this is rooted in the fact that the dispersion stays linear in the limit $|k| \to \infty$ and the integration manifold is non-compact and effectively halved, leading to the half-integer result [3]. The integer result is always true on a lattice, for a continuum model, however, a regularisation of the mass, which annihilates the linear dispersion in the large k limit, is necessary. Although the full Chern number can only be obtained by integrating over the full Brillouin zone, an integer change in the invariant is still present within the Dirac description. A sign change in the mass of the Dirac Hamiltonian thus indicates a transition, which necessarily involves a closing of the gap. Figure 1.4 illustrates the dispersion around the Dirac points and the change of the Chern number as a function of mass. Dirac Hamiltonians with linear dispersion will cross our paths again in the second part of this work, where the linearisation is used to formulate a quasiclassical description of topological insulators and superconductors.

1.6 Haldane model

Haldane [32] demonstrated that a non-trivial two-band insulator with a quantised Hall conductance can be realised in a honeycomb lattice with two inequivalent sub-lattices in the absence of an external magnetic field. In order to break the time-reversal symmetry the model requires a local magnetic flux that only affects second neighbour hopping amplitudes,

---

[10]In order to avoid confusion, we linearise the two level Hamiltonian around a momentum, say q, close to the Dirac point. By setting both $\hbar$ and the Fermi velocity v_F to unity and redefining $q \to k$ we end up with eq. (1.11).
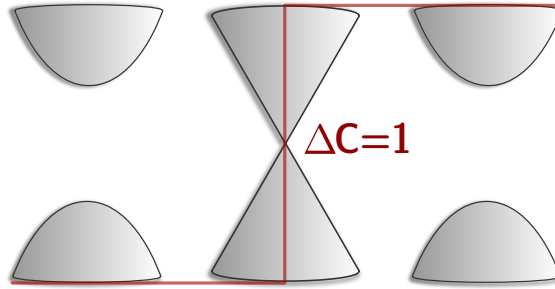
Figure 1.4: Schematic dispersion for topological insulators with different Chern numbers (indicated by red curve). At the Dirac point, the gap closes in a linear manner and the Chern number signalises an integer jump ΔC.

with a vanishing net flux per unit cell. The system possesses two Dirac points around which the linearised Hamiltonian is given by eq. (1.11), and the mass terms at this two points are $m = M \pm t \sin \phi$, where $\pm M$ are the on-site energies of the sub-lattices, t is the hopping amplitude and ϕ the Aharnov-Bohm phase (induced by the local flux [32]). Modulating the two parameters M and ϕ the phase diagram of the Haldane model (fig. 1.5) can be constructed. One recognises two phases ($|M| < t \sin \phi$) corresponding to a positive and negative Chern number (coloured areas) and a third trivial phase ($|M| > t \sin \phi$) corresponding to a vanishing Chern number. The gap vanishes at the Dirac points but a finite gap evolves as a function of both parameters, separating all three phases. The transition lines ($|M| = t \sin \phi$) separating these phases indicate the parameter values for which the system is no longer an insulator.
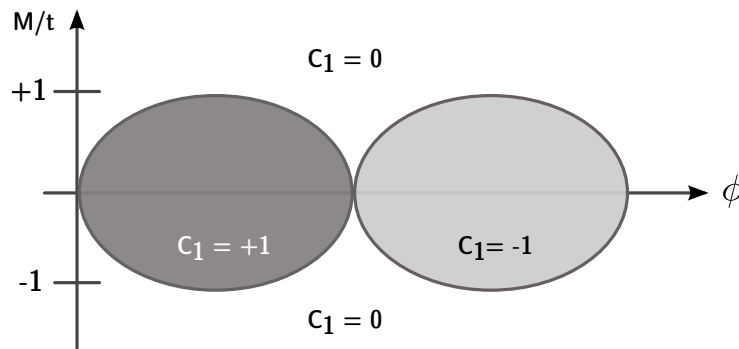
Figure 1.5: Phase diagram for the Haldane model. The system is in the trivial phase ($C_1 = 0$) for $|M/t| > \sin \phi$ and in the non-trival ($C_1 = \pm 1$) for $|M/t| < \sin \phi$. The lines $|M/t| = \sin \phi$ indicate phase transitions at which the bulk gap closes.

1.7 Edge states

By definition, a topological insulator hosts metallic surface states at its boundary. On several occasions we have seen, that a gap closing has to occur on the boundary between two insulators with different values of the topological invariants. For Dirac Hamiltonians we now illustrate that one can indeed prove the existence of such states by simple arguments. To this end, we consider an interface between two topological insulators described by a massive Dirac Hamiltonian (such as the Haldane model). On the left-hand side the insulator is supposed to be trivial ($C_1 = 0$) while on the right-hand side it is non-trivial ($C_1 = 1$). As we have seen, such a change in the Chern number can only be achieved by a sign change of the mass across the interface, as illustrated in fig. 1.6. In order to describe the edge state sitting at the interface where the mass vanishes, one solves the corresponding Schrödinger equation in real space for the massive Dirac Hamiltonian. A detailed derivation is done in [2] leading to the normalised solution

$$\Psi(x, y) \propto \exp[ik_x x] \exp[-\int_0^y m(y')\mathrm{d}y'](1, 1)^\mathrm{T}, \qquad (1.12)$$

where the mass changes sign along the y-axis and vanishes at $y = 0$. The eigenenergy (in units of $\hbar = v_F = 1$ and for $E_F = 0$) is given by $E(k_x) = k_x$. Thus eq. (1.12) describes a chiral (moving only in one direction) state, that transversely crosses the interface (in x-direction) with a positive Fermi velocity. In fig. 1.7 this single state connecting the valence and conduction band is illustrated.
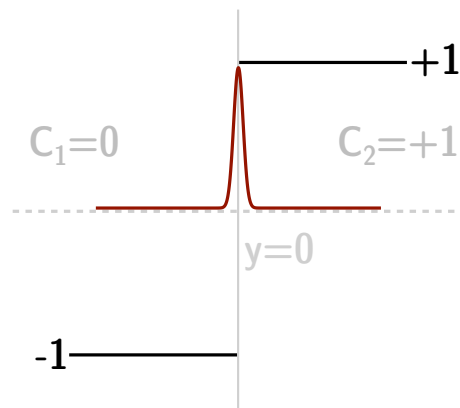

Figure 1.6: Schematic illustration of an interface between a trivial insulator (left) and a non-trivial one (right). The sign of the mass term in the Dirac Hamiltonian changes (black lines) from -1 to $+1$ at the interface ($y = 0$). The red curve represents the wave function of the localised zero energy mode at the interface. Details are explained in the text.

We have yet encountered another example of the bulk boundary correspondence. Of course, the procedure above is not tied to Dirac Hamiltonians and the idealised band structure in fig. 1.7 might become more complicated. The Fermi energy could in general intersect with the connecting band several times. In case of an edge state, it will always cross it an odd number of times and for each intersection the direction of the Fermi velocity needs to be taken into account. As a consequence, the weighted sum of all intersections will always equal the change in Chern numbers across the interface at which the transition happens.
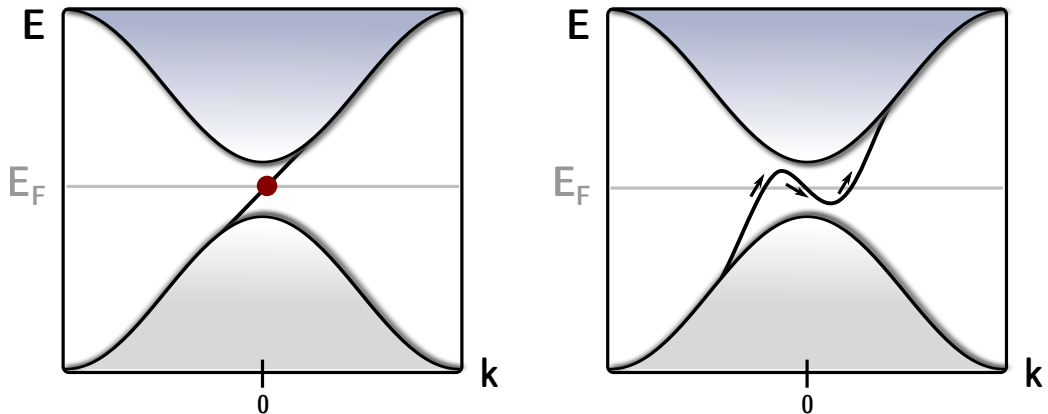
Figure 1.7: Chiral edge state crossing the Fermi energy. Left: The edge state crosses the Fermi energy once with positive group velocity. Right: The band of the chiral edge state crosses the Fermi energy three times. Twice with positive and once with negative group velocity. The direction of the velocity is indicated by arrows.

1.8 $\mathbb{Z}_2$-topological insulators

The above arguments lead to a vanishing Chern number in the presence of time-reversal symmetry. It was shown by Kane and Mele [6, 7], that for a system with half integer spin, spin-orbit interactions open a possibility for a topologically non-trivial system with unbroken time-reversal symmetry. Although the Chern number is always trivial, the phases can be classified by a topological $\mathbb{Z}_2$ invariant. The authors considered graphene described by a Haldane model but replaced the local magnetic flux by spin-orbit interactions. The physical phase distinguished by the $\mathbb{Z}_2$-invariant is called the *quantum spin Hall effect* (QSHE). Note that these results were independently derived by Zhang *et al.* [33, 34]. Where the QSHE was predicted in HgTe quantum wells, which was experimental confirmed shortly thereafter [8].

The presence of time-reversal symmetry relates a Bloch states at k to the one at $-k$ and thus the time-reversal operator defines an anti-unitary map from the fibre at k to the fibre at $-k$. And indeed, the valence bundle turns out to be always trivial considering the Chern number and the constraints imposed on the eigenstates reveal the non-triviality of the

system [30].

Due to Kramer's theorem all eigenstates of the Hamiltonian are at least two-fold degenerate. Spin-orbit coupling splits this degeneracy except for isolated points called time-reversal-invariant moments (TRIM). These points are located at the boundary of the effective Brillouin zones[11]. The binary nature of the classification can be understood from a very simple picture: Since the eigenstates are degenerate at the TRIM, depending on the system, a band connecting the valence and conductance band may intersect with the Fermi energy even or odd times. The former case is trivial since the system can be continuously deformed (imagine lifting the band above the Fermi energy) and the intersection can be removed, leaving the dispersion with no band connecting the valence and conductance band. In case of an odd number of intersections this is not possible and the system is non-trivial, exhibiting an edge mode. Recall that in the case of a Chern insulator the weighted number of times the connecting band intersects with the Fermi energy, defined the change in the Chern number. In case of the QSHE, the number of Kramers pairs of the edge mode that intersects with the Fermi energy defines the change in a $\mathbb{Z}_2$ invariant. Before we consider the nature of these edge modes, we elaborate a bit more on the construction of the invariant. Similar to the discussion for Chern insulators, the obstruction to construct a basis on the whole Brillouin zone, where the eigenstates are related by the time-reversal operator, proves to be impossible in the non-trivial case. Details can be found in ref. [30]. There are several ways to define a $\mathbb{Z}_2$ invariant [7, 35], one that will be of interest at a later stage was introduced by Fu and Kane [35]. The sewing matrix is defined as

$$w(k) = \langle u_m(k)|T u_n(-k)\rangle,$$

where $|u(k)\rangle$ again denote the occupied Bloch functions and T the anti-unitary time-reversal operator with $T^2 = -1$. w measures the overlap or orthogonality of the Bloch states with their time-reversal partners. It is unitary and furthermore at the TRIM, w is skew-symmetric $w^{\mathrm{T}} = -w$. A skew-symmetric matrix allows for the definition of a Pfaffian, $\mathrm{Pf}(w) = (\det w)^2$. Thus for each TRIM k_a we can define the binary quantity

$$\delta_a = \mathrm{Pf}(w(k_a)) \det(w(k_a))^{-\frac{1}{2}} = \pm 1,$$

and if the Bloch states are chosen continuously, the $\mathbb{Z}_2$ invariant is defined as

$$(-1)^\nu = \prod_a \delta_a, \tag{1.13}$$

where the product runs over all TRIM (of which there are four in two dimensions).

The edge states of the QSHE can be derived in the same fashion as for the IQHE. The simplest model necessarily involves four levels (two levels with different spin). The Hamilto-

---

[11]Since time-reversal symmetry is present it is sufficient to only consider half of the Brillouin zone.

nian (1.7) thus has to be represented in a four-dimensional basis and is given by

$$H(k) = \sum_{i=1}^{5} h_i(k)\Gamma_i + \sum_{i>j} h_{ij}(k)\Gamma_{ij},$$

where the gamma matrices $\Gamma_{i=1,\dots,5}$ obey the Clifford algebra[12] $[\Gamma_i, \Gamma_j]_+ = 2\delta_{ij}$ and $\Gamma_{ij} = -2i[\Gamma_i, \Gamma_j]_-$. Symmetry constraints opposed to the system restrict the gamma matrices further.

Considering the model introduced by Kane and Mele, a linearisation around one of the TRIM, as it was done in the discussion on Dirac Hamiltonians for Chern insulators, leads to the minimal representation

$$H(k) \simeq k_1\Gamma_5 - k_2\Gamma_2 + m\Gamma_1,$$

where we again assume that the sign of the mass m changes along a coordinate y and vanishes at the interface between two different insulators at $y = 0$. The specific representation of the gamma matrices are of no importance at this point and will be discussed later; it is sufficient to understand that they live in the tensor space of spins and the degrees of freedom of the two-level system[13]. However, it is easy to see that the Hamiltonian can be block diagonalised with each block referring two one of the two spin species, $H = \mathrm{diag}(H^\uparrow, H^\downarrow)$ and thus the Schrödinger equations decouples within the spins. These Schrödinger equations are then straightforwardly solved in real space [30], yielding

$$\Psi_{\uparrow/\downarrow}(x, y) \propto \exp[\mp ik_x x] \exp[-\int_0^y m(y')\mathrm{d}y']\hat{e}_{\uparrow/\downarrow},$$

where $\hat{e}_\uparrow = (0, 1, 0, 0)^\mathrm{T}$ and $\hat{e}_\downarrow = (\sigma_1 \otimes \mathbb{1})\hat{e}_\uparrow$. Thus the boundary hosts helical edge states, one state with spin-up moves to the right and the spin-reversed partner moves to the left with the same velocity. These helical edge states are illustrated in fig. 1.8 and the parities of these helical edge states are represented by the $\mathbb{Z}_2$ invariant eq. (1.13).

1.9 Stability of edge states

The robustness of metallic edge states, present due to the bulk boundary correspondence, is protected due to their topological origin. Chiral and helical edge states have been identified at the boundary of a Chern and $\mathbb{Z}_2$ topological insulator, respectively. Chiral edge modes only travel in one direction and simply put, there is just no possibility for backscattering as long as the sample width is larger than the decay length of the edge mode [36]. For

---

[12]Throughout this work we denote (anti-)commutators by $[A, B]_\xi = A \circ B + (\xi)B \circ A$.
[13]Therefore they are in general a tensor product of two Pauli matrices.
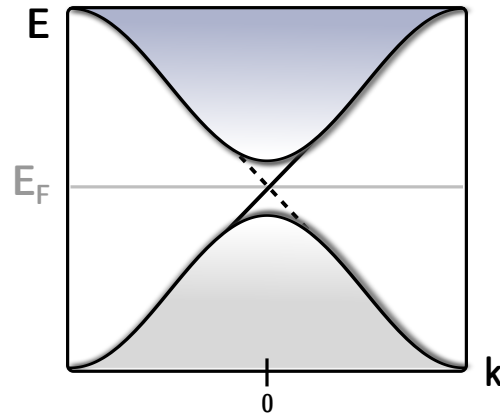
Figure 1.8: Helical edge states of the QSHE. A pair of electrons moving in opposite directions with opposite spin cross the Fermi energy.

the helical edge states in the QSHE the robustness is due to destructive interference of the backscattering paths. Imagine an electron with spin σ travelling along the edge of the QSH insulator. We assume that there is only one pair of edge states. If the electron is reflected by disorder compatible with the symmetry class (i.e. non-magnetic disorder), it has to flip its spin (since it is helical). The two possible paths (illustrated in fig. 1.9) the electron can take during that scatter process will rotate the spin by an angle of $\pm\pi$, depending on which direction it takes, resulting in a total difference of 2π between both paths. Thus for half-integer spin, both paths will interfere destructively[14]. Therefore the presence of time-reversal symmetry protects the edge states by annihilating the possibility of backscattering. On a final note we see that the parity of helical states at one edge indeed relates to the $\mathbb{Z}_2$ invariant eq. (1.13), as an even number of pairs would always give rise to the possibility for the electron to change the channel when scattering at an impurity. The latter would annihilate the destructive interference and lead to localisation effects.

1.10 Topological superconductors

Throughout the text (although at times impertinently concealed for the sake of simplicity) the terms topological insulators and superconductors were bound to each other, without paying any special attention to the latter type of systems. We devote more attention to topological superconductors in the second part of this work, however we shall not leave this introduction without revealing the origin of the term 'topological superconductor'. Although superconductors (Class D, C, DIII, CI), described by a quasi-particle Bogoliubov-de Gennes Hamiltonian, have no bulk gap like insulators, the quasi-particle spectrum is gapped by the

---

[14]Recall that the wave function for a half-integer spin particle changes the sign upon a full rotation of the spin.
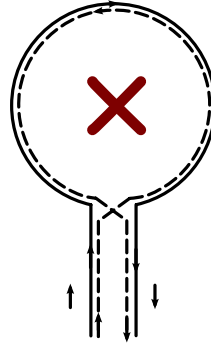
Figure 1.9: Possible trajectories for backscattering of an electron at a non-magnetic impurity (red cross): Clockwise rotation (solid line) and counter-clockwise rotation (dashed). Due to TRS the spin has to reverse in both case (indicated by arrows at the bottom), the total phase change leads to a destructive interference of both paths, and thus TRS protects edge-modes from disorder.

superconducting order parameter Δ due to the intrinsic particle-hole symmetry. Thus, a similar classification of Bogoliubov-de Gennes Hamiltonians, that can not be continuously deformed into one another without closing this gap, is desired. It turns out, that boundary modes of spinless fermions in one dimension in superconducting systems represent a very elusive type of particles called *Majorana fermions*, discussed in the second part of this work.

1.11 Completion of the table and dimensional reduction

Having reviewed the construction of $\mathbb{Z}$- and $\mathbb{Z}_2$-topological invariants for the IQHE and the QSHE, we close this section with a comment on the completion of table 1.2 from an invariants point of view[15]. In a seminal work by Qi *et al.* [27] it was shown that $\mathbb{Z}_2$- topological, time-reversal invariant insulators (breaking chiral symmetry) can be derived from higher dimensional $\mathbb{Z}$-topological insulators using a technique called *dimensional reduction*. Topological invariants were then derived from an effective field theory describing the topological insulator. Ryu *et al.* [3] later constructed representatives of topological insulators (in terms of Dirac Hamiltonians) for all classes in arbitrary dimensions. Again using *dimensional reduction*, the authors extended the earlier work [27] to complete the scheme shown in table 1.2. The concept of dimensional reduction and topological field theory will be discussed in the second chapter. Due to the possibility for more complex structures like knots on two dimensional surfaces, topological insulators in three dimensions are described by a different mechanism. Since this work is mainly considering one- and at times two-dimensional systems, three-dimensional topological insulators exceed the scope of this work (for references

---

[15]Not a point that is invariant.

see [2, 26, 27, 36–40]).

In passing we note that classifications of topological insulators and superconductors in the presence of additional spatial symmetries such as reflection and mirror symmetries have been discussed in [41, 42].

2

Topological invariants in terms of quasiclassical Green's functions

It is not overstating the case to say that the BCS-theory of superconductivity developed in the late 1950s and early 1960s [44–49], is one of the most effective and established theories of modern condensed matter physics. However, being a mean field theory, even in the absence of disorder sophisticated problems involving for example strong magnetic fields, or temperatures far away from the critical temperature T_C, prove difficult (or impossible) to solve. The same is true for heterostructures of superconductor and normal metals. A theory which allows for a significant simplification of the transport equations involved, is the *quasiclassical theory* [16, 17]. Since the late 1960s[1] the quasiclassical theory has become an established technique in mesoscopic (non-equilibrium) superconductivity [51–54] as well as in the theory of quantum transport [55–59]. It combines the classical description of quasi-particles with the quantum description of the internal degrees of freedom. While internal structures such as spin and particle-hole symmetry are described quantum mechanically, the quasi-particles propagate along classical trajectories. One reason for its success is the fact that the relevant spatial scale (coherence length) characterising most common superconductors, proportional to the inverse of the BCS gap, exceeds the Fermi wavelength and thereby justify a quasiclassical approximation (in which the Green's functions vary slowly on the scale of the Fermi wavelength).

An extension of the quasiclassical technique to the topological superconductors systems seems natural. However, before we present the quasiclassical approach to this novel systems, we briefly review the quasiclassical technique in conventional normal metal - superconductor

---

[1]Note that for normal metals, the scheme involved was already discussed in 1964 by Prange and Kadanoff [50].

heterostructres. We restrict ourselves to the bare presentation of the necessary equations and refer to one of the numerous reviews [18, 60–62] for further reading.

2.1 Quasiclassical Green's functions

We start from the well-known Gor'kov Green's function in the Nambu representation $\Psi = (\psi_\uparrow, \bar\psi_\downarrow)^{\mathrm{T}}$, $\bar\Psi = (\bar\psi_\uparrow, \psi_\downarrow)$, where $\psi(x)$ annihilates a fermion at space-time x and $\bar\psi$ creates a fermion at the same position,

$$G = -i\langle \mathcal{T}(\Psi(x) \otimes \bar\Psi(x'))\rangle = \begin{pmatrix} \mathcal{G}(x,x') & F(x,x') \\ \bar{F}(x,x') & \bar{\mathcal{G}}(x,x') \end{pmatrix}.$$

Here $\langle\ldots\rangle$ denotes the quantum average and $\mathcal{T}$ represents the time-ordering operator. In this representation $\mathcal{G}$ and $\bar{\mathcal{G}}$ represent the particle and hole Green's functions, respectively, while $F = -i\langle\mathcal{T}\psi_\uparrow\psi_\downarrow\rangle$ is the pair amplitude or anomalous Green's function[2]. The Gor'kov equations are then given by [18]

$$(G_0^{-1} + i\Delta\sigma_2\delta(x_1 - x_1') - \Sigma)(x_1, x_1') \overset{*}{\otimes} G(x_1', x_2) = \delta(x_1 - x_1'), \tag{2.1}$$

where we assumed that the pairing potential is real. The product $\overset{*}{\otimes}$ includes a convolution over coordinates, Σ denotes the impurity self-energy and the free Green's function is defined as

$$G_0^{-1}(x, x') = \delta(x - x')(\sigma_3\partial_t - H(x)),$$

with the single-particle Hamiltonian H.

For superconductor - normal metal heterostructures the Gor'kov equation turns out to be very cumbersome and a detailed microscopic description is often not needed. A more efficient description can be achieved by a prior identification of the information encoded in the system, which are actually relevant for the phenomena under investigation. To this end, we notice that the Green's function in the Gor'kov equation contains fast oscillating contributions (on the scale of the Fermi wavelength λ_F), representing redundant information. The reason being that the relevant length scales in a superconductor $\xi = v_F/\Delta$ and $\xi_T = v_f/2\pi T$ exceed the Fermi wavelength. In superconducting systems, relevant contributions are produced by quasi-particles confined around the Fermi energy where the Green's function is sharply peaked. A separation of the Green's function into slowly and fast (redundant) oscillating parts is therefore desirable. The latter are associated with oscillations of the Green's function as a function of the relative coordinate $\rho = x - x'$, while the former are produced by oscillations in the centre of mass coordinate $2r = x + x'$. The reduction to relevant information within

---

[2]In case of an s-wave superconductor the anomalous Green's function is related to the pairing potential by $\Delta(x) = -\lambda F(x, x)$, where $\lambda < 0$ is an interaction constant.

the quasiclassical approximation [16, 17] can thus be achieved by averaging out the relative coordinate ρ.

The calculations are conveniently performed using the Wigner-transformation. The convolution in the Gor'kov equations can be expressed using a gradient (Moyal) expansion

$$(A \overset{*}{\otimes} B)(p, r, \epsilon) = e^{\frac{i}{2}(\partial_r^A \partial_p^B - \partial_p^A \partial_r^B)} A(p, r, \epsilon) B(p, r, \epsilon).$$

Given that we are not interested in fast oscillations, the upper product is expanded up to linear order. Starting from the combined Gor'kov equation

$$(G_0^{-1} - \Sigma) \overset{*}{\otimes} G - G \overset{*}{\otimes} ((G_0^{-1})^\dagger - \Sigma) = 0,$$

and neglecting terms of the order $(p - p_F)\partial_r$ and higher orders of $(p - p_F)$ (due to proximity of p to p_F and the slow dependence of G on r), we arrive at

$$i v_F \partial_r G + [\epsilon \sigma_3 + i \sigma_2 \Delta - \Sigma, G]_- = 0. \tag{2.2}$$

Note the enhanced simplicity of this equation compared to the Gor'kov equation (2.1). The fact that equation (2.2) does not depend on the distance to the Fermi momentum $\xi(p) = p^2/2m - \mu \simeq v_F(p - p_F)$, ensures that it is valid for the quasiclassical Green's function

$$g(r, p_F, \epsilon) \equiv \frac{i}{\pi} \int \mathrm{d}\xi(p) G(\xi, p_F, r, \epsilon).$$

Thus the quasiclassical Gor'kov equation, called *Eilenberger equation*, reads

$$i v_F \partial_r g + [\epsilon \sigma_3 + i \sigma_2 \Delta - \Sigma, g]_- = 0. \tag{2.3}$$

Note that we used Σ for both the self-energy and the quasiclassical approximated self-energy. We restricted our discussion to stationary problems. The Eilenberger eq. (2.3) however is not sufficient to uniquely determine g, since g^2 provides an additional solution to eq. (2.3). It turns out that $g^2 = c\mathbb{1}$. The constant c can be derived from the solution of the isotropic Gor'kov equation deep within the superconductor, resulting in the non-linear constraint or normalisation condition

$$g^2 = \mathbb{1}.$$

As a closing remark we note that, in case of one-dimensional geometry (a wire), r is simply given by the coordinate along the wire and $\xi(p)$ can take the two values ± 1 depending on the direction of the moving fermion.

Interfaces between different materials (such as between superconductors and normal metals) lead to discontinuities in g at the transition. At the level of the quasiclassical approxima-

tion, effects of interfaces (or potential barriers) are not taken into account, since information on length scales of the order of the Fermi wavelength are integrated out. Rapid changes of the Green's function at interfaces (or potential barriers) in principle prohibit a quasiclassical approximation. As it turns out, the effect of an interface can be incorporated into the quasiclassical description by effective boundary conditions on g. Such boundary conditions for arbitrary interfaces where first derived by Zaitsev [55] and extensions to other transport problems and circuit theory can be found in ref. [56–59].

2.2 Eilenberger function

Throughout this work we consider disordered quantum wires connected to two clean topological insulators or superconductors, to which refer as terminals. The prototypical setup is illustrated in fig. 2.1. The detailed nature of the terminals depends on the specific model under inspection and both terminals can in principle be in different topological phases. We will show that the topological invariants constructed within this framework, depend solely on the topological phases of the associated terminal Eilenberger functions (or quasiclassical Green's functions), i.e. deep within the terminal. These topological invariants relate to the number of edge states at the boundary between topologically inequivalent terminals. In many cases, one of the terminals can be understood as the trivial vacuum and thus the topological phase of the system is entirely determined by phase of the remaining terminal. In section 4.3 we consider a model in which one terminal is given by a trivial tunnel barrier. It can be shown that the implementation of the latter, within the symmetry class of the system, is compatible with a generic set of boundary conditions imposed on the Eilenberger functions.

In the vicinity of a quantum phase transition separating the topological and trivial insulating phase, the minimal low-energy model is given by a gapped Dirac Hamiltonian (c.f. sec. 1.5). Descriptions and classifications of topological insulators based on this low-energy Dirac models have proven to be very effective [3]. In one-dimensional systems the Hamiltonian becomes linear in momentum, facilitating a formulation of (exact) quasiclassical equations of motion and the construction of the Eilenberger function for the Dirac model (c.f. our discussion in section 2.1). The quasiclassical approximation, discussed in the previous section, thus effectively results in a linearisation of the Hamiltonian. Therefore we confine our discussion to Dirac Hamiltonians and consider the low-energy linearised Hamiltonian $\mathcal{H}$ of a one-dimensional quantum wire,

$$\mathcal{H} = -iv\Gamma\partial_x + \hat{m}. \tag{2.4}$$

Here Γ denotes a single Dirac matrix satisfying $\Gamma = \Gamma^\dagger$, $\Gamma^2 = \mathbb{1}$, v denotes the velocity and $\hat{m}$ is the mass matrix. We refer to the first term on the right-hand side in eq. (2.4) as *kinetic part*. The Hamiltonian $\mathcal{H}$ generally acts on a position depended spinor $\psi(x) = (\psi_R, \psi_L)^{\mathrm{T}}$ belonging to the direct product space of possible spin, particle-hole as well as further subspaces comprising additional quantum numbers like chirality, channels and bands.
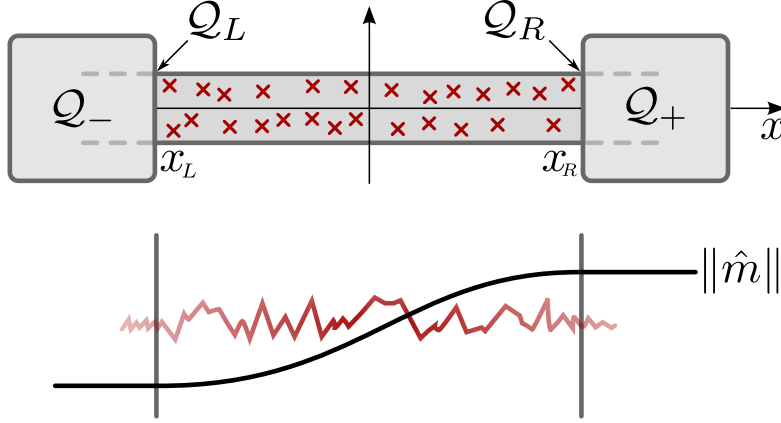
Figure 2.1: Top: Prototypical setup of a disordered (indicated by the red crosses) quantum wire connected to two terminals, with terminal isotropic Eilenberger functions $\mathcal{Q}_\pm$ (see text for definition). At the interface between the scattering region and the terminal, the interface Eilenberger functions are denoted by $\mathcal{Q}_{L/R}$. In the terminals the Eilenberger function $\mathcal{Q}$ is assumed to rapidly converge to $\mathcal{Q}_\pm$. Bottom: The profile of the local gap, here denoted by the formal position dependent norm $\|\hat{m}\|$ of the mass term, induced by the system parameters is shown (black curve). The scattering region is defined as the region where the scattering rate (indicated by the red curve) is comparable to the local gap. Within the terminals the mass saturates to a constant value.

In the process of linearising the original lattice Hamiltonian around some reference Fermi momentum k_F, the introduction of chiral fermions leads to presence of a chiral index (R/L moving fermions, see e.g. [63]). The fermion spinor field is thus represented as a superposition $\psi^\alpha(x) = \psi_R^\alpha(x)e^{ik_Fx} + \psi_L^\alpha(x)e^{-ik_Fx}$, where α denotes the set of the remaining quantum indices. A detailed example of such a linearisation will be given in sec. 4.2.3. We begin with defining the matrix (two-point) Green's function

$$g^{R/A}(x, x'; \epsilon) \equiv vG^{R/A}(x, x'; \epsilon)\Gamma, \tag{2.5}$$

where $G^{R/A}(x, x'; \epsilon) \equiv \langle x|(\epsilon \pm i0^+ - \mathcal{H})^{-1}|x'\rangle$ denote the conventional retarded and advanced Green's functions, respectively. The advantage of this auxiliary construction will become clear momentarily. The evolution operator (or Liouvillian) is defined according to

$$\mathcal{L}_\epsilon \equiv -\frac{i}{v}\Gamma(\hat{\epsilon} - \hat{m}), \tag{2.6}$$

where $\hat{\epsilon}$ denotes the diagonal energy matrix. The Green's function g then evolves according

to the two mutually adjoint differential equations

$$\partial_x g(x, x'; \epsilon) + \mathcal{L}_\epsilon g(x, x'; \epsilon) = -i\delta(x - x'),$$
$$\partial_{x'} g(x, x'; \epsilon) - g(x, x'; \epsilon)\mathcal{L}_\epsilon = i\delta(x - x'). \tag{2.7}$$

From the above expression it can be seen that g is discontinuous at $x = x'$. This discontinuity, is removed in the continuous (one-point) Green's function

$$\mathcal{Q}_\epsilon(x) \equiv \lim_{x' \to x} \left[2ig(x, x'; \epsilon) - \mathrm{sgn}(x - x') \right], \tag{2.8}$$

which is called *Eilenberger function* and which will be our main object of interest. The latter is normalised to unity, $\mathcal{Q}_\epsilon(x)^2 = \mathbb{1}$. By adding up both equations of motions (2.7), the evolution of $\mathcal{Q}$ is described by the following equation of motion

$$\partial_x \mathcal{Q}_\epsilon(x) + [\mathcal{L}_\epsilon, \mathcal{Q}_\epsilon(x)]_- = 0, \tag{2.9}$$

which is called as *Eilenberger equation*, analogous to eq. (2.3).

2.2.1 Symmetries

Possible symmetries present constrain the Hamiltonian $\mathcal{H}$ as it was discussed in section 1.2. We now study the symmetry constraints on g, $\mathcal{L}$ and finally on $\mathcal{Q}$ in succession to the constraints on $\mathcal{H}$. We begin with charge-conjugation symmetry eq. (1.2), where the basis-dependent unitary matrix U_C obeys $U_C U_C^* = \pm\mathbb{1}$. For the Dirac matrix Γ it follows that

$$U_C \Gamma^{\mathrm{T}} U_C^\dagger = \Gamma.$$

Similarly, the advanced and retarded Green's functions inherit charge-conjugation from $\mathcal{H}$, since

$$\begin{aligned}
(G^A(x', x; -\epsilon))^{\mathrm{T}} &= \langle x'| \left((-\epsilon - i0^+ - \mathcal{H})^{-1} \right)^{\mathrm{T}} |x\rangle \\
&= \langle x'| - U_C^\dagger (\epsilon + i0^+ - \mathcal{H})^{-1} U_C |x\rangle \\
&= -U_C^\dagger G^R(x, x'; \epsilon) U_C.
\end{aligned}$$

Hence we find that for g, charge conjugation symmetry translates to

$$g^R(x, x'; \epsilon) = -u_C g^A(x', x; -\epsilon)^{\mathrm{T}} u_C^\dagger, \tag{2.10}$$

where we defined the unitary matrix $u_C \equiv \Gamma U_C$, which obeys $u_C u_C^* = \pm\mathbb{1}$.

Accordingly, the evolution operator and the Eilenberger function obey

$$\mathcal{L}_\epsilon = -u_C \mathcal{L}_{-\epsilon}^{\mathrm{T}} u_C^\dagger, \quad \mathcal{Q}_\epsilon = -u_C \mathcal{Q}_{-\epsilon}^{\mathrm{T}} u_C^\dagger. \tag{2.11}$$

The symmetry constraints on $\mathcal{L}$ and $\mathcal{Q}$ in the presence of time-reversal symmetry (1.1) and sublattice symmetry (1.3) can be derived in the same fashion, leading to

$$u_{\mathrm{T}} \mathcal{L}_\epsilon^{\mathrm{T}} u_{\mathrm{T}}^\dagger = -\mathcal{L}_\epsilon, \quad u_{\mathrm{T}} \mathcal{Q}_\epsilon^{\mathrm{T}} u_{\mathrm{T}}^\dagger = -\mathcal{Q}_\epsilon, \quad \mathcal{L}_\epsilon = U_S \mathcal{L}_{-\epsilon} U_S^\dagger, \quad \mathcal{Q}_\epsilon = U_S \mathcal{Q}_{-\epsilon} U_S^\dagger,$$

where we defined $u_{\mathrm{T}} \equiv \Gamma U_{\mathrm{T}}$, with $u_{\mathrm{T}} u_{\mathrm{T}}^* = \pm \mathbb{1}$ and $U_S U_S^* = \mathbb{1}$. Notice how charge-conjugation opposed to time-reversal symmetry only relates operators with opposite energies with each other, a fact that will be important at a later stage.

2.2.2 Boundary Green's functions and the clean limit

Let us return to the setup illustrated in fig. 2.1. Internal microscopic parameters of the wire are encoded in the mass matrix $\hat{m}(x)$. These parameters vary randomly in space and saturate to some non-random constant values far within the terminals[3]. We denote these isotropic limits by $\hat{m}_\pm$, for the right and left terminal, respectively. Disorder compatible with the symmetries of the wire can then be introduced by splitting the mass $\hat{m}(x)$ into a non-random (external) parameter contribution $\hat{m}_0(x)$, together with a Gaussian distributed random matrix $\delta\hat{m}(x)$ which is only restricted by the present symmetries, i.e. $\hat{m}(x) = \hat{m}_0(x) + \delta\hat{m}(x)$. In the lower part of fig. 2.1 a profile of the mass matrix is illustrated. The width of the region between the two interfaces at $x_{L/R}$, is set by regime where the scattering rate is comparable to the local gap (given by an abstract position-dependent norm $\|\hat{m}(x)\|$), i.e. $\frac{1}{\tau} \simeq \|\hat{m}(x)\|$. Saturation in the terminals is achieved if $\frac{1}{\tau} < \|\hat{m}(x)\|$ and disorder effects can be neglected. We can therefore safely assume that the terminals are disorder-free[4]. We denote the asymptotic Eilenberger functions in the terminals, corresponding to the saturated masses $\hat{m}_\pm$, by[5]

$$\mathcal{Q}_\epsilon(x \to \pm\infty) \equiv \mathcal{Q}_\pm.$$

As we will see later, these isotropic limits encode all informations necessary to determine the topological invariants.

Since in this isotropic limit the Eilenberger function is stationary, the Eilenberger eq. (2.9) reduces to the isotropic Eilenberger equation

$$[\mathcal{Q}_\epsilon, \mathcal{L}_\epsilon]_- = 0,$$

---

[3]For example, in case of a proximity coupled superconductor, the proximity induced order parameter in the wire saturates to a constant value on the scale of the coherence length.

[4]Note that the theory becomes analytically correct in the $x \to \infty$ limit.

[5]Note that we omit the energy subscript whenever possible to simplify the notation.

together with the non-linear constraint $\mathcal{Q}_\epsilon^2 = \mathbb{1}$.

In order to solve these equations, we assume the disorder-free evolution operator $\mathcal{L}_\epsilon$ to be diagonalised as

$$\mathcal{L}_\epsilon = T\hat{\lambda}T^{-1}, \tag{2.12}$$

where T is a transformation matrix and the matrix $\hat{\lambda}$ comprises the eigenvalue structure. Due to the Dirac nature of our Hamiltonian the eigenvalue matrix takes the form

$$\hat{\lambda} = \text{diag}(\lambda_+, \lambda_-) \otimes \Sigma, \tag{2.13}$$

where we $\lambda_\pm$ are eigenvalues (or diagonal matrices of eigenvalues) with positive real parts. The matrix Σ, appearing in the upper expression, is diagonal and incorporates the sign structure and has a vanishing trace $\text{tr}\,\Sigma = 0$. Details of the transformation matrix T are not of interest at this point and it can be calculated for the individual case. According to the definition (2.8), the isotropic Eilenberger equation is then solved by matrices of the form

$$\mathcal{Q}_\epsilon = T\Lambda T^{-1}, \tag{2.14}$$

where the matrix $\Lambda = \text{diag}(\pm 1, \ldots, \pm 1)$ is a diagonal matrix containing only unit-modular entries. The order in which this entries are distributed is determined by the sign of the infinitesimal offset $\epsilon \to \epsilon \pm i0^+$ introduced in the retarded/advanced Green's functions. In order to derive the explicit form of the matrix Λ in eq. (2.14), we consider the momentum representation of the equations of motion, eq. (2.7). The Green's function is translational invariant $g(x, x'; \epsilon) = g(x - x'; \epsilon)$ and its Fourier transform satisfies

$$(i\mathcal{L}_\epsilon - p)\, g(p; \epsilon) = 1.$$

In the diagonalised representation (2.12) yields

$$g(p; \epsilon) = -T \left[p - i\hat{\lambda} \right]^{-1} T^{-1}.$$

Since the real parts of the eigenvalues $\text{Re}\,(\lambda_\pm) > 0$ are positive, one can calculate the inverse Fourier transformation for the retarded Green's function,

$$g(x, x'; \epsilon) = T \left(\int \frac{\mathrm{d}p}{2\pi} \left[p - i\hat{\lambda} \right]^{-1} e^{ipx} \right) T^{-1}$$

$$= -\frac{i}{2} T \left(\Sigma \otimes \mathbb{1} + \text{sgn}(x - x') \right) e^{-\hat{\lambda}|x-x'|} T^{-1}.$$

Note that for $x \neq x'$, the kernel of the upper expression is exponentially decaying, since we defined the eigenvalues $\lambda_\pm$ to be of positive real part. By the same token, we could have chosen a different diagonalisation of $\mathcal{L}$ with negative real parts, resulting in a sign change

in the upper integral. With the definition (2.8) it follows that the sign structure of Λ is fully determined by Σ, or put differently, by the sign of the infinitesimal offset $\epsilon \to \epsilon \pm i0^+$. In order to establish a relation between Σ and Γ, we note that from the definition (2.6), it follows that for high energies ($\epsilon \to \infty$) the evolution operator is approximately given by $-i\Gamma$. In the same limit, T is close to identity $T \simeq \mathbb{1}$ and $\mathcal{Q}$ is almost Λ. If, for simplicity, we assume that Γ is diagonal, we see that $\Gamma \simeq \Sigma$. Of course, if Γ is not diagonal such a simple identification is not possible and more work is necessary to determine the correct sign structure of Λ. This analysis also allows for a very straightforward scheme to construct Λ and therefore $\mathcal{Q}$: Once $\mathcal{L}$ is given in a suitable basis and its eigenvalues are calculated and properly ordered, the proper sign structure of Λ can be calculated directly from the sign of the real part of each eigenvalue of $\mathcal{L}$. A scheme that will be put to use in later calculations.

2.2.3 Transfer matrix

We now turn to the formal solution of the Eilenberger equation for the disordered system. It goes without saying that the solution of the Eilenberger equation in the presence of disorder is a formal construction, in the sense that it depends on the particular realisation of disorder. Given an observable that functionally depends on $\mathcal{Q}$, one needs to average over different realisations in order to be able to draw meaningful results.

As we discussed earlier, the terminals can safely be considered to be disorder-free and the asymptotic values of the terminal Eilenberger functions are $\mathcal{Q}_+$ and $\mathcal{Q}_-$, constructed according to scheme outlined the previous section. Note that $\mathcal{Q}_+$ and $\mathcal{Q}_-$ may in general describe different topological phases. We denote the length of the intermediate region (in which the disorder is comparable to the local gap) by l_x and assume that the mass term, comprising the dependence on the system specific parameters, varies in space in a region $|x| < l_x/2$. By the same token, saturation of the system parameters is achieved at $|x| \gg l_x/2$. The $\mathcal{Q}$-matrices at the interfaces between the terminal regions and the disordered region are denoted by

$$\mathcal{Q}_R = \mathcal{Q}(x_R), \quad \mathcal{Q}_L = \mathcal{Q}(x_L), \tag{2.15}$$

where we defined $x_L = -x_R = l_x/2$. Assuming that the number of modes present in the quantum wire is sufficiently large (i.e. that the characteristic energy length, l_ϵ, exceeds the longitude of the wire, $l_x \gg l_\epsilon$, while its latitude is small in comparison $l_y \ll l_x$), we are in a position to define a transfer matrix[6] M that formally connects both interface Eilenberger functions,

$$\mathcal{Q}_R = M(x_R, x_L) \mathcal{Q}_L M^{-1}(x_R, x_L).$$

The transfer matrix given at an energy ϵ is a function of two positions and functionally

---

[6]In a way this defines our notion of one-dimensional systems.

depends on the disorder configuration. The interface $\mathcal{Q}$-matrices can then be related to the terminal $\mathcal{Q}$-functions $\mathcal{Q}_\pm$. In order to do so, we notice that the transfer matrix M at given energy ϵ can formally be derived from the Eilenberger eq. (2.9) for two arbitrary positions x and x',

$$M_\epsilon(x, x') = \mathcal{P}_x \exp\left[-\int_x^{x'} \mathcal{L}_\epsilon(y) \mathrm{d}y \right] = \mathcal{P}_x \exp\left[\frac{i}{v} \int_x^{x'} \Gamma\left(\hat{\epsilon} - \hat{m}(y)\right) \mathrm{d}y \right], \quad (2.16)$$

where $\mathcal{P}_x$ denotes the path-ordering operator and we made use of definition $\mathcal{L}_\epsilon = -\frac{i}{v}\Gamma(\hat{\epsilon} - \hat{m})$. The relation between the terminal and interface $\mathcal{Q}$-matrices then reads

$$\mathcal{Q}_\pm = M(x, x_{R/L})\mathcal{Q}_{R/L}M^{-1}(x, x_{R/L}), \quad (2.17)$$

in the limit $x \to \pm\infty$.

Since the transfer matrix M_ϵ is based on $\mathcal{L}_\epsilon$, we can formulate symmetry constraints for the transfer matrix M_ϵ. Independent of the present symmetries, M_ϵ obeys the flux conservation [64]

$$M_\epsilon^\dagger \Gamma M_\epsilon = \Gamma. \quad (2.18)$$

To illustrate this property we consider a disordered system which is placed between two semi-infinite leads of finite width, assumed to be perfectly conducting. We impose hard-wall boundary conditions at the transverse surface[7] and therefore the energy of the transverse part of the energy of the wave functions is quantised. The $2N \times 2N$-dimensional transfer matrix M in this scenario (where N relates to the quantised transverse momentum and the factor two accounts for the chirality of the waves) is given by

$$M(\iota, o)^\mathrm{T} = (o', \iota')^\mathrm{T},$$

where ι and o denote the left moving wave vectors, whereas the primed vectors refer to the right moving ones. Recall that M relates flux amplitudes of the left-hands side to the ones on the right-hand side, whereas scattering matrices usually relate incoming to outgoing fluxes. Flux conservation translates to a hyperbolic norm of the vector $(\iota, o)^\mathrm{T}$, $|\iota|^2 - |o|^2 = -|\iota'|^2 + |o'|^2$ and M preserving this norm is thus a pseudo-unitary matrix, i.e. $M \in U(N, N)$. In this case the flux conservation can be represented[8] by $\Gamma = \sigma_3 \otimes \mathbb{1}_N$.

In addition, the non-unitary symmetries T, C and S put the following restrictions on M

$$u_C M_{-\epsilon}^\mathrm{T} u_C^\dagger = M_\epsilon^{-1}, \quad u_\mathrm{T} M_\epsilon^\mathrm{T} u_\mathrm{T}^\dagger = M_\epsilon^{-1}, \quad u_S M_{-\epsilon} u_S^\dagger = M_\epsilon. \quad (2.19)$$

---

[7]However, details of the boundary conditions are of no importance to the theory.

[8]Formally eq. (2.18) defines a pseudo-unitary matrix, $U(p, q) := \{U \in \mathbb{C} \otimes \mathbb{C} | U^\dagger \eta U = \eta\}$ where η is invertible and Hermitian.

A summary of the symmetry relations for all relevant operators can be found in table 2.1 below.

symmetry	Dirac matrix	Q-matrix	transfer matrix
particle-hole (C)	$U_C \Gamma^{\mathrm{T}} U_C^\dagger = \Gamma$	$u_C Q_{-\epsilon}^{\mathrm{T}} u_C^\dagger = -Q_\epsilon$	$u_C M_{-\epsilon}^{\mathrm{T}} u_C^\dagger = M_\epsilon^{-1}$
time-reversal (T)	$U_{\mathrm{T}} \Gamma^{\mathrm{T}} U_{\mathrm{T}}^\dagger = -\Gamma$	$u_{\mathrm{T}} Q_\epsilon^{\mathrm{T}} u_{\mathrm{T}}^\dagger = -Q_\epsilon$	$u_T M_\epsilon^{\mathrm{T}} u_T^\dagger = M_\epsilon^{-1}$
sublattice (S)	$[U_S, \Gamma]_+ = 0$	$U_S Q_{-\epsilon} U_S^\dagger = Q_\epsilon$	$U_S M_{-\epsilon} U_S^\dagger = M_\epsilon$

Table 2.1: Symmetries of the Dirac (Γ), Eilenberger (Q) and the transfer (M) matrices. We defined the matrices $u_i = \Gamma U_i$ with $i = \{C, \mathrm{T}\}$. They satisfy the relations $u_i u_i^* = \pm\mathbb{1}$ and $U_i U_i^* = \pm\mathbb{1}$ with both u_i and U_i being unitary. Note that if all three symmetries are present, the additional relations $U_C = U_S U_T$ and $u_C = U_S u_T$ hold.

2.2.4 Boundary conditions

The transfer matrix relation eq. (2.17) shows that the terminal $\mathcal{Q}$-functions and the interface $\mathcal{Q}$-functions in general do not coincide. In this section we will show, that the physical requirement of a non-divergent $\mathcal{Q}$-function allows the representation of eq. (2.17) in terms of a set of algebraic relations. From this relations we are able to draw conclusions on the pole structure of $\mathcal{Q}$, which in return is used in the construction of the topological invariants at a later stage. In addition, the algebraic relations lay the foundation for a numerical method used to compute the disordered Eilenberger function and to calculate physical observables. The numerical method is extensively discussed in section 4.4.

The transfer matrix M_ϵ is an element of the pseudo-unitary group $U(N, N)$, which is non-compact. Let $w \in u(N, N)$ be an element of the Lie algebra $u(N, N)$ of the pseudo-unitary Lie group $U(N, N)$. w is of the form

$$w = \begin{pmatrix} a & b \\ c & d \end{pmatrix},$$

where $a + a^* = 0$, $d + d^* = 0$ and $b = c^*$. Let w be explicitly given by,

$$w = \begin{pmatrix} 0 & b \\ b^* & 0 \end{pmatrix}.$$

The elements of $W \in U(N, N)$ will then be of the form

$$W = e^{wx} \simeq \begin{pmatrix} \cosh(bx) & \sinh(bx) \\ \sinh(bx) & \cosh(bx) \end{pmatrix}.$$

Consequently, the action of W on a generic matrix in the limit $x \to \infty$, will possibly lead to divergent contributions (proportional to e^{bx}) as well as to convergent contributions (proportional to e^{-bx}). However, the physical quasiclassical Green's functions should be non-divergent and we will see in a moment how this requirement can be translated to an algebraic condition on $\mathcal{Q}_{R/L}$ and $\mathcal{Q}_\pm$. To this end, we will closely follow the technique introduced in ref. [58]. Let us limit our discussion to the right-hand side of the setup shown in fig. 2.1 and drop the energy subscript for clarity. We assume that $x, x' \geq x_R$, i.e. we are to the right of the right terminal. The quasiclassical Green's function $g(x, x')$ at this point reads

$$g(x_R + 0^+, x_R) = -(i/2)(\mathcal{Q}_R + \mathbb{1}), \quad g(x_R, x_R + 0^+) = -(i/2)(\mathcal{Q}_R - \mathbb{1}),$$

which is an immediate consequence of the definition (2.8). Since we are in the terminal, the evolution operator $\mathcal{L}_\epsilon|_{x>x_R}$ is by definition constant in space, which allows for a direct solution of the equations of motion for the quasiclassical Green's function eq. (2.7),

$$g(x, x_R) = e^{-\mathcal{L}(x-x_R)} g(x_R + 0^+, x_R), \quad g(x_R, x) = g(x_R, x_R + 0^+) e^{\mathcal{L}(x-x_R)}.$$

Combined with the upper expression, we find

$$g(x, x_R) = -(i/2) e^{-\mathcal{L}(x-x_R)}(\mathcal{Q}_R + \mathbb{1}), \quad g(x_R, x) = -(i/2)(\mathcal{Q}_R - \mathbb{1}) e^{\mathcal{L}(x-x_R)}.$$

In order to discuss the asymptotics of this expressions, we switch to the basis in which $\mathcal{L}$ is diagonal (cf. eq. (2.12)) and denote the rotated Green's function and Eilenberger function by $\bar{g} = T^{-1} g T$ and $\bar{\mathcal{Q}}_R = T^{-1} \mathcal{Q}_R T$, respectively. The solutions for the equations of motion in this basis are thus given by

$$\bar{g}(x, x_R) = -(i/2) e^{-\hat{\lambda}(x-x_R)}(\bar{\mathcal{Q}}_R + \mathbb{1}), \tag{2.20}$$

$$\bar{g}(x_R, x) = -(i/2)(\bar{\mathcal{Q}}_R - \mathbb{1}) e^{\hat{\lambda}(x-x_R)}, \tag{2.21}$$

where the matrix $\hat{\lambda}$ was defined in eq. (2.13) as the diagonal part of $\mathcal{L}_\epsilon$. Owing to the positivity of $\mathrm{Re}\,(\lambda_\pm)$ in the limit $x \to \infty$, all positive entries (recall the sign structure in $\hat{\lambda}$ was encoded in Σ) of $\hat{\lambda}$ will lead to convergent contributions in eq. (2.20), while all negative entries will lead to divergent terms (vice versa for eq. (2.21)). Without loss of generality we fix the sign structure in $\hat{\lambda}$ to be $1 \otimes \sigma_3$[9], i.e. $\hat{\lambda} = \mathrm{diag}(\lambda_+, -\lambda_+, \lambda_-, -\lambda_-)$. With the help of the projectors $\Sigma_\pm \equiv \frac{1}{2}(\mathbb{1} \otimes (\mathbb{1} \pm \sigma_3))$, we notice that

$$e^{-\hat{\lambda}x} = \Sigma_+ e^{-\hat{\lambda}x} \Sigma_+ + \Sigma_- e^{-\hat{\lambda}x} \Sigma_-.$$

In the limit $x \to \infty$, the first term on the right-hand side of the above expression is convergent, while the second term diverges. We thus conclude that the requirement of convergence

---

[9]All possible quantum indices are left implicit.

of $\bar{g}$,

$$\bar{g}(x, x_R) = -(i/2)\left(\Sigma_+ e^{-\hat{\lambda}(x-x_R)}\Sigma_+ + \Sigma_- e^{-\hat{\lambda}(x-x_R)}\Sigma_-\right)(\bar{\mathcal{Q}}_R + \mathbb{1}),$$
$$\bar{g}(x_R, x) = -(i/2)(\bar{\mathcal{Q}}_R - \mathbb{1})\left(\Sigma_+ e^{\hat{\lambda}(x-x_R)}\Sigma_+ + \Sigma_- e^{\hat{\lambda}(x-x_R)}\Sigma_-\right),$$

is equivalent to the condition

$$(\mathbb{1} - \Lambda)(\bar{\mathcal{Q}}_R + \mathbb{1}) = 0,$$
$$(\bar{\mathcal{Q}}_R + \mathbb{1})(\mathbb{1} + \Lambda) = 0. \tag{2.22}$$

The left terminal can be treated in the same fashion. Using that the Eilenberger function in the right/left terminal was given by $T\Lambda T^{-1} = Q_\pm$, we arrive at

$$(\mathbb{1} \pm \mathcal{Q}_{L/R})(\mathbb{1} \mp \mathcal{Q}_\mp) = 0,$$
$$(\mathbb{1} \pm \mathcal{Q}_\mp)(\mathbb{1} \mp \mathcal{Q}_{L/R}) = 0.$$

In order to obtain a closed expression for $\mathcal{Q}_{R/L}$ in terms of $\mathcal{Q}_\pm$ and the transfer matrix M, we multiply the above equation (2.22) from the left side by M and from the right by M^{-1}, resulting in

$$M(\mathbb{1} + \mathcal{Q}_-)(\mathbb{1} - \mathcal{Q}_L)M^{-1} = \mathbb{1} + M\mathcal{Q}_-M^{-1} - M\mathcal{Q}_L M^{-1} - M\mathcal{Q}_-\mathcal{Q}_L M^{-1}$$
$$= 1 - M\mathcal{Q}_-M^{-1}\mathcal{Q}_R + M\mathcal{Q}_-M^{-1} - \mathcal{Q}_R,$$

where we made use of the eq. (2.15). Combining this with eq. (2.22) we arrive at

$$2 \cdot \mathbb{1} - M\mathcal{Q}_-M^{-1}\mathcal{Q}_R + M\mathcal{Q}_-M^{-1} - \mathcal{Q}_+ - \mathcal{Q}_+\mathcal{Q}_R = 0.$$

The final expressions are then given by

$$\mathcal{Q}_R = \mathbb{1} + \frac{2}{\mathcal{Q}_+ + M\mathcal{Q}_-M^{-1}}(\mathbb{1} - \mathcal{Q}_+),$$
$$\mathcal{Q}_L = \mathbb{1} + (1 - \mathcal{Q}_-)\frac{2}{\mathcal{Q}_- + M\mathcal{Q}_+M^{-1}}, \tag{2.23}$$

where we dropped the explicit space dependence, i.e. $M = M(x_R, x_L)$.

We have thus shown, that the requirement for the non-divergence of the quasiclassical Green's function is equivalent to the set of algebraic relations (2.23). In two final steps the Eilenberger function $\mathcal{Q}(x)$ in the scattering region is obtained by using eqs. (2.23) to construct $\mathcal{Q}_{R/L}$ and a subsequent application of $M(x, x_{R/L})$ to $Q_{R/L}$.

At this point we would like to stress the importance of eqs. (2.23). These relations lay the foundation for an efficient numerical analysis that will be used in chapters 4.4. Within this

method, the transfer matrix is obtained as a numerical solution of a system of linear first-order differential equations (2.7). The terminal Eilenberger functions $\mathcal{Q}_\pm$ are analytically calculated using the scheme outlined in the previous section and the full Eilenberger function for the scattering region is then obtained using eqs. (2.23).

2.3 Topological invariants

In this section, we derive the topological invariants for all five non-trivial symmetry classes in one dimension within the quasiclassical approach. It turns out, that these invariants, which give the number of localised zero-energy states in the system, only depend on the terminal Eilenberger functions $\mathcal{Q}_\pm$. Details of the transfer matrix M_ϵ, which describes the disorder scattering within the wire, turn out to be of no importance. The transfer matrix may affect the spatial profiles of the corresponding zero-energy wave functions, but it does not influence the number of states present. After deriving the invariants we consider a few examples. An extensive example of class D is given in chapter 4. A proof relating the number of zero-energy boundary states to the topological invariants can be found in appendix A.

In order to increase the readability of the following sections, we have summarised the invariants in table 2.2. This allows the reader to temporarily skip the formal derivation of the latter and to return after digesting the less formal examples introduced in section 2.4. Each invariant in tab. 2.2 is presented in a basis in which the symmetries take a particularly simple form. Details will be explained in the actual derivation and we canonically denote the Eilenberger functions in this basis by $\tilde{\mathcal{Q}}$. The subscripts $\pm$ as usual refer to the right and left terminal. In case of the $\mathbb{Z}_2$ classes D and DIII, $\tilde{\mathcal{Q}}$ turns out to be a skew-symmetric matrix and the invariants in this classes can be defined using Pfaffians. Due to the chiral and particle-hole symmetry the $\tilde{\mathcal{Q}}$-matrix splits into two off-diagonal blocks which is indicated by the additional index in $\tilde{\mathcal{Q}}_{i,\pm}$. For the classes characterised by an integer invariant, the $\mathcal{Q}$-matrix decomposes into a block-diagonal structure, which are also labelled by an index i. The invariants in this cases are given in terms of traces of the sub-blocks of $\mathcal{Q}$. Note that the full trace of $\mathcal{Q}$ necessarily vanishes.

2.3.1 Superconducting classes D and DIII

We start with the $\mathbb{Z}_2$-topological superconductors. Our goal is to find a $\mathbb{Z}_2$-topological quantum number which determines the number of zero-energy edge modes present in the system. In case of the superconducting classes, topological edge modes are called Majorana modes and a detailed discussion can be found in the second part of this work. In case of a trivial system, the subgap Andreev bound states will be symmetrically distributed (in energy) around the middle of the gap, due to the BdG structure of the Hamiltonian (see section 3.2.2 for a detailed discussion). These subgap states come in pairs and their distance is determined by the profile of the pairing amplitude in space (the BCS barrier). Since a Majorana mode is an eigenstate of the charge-conjugation operator, it has zero energy and therefore is lacking

Class	T	C	S	top. phase	top. number $\mathcal{M}$
D	0	+1	0	$\mathbb{Z}_2$	$\mathrm{Pf}(\tilde{Q}_+)\,\mathrm{Pf}(\tilde{Q}_-)$
DIII	-1	+1	1	$\mathbb{Z}_2$	$\mathrm{Pf}(\tilde{Q}_{1,+})/\mathrm{Pf}(\tilde{Q}_{1,-})$
BDI	+1	+1	1	$\mathbb{Z}$	$\frac{1}{2}(\mathrm{tr}(Q_{i,+}) - \mathrm{tr}(Q_{i,-}))$
AIII	0	0	1	$\mathbb{Z}$	$\frac{1}{2}(\mathrm{tr}(Q_{i,+}) - \mathrm{tr}(Q_{i,-}))$
CII	-1	-1	1	$\mathbb{Z}$	$\frac{1}{4}(\mathrm{tr}(Q_{i,+}) - \mathrm{tr}(Q_{i,-}))$

Table 2.2: Table of topological invariants $\mathcal{M}$ for all five non-trivial classes in one dimension. The matrices $\tilde{\mathcal{Q}}$ are chosen in a convenient basis, in which the symmetry relations simplify and $\tilde{\mathcal{Q}}$ becomes skew-symmetric. The subscript $\pm$ refers to the saturated $\mathcal{Q}$-functions in the right and left terminals. The additional index i refers to one of the two blocks appearing in the chiral representation. Derivations of the results are discussed in sec. 2.3.1 and 2.3.2.

a partner state (of opposite energy) in the spectrum. Due to the particle-hole symmetry, it is thus impossible to remove it from zero energy and it is topologically protected.

Class D

According to the boundary conditions given in eq. (2.23), the pole structure of $\mathcal{Q}$ is solely determined by the denominator[10]

$$\mathcal{D}(\epsilon) := \mathcal{Q}_+(\epsilon) + M(\epsilon)\mathcal{Q}_-(\epsilon)M^{-1}(\epsilon). \tag{2.24}$$

The energies E_j of the spectrum of Andreev bound states will be given by the solutions of the secular equation $\det \mathcal{D}(E_j) = 0$. A Majorana state will manifest itself through a zero-energy solution $E_0 = 0$ of this equation. In anticipation of a Pfaffian invariant, we define the auxiliary $\mathcal{Q}$-function

$$\tilde{\mathcal{Q}}_\pm(\epsilon) \equiv \mathcal{Q}_\pm(\epsilon)u_C,$$

and $\tilde{\mathcal{D}}(\epsilon) \equiv \mathcal{D}(\epsilon)u_C$. First we recall that in the subgap interval one cannot distinguish between advanced and retarded Green's functions, i.e. $(G^{A/R})^\dagger = G^{A/R}$. As a consequence $\tilde{\mathcal{Q}}_\pm(\epsilon)$ will be skew-hermitian $\tilde{\mathcal{Q}}_\pm^\dagger(\epsilon) = -\tilde{\mathcal{Q}}_\pm(\epsilon)$. Owing to the particle-hole symmetry relations (2.11), the auxiliary matrix $\tilde{\mathcal{Q}}$ obeys

$$\tilde{\mathcal{Q}}_\pm(\epsilon) = -\tilde{\mathcal{Q}}_\pm^{\mathrm{T}}(-\epsilon),$$

---

[10]In order to reduce the number of subscripts, we temporarily promoted $\mathcal{Q}_\epsilon$ to $\mathcal{Q}(\epsilon)$ and $\mathcal{D}(\epsilon)$ likewise.

which at zero energy becomes a skew-symmetric $\tilde{\mathcal{Q}}_\pm^{\mathrm{T}}(0) = -\tilde{\mathcal{Q}}_\pm(0)$ and real $\tilde{\mathcal{Q}}_\pm^*(0) = \tilde{\mathcal{Q}}_\pm(0)$ matrix[11]. Due to the flux conservation (2.18) and particle-hole symmetry (2.19), the denominator $\tilde{\mathcal{D}}$ obeys a similar relation

$$\tilde{\mathcal{D}}(\epsilon)^{\mathrm{T}} = -\tilde{\mathcal{D}}(-\epsilon),$$

which signalises that the pole structure is symmetric around $\epsilon = 0$ and thus Andreev bound states appear in pairs of opposite energies $\pm E_j$. Like $\tilde{\mathcal{Q}}$, $\tilde{\mathcal{D}}$ becomes skew-symmetric and real at zero-energy

$$\tilde{\mathcal{D}}(0) = -\tilde{\mathcal{D}}(0), \quad \tilde{\mathcal{D}}^*(0) = \tilde{\mathcal{D}}(0).$$

The skew-symmetry implies the existence of a Pfaffian and thus the existence of Majorana fermions (zero-energy solutions of the secular equation $\det \mathcal{D} = 0$) is reduced to the solution of the following equation

$$\det \tilde{D} = [\mathrm{Pf}(\tilde{D})]^2 = [\mathrm{Pf}(\tilde{\mathcal{Q}}_+ + M\tilde{\mathcal{Q}}_- M^{\mathrm{T}})]^2 = 0, \tag{2.25}$$

where we dropped the zero-energy argument for brevity and made use of eq. (2.19). It is not the solution of this equation we are actually interested in, but the number of zero-energy solutions. As we will see in a moment, this number can be derived from eq. (2.25). Note however, that the matrix $\mathcal{Q}_+$ is not skew-symmetric and hence we cannot define a Pfaffian for it.

We now address the question whether or not zero-energy solutions are present. To this end, we denote the dimension of $\tilde{\mathcal{D}}$ by $d_\mathcal{D} \times d_\mathcal{D}$. It follows that due to its skew-symmetry, the determinant scales as

$$\det(\tilde{\mathcal{D}}) = \det(-\tilde{\mathcal{D}}^{\mathrm{T}}) = \det((-1)\tilde{\mathcal{D}}) = (-1)^{d_\mathcal{D}} \det \tilde{\mathcal{D}}.$$

Since the latter expression leads to $\det \tilde{\mathcal{D}} = 0$ if $d_\mathcal{D} \in 2\mathbb{N} + 1$ is odd, the rank of $\tilde{\mathcal{D}}$ has to be even. If the rank is even however, the rank-nullity theorem ensures that the nullity (the dimension of the kernel) of $\tilde{\mathcal{D}}$ is even. We denote the nullity by $2\mathcal{N}$ and try to relate the parity of $\mathcal{N}$ to the Eilenberger function. Since the object $\tilde{\mathcal{Q}}_M \equiv M\tilde{\mathcal{Q}}_- M^{\mathrm{T}}$ satisfies all defining properties of $\mathcal{Q}_-$, we introduce the matrix[12] $F \equiv \tilde{\mathcal{Q}}_M^{-1}\tilde{\mathcal{Q}}_+$ and the secular equation becomes $\det(1 + F) = 0$. The task of finding $\mathcal{N}$ can then be reformulated into finding half of the degree of degeneracy (if any) of the eigenvalue $z_n = -1$ of the matrix F, in the secular equation

$$\det(z + F) = 0.$$

---

[11]Both matrices, U_C as well as u_C are symmetric.
[12]We will however, frequently write $\tilde{\mathcal{Q}}_-^{-1}$ instead of $\tilde{\mathcal{Q}}_M^{-1}$.

Let us, for simplicity choose a basis in which charge-conjugation symmetry is represented by the identity, $U_C = \mathbb{1}$ and $u_C = \Gamma$. We refer to this basis as Majorana representation and at zero energy, $\tilde{\mathcal{Q}}_\pm$ is a real skew-symmetric matrix of unit determinant $\det \tilde{\mathcal{Q}}_\pm = 1$. Since $\mathcal{Q}_\pm^2 = \mathbb{1}$ it follows that

$$\tilde{\mathcal{Q}}_\pm = \Gamma \tilde{\mathcal{Q}}_\pm^{-1} \Gamma. \tag{2.26}$$

We denote the dimension of the $\tilde{\mathcal{Q}}_\pm$-matrices by $4M \times 4M$, taking into account the particle-hole, spin and channel subspace as well as further subspaces. From eq. (2.26) it follows that

$$F^{\mathrm{T}} \Gamma F = \Gamma. \tag{2.27}$$

Assuming that the eigenvalues (± 1) of Γ come in pairs, one can rotate $\tilde{F} = UFU^\dagger$ to an orthogonal matrix $\tilde{F}\tilde{F}^{\mathrm{T}} = \mathbb{1}$. Since the unitary transformation U is generally complex, eq. (2.27) defines F to be an element of the complex orthogonal group $O(4M, \mathbb{C})$. Different from orthogonal matrices, the eigenvalues of pseudo-orthogonal matrices are either (± 1) or come in pairs (λ, λ^{-1}), with $\lambda \in \mathbb{C}$ which are not necessarily unimodular[13].

Being a real skew-symmetric matrix, $\tilde{\mathcal{Q}}_\pm$ can be factorised as

$$\tilde{\mathcal{Q}}_\pm = R_\pm \bigoplus_{k=1}^{2M} (ix_k^\pm \sigma_2) R_\pm^{\mathrm{T}} = R_\pm N_\pm (\Sigma_y) N_\pm R_\pm^{\mathrm{T}},$$

where $N_\pm := \bigoplus_{k=1}^{2M} (x_k^\pm)^{\frac{1}{2}} \otimes \mathbb{1}$, $\Sigma_y = \mathbb{1} \otimes \sigma_y$, $\mathbb{R}_\pm \in O(\mathbb{R}, 4M)$ is a real orthogonal matrix, $x_k^\pm > 0$ and $\{\pm ix_k^\pm\}$ is the set of imaginary eigenvalues of $\tilde{\mathcal{Q}}_\pm$.[14] Now, since for the Eilenberger function $\det \tilde{\mathcal{Q}}_\pm = 1$ and $R_\pm \in O(\mathbb{R}, 4M)$, it follows that the determinant of $N_\pm$ is given by

$$\det N_\pm = \prod_{k=1}^{2M} x_k^\pm = 1,$$

and hence

$$\mathrm{Pf}(\tilde{\mathcal{Q}}_\pm) = \det R_\pm.$$

---

[13]Note that eq. (2.27) together with the properties of Γ, defines F to be a pseudo-orthogonal matrix. Eigenvalues of pseudo-orthogonal matrices have precisely the same properties discussed in the text.

[14]Note that in general the decomposition could include zero blocks, but since $\det \tilde{\mathcal{Q}} = 1$ these are excluded.

We return to our object of interest, the secular determinant, which is given by

$$\det(z + \tilde{Q}_-^{-1}\tilde{Q}_+) = \det(\tilde{Q}_-^{-1})\det(z\tilde{Q}_-^{-1} + \tilde{Q}_+)$$
$$= \det(z + \Sigma_y R \Sigma_y R^{\mathrm{T}}) = \det(i\Sigma_y z + iR\Sigma_y R^{\mathrm{T}})$$
$$= \left(\mathrm{Pf}(i\Sigma_y z + iR\Sigma_y R^{\mathrm{T}})\right)^2 =: p^2(z),$$

where we defined the non-orthogonal matrix $R := N_-^{-1} R_-^{\mathrm{T}} R_+ N_+$ and $p(z)$ denotes the characteristic polynomial. The last expression implies that the eigenvalues z_n of the matrix F are double degenerate, hence

$$p(z) = \mathrm{Pf}(i\Sigma_y z + iR\Sigma_y R^{\mathrm{T}}) = \prod_{n=1}^{2M}(z + z_n). \tag{2.28}$$

Let us assume that in the product (2.28), the positive eigenvalues $(+1)$ are present $\mathcal{N}_+$ times while the negative (-1) appear $\mathcal{N}_-$ times. Recall that the remaining $2M - \mathcal{N}_- - \mathcal{N}_+$ eigenvalues come in pairs (λ, λ^{-1}), thus the sum of $\mathcal{N}_+$ and $\mathcal{N}_-$ has to be even and both $\mathcal{N}_\pm$ have to be of the same parity. Therefore, the characteristic polynomial reads

$$p(z) = (z+1)^{\mathcal{N}_+}(z-1)^{\mathcal{N}_-} \prod_{k=1}^{M-\frac{1}{2}(\mathcal{N}_+ - \mathcal{N}_-)}(z + \lambda_k)(z + \lambda_k^{-1}).$$

Setting $z = 0$ we conclude that

$$p(0) = (-1)^{\mathcal{N}_-} = \mathrm{Pf}(iR\Sigma_y R^{\mathrm{T}}) = \det(R_+ R_-).$$

Taking the transfer matrix M into account, we conclude that the parity of $\mathcal{N} = \mathcal{N}_-$ can be express as

$$(-1)^{\mathcal{N}} = \mathrm{Pf}\,\tilde{Q}_+ \,\mathrm{Pf}(M\tilde{Q}_- M^{\mathrm{T}}) = \det M \,\mathrm{Pf}\,\tilde{Q}_- \,\mathrm{Pf}\,\tilde{Q}_+.$$

We recall that at zero energy particle-hole symmetry implies a unimodular determinant for the transfer matrix M, i.e. $\det M = \pm 1$. In addition the transfer matrix $M(x, x')$ is by construction a continuous function of x and x', such that for a fixed initial value $M(x = x') = \mathbb{1}$ the determinant has to be fixed to $\det M = +1$. Hence the parity of $\mathcal{N}$ is solely defined by properties of the terminals, it is given by

$$\mathcal{M} = (-1)^{\mathcal{N}} = \mathrm{Pf}\,\tilde{Q}_- \,\mathrm{Pf}\,\tilde{Q}_+.$$

Which is frequently called *Majorana number* and it shall cross our path again in chapter four.

In appendix A we prove that $\mathcal{M}$ distinguishes the state of the quantum wire with a

Majorana particle ($\mathcal{M} = +1$) and the state without one ($\mathcal{M} = -1$).

Class DIII

Class DIII shares with class D the presence of particle-hole symmetry, but in addition time-reversal symmetry and chiral symmetry are present. The latter are represented by U_i with $U_i U_i^* = +\mathbb{1}$ for $i = T, S$, respectively. Therefore the general statements and constructions for class D are still valid. Due to the chiral symmetry, the Hamiltonian (2.4) can be brought to a block off-diagonal form[15]

$$\mathcal{H} = \begin{pmatrix} & \tilde{D} \\ \tilde{D}^{\mathrm{T}} & \end{pmatrix} = v \begin{pmatrix} & \gamma \\ \gamma^\dagger & \end{pmatrix} \hat{p} + \begin{pmatrix} & m \\ m^\dagger & \end{pmatrix}, \tag{2.29}$$

where $\hat{p} \equiv -i\partial_x$ and $\tilde{D}^{\mathrm{T}} = -\tilde{D}$. In this chiral basis, where $U_S = \sigma_3$, the Dirac matrix becomes

$$\Gamma = \begin{pmatrix} & \gamma \\ \gamma^\dagger & \end{pmatrix},$$

where the entries γ are unitary, symmetric matrices, i.e.

$$\gamma\gamma^\dagger = \mathbb{1}, \quad \gamma^{\mathrm{T}} = \gamma, \quad \gamma\gamma^* = \mathbb{1}.$$

The evolution operator is given by

$$\mathcal{L}_\epsilon = \begin{pmatrix} i\gamma m^\dagger & -i\epsilon\gamma \\ -i\epsilon\gamma^\dagger & i\gamma^\dagger m \end{pmatrix},$$

which shows that at zero energy in the gapped phase, the $\mathcal{Q}$-matrix becomes block-diagonal[16], i.e.

$$\mathcal{Q} = \bigoplus_{i=1}^{2} \mathcal{Q}_i,$$

where both blocks obey the non-linear constraint $\mathcal{Q}_i^2 = \mathbb{1}$. Each sub-block will inherit symmetry constraints from the parent $\mathcal{Q}$-matrix. Particle-hole symmetry leads to the relations

$$\mathcal{Q}_1^{\mathrm{T}} = -\gamma^* \mathcal{Q}_1 \gamma, \quad \mathcal{Q}_2^{\mathrm{T}} = -\gamma \mathcal{Q}_2 \gamma^*,$$

---

[15]In section 2.4 we explicitly demonstrate such a block off-diagonalisation.
[16]We omit the terminal subscript $\pm$ for clarity.

while the fact that in the gapped region no distinction between retarded and advanced components is possible, relates the blocks with each other

$$\mathcal{Q}^\dagger = -\Gamma \mathcal{Q} \Gamma, \quad \mathcal{Q}_1^\dagger = -\gamma \mathcal{Q}_2 \gamma^*, \quad \mathcal{Q}_2^\dagger = -\gamma^* \mathcal{Q}_1 \gamma.$$

In combining both properties, one realises that both blocks are mutually conjugated $\mathcal{Q}_1^* = \mathcal{Q}_2$. The auxiliary matrix $\tilde{\mathcal{Q}}_\pm = \mathcal{Q}_\pm \Gamma$ in this representation is block off-diagonal

$$\tilde{\mathcal{Q}}_\pm = \begin{pmatrix} & \tilde{\mathcal{Q}}_{1,\pm} \\ \tilde{\mathcal{Q}}_{2,\pm} & \end{pmatrix},$$

with skew-symmetric blocks

$$\tilde{Q}_1 \equiv \mathcal{Q}_1 \gamma, \quad \tilde{\mathcal{Q}}_1^{\mathrm{T}} = -\tilde{\mathcal{Q}}_1;$$
$$\tilde{Q}_2 \equiv \mathcal{Q}_1 \gamma^*, \quad \tilde{\mathcal{Q}}_2^{\mathrm{T}} = -\tilde{\mathcal{Q}}_2,$$

which are mutually conjugated $\tilde{\mathcal{Q}}_1^* = \tilde{\mathcal{Q}}_2$.

By the same token, flux conservation and the symmetry constraints of class DIII ensure that the general form of the transfer matrix M at zero energy is given by

$$M = \mathrm{diag}(M_1, M_1^*),$$

with $\gamma M_1^{\mathrm{T}} \gamma^* = M_1^{-1}$.

The construction of the $\mathbb{Z}_2$-invariant for class DIII is in close proximity to the previous construction in class D. However, we point out that the blocks $\tilde{\mathcal{Q}}_{i=1,2}$ have non-unity determinants, $\det \tilde{\mathcal{Q}}_1 = (\det \mathcal{Q}_2)^* = \det \gamma$. Starting point is again the secular equation at zero energy

$$\det \mathcal{D}_1 = \det(\tilde{\mathcal{Q}}_{1,+} + M_1 \tilde{\mathcal{Q}}_{1,-} M_1^{\mathrm{T}}) = 0,$$

and we denote by $2\mathcal{N}$ the number of solutions thereof. Following the lines of the previous proof for class D, we define the matrix[17] $F_1 = \tilde{\mathcal{Q}}_{1,-}^{-1} \tilde{\mathcal{Q}}_{1,+}$ and analyse the secular determinant

$$g(z) = \det(z + F_1).$$

The matrix F_1 inherits symmetry constraints from $\tilde{\mathcal{Q}}$ and Γ and it is easy to see that

$$F_1^{\mathrm{T}} \gamma F_1 = \gamma.$$

---

[17]We redefine the terminal Eilenberger function according to $\tilde{\mathcal{Q}}_{1,-} \to M_1 \tilde{\mathcal{Q}}_{1,-} M_1^{\mathrm{T}}$ but keep the notation for the sake of clarity.

Since γ was symmetric, F_1 is similar to a complex orthogonal matrix[18]. Thus the eigenvalues z_n are either equal to (± 1) or they again come in pairs (λ, λ^{-1}), with $\lambda \in \mathbb{C}$ being a complex number. In order to construct the topological invariant, we note that

$$g(z) = \det(z + \tilde{\mathcal{Q}}_{1,-}^{-1}\tilde{\mathcal{Q}}_{1,+}) = \det(z\tilde{\mathcal{Q}}_{1,-} + \tilde{\mathcal{Q}}_{1,+})/\det(\tilde{\mathcal{Q}}_{1,-}) = p^2(z),$$

where the characteristic polynomial $p(z)$ is given by (recall the sub-blocks are again skew-symmetric)

$$p(z) \equiv \mathrm{Pf}(z\tilde{\mathcal{Q}}_{1,-} + \tilde{\mathcal{Q}}_{1,+})/\mathrm{Pf}(\tilde{\mathcal{Q}}_{1,-}) = \prod_{n=1}^{2M}(z + z_n).$$

We observe that all eigenvalues of F_1 are double degenerate. The degree of degeneracy $\mathcal{N}$, which equals the number of zero eigenvalues of the operator $\mathcal{D}_1$, is even. Thus, following the arguments of our discussion on class D, we conclude that the parity of $\mathcal{N}/2$ is given by

$$(-1)^{\mathcal{N}/2} = p(0) = \mathrm{Pf}(\tilde{\mathcal{Q}}_{1,+})/\mathrm{Pf}(\tilde{\mathcal{Q}}_{1,-}).$$

Taking into account that $\det\tilde{\mathcal{Q}}_{1,\pm} = \det\gamma$, the above expression indeed takes the values ± 1. We will see later that $\mathcal{N}$ presents the total number of localised zero-energy states (with Kramer's degeneracy taken into account). The $\mathbb{Z}_2$-invariant for class DIII is thus given by

$$\mathcal{M} = (-1)^{\mathcal{N}/2} = \mathrm{Pf}(\tilde{\mathcal{Q}}_{1,+})/\mathrm{Pf}(\tilde{\mathcal{Q}}_{1,-}).$$

2.3.2 Classes with $\mathbb{Z}$-topological quantum numbers

We now turn to the three remaining $\mathbb{Z}$-topological classes BDI, CII and AIII. Since all three symmetry classes are chiral, we work in the chiral basis ($U_S = \sigma_3$) where the generic Dirac Hamiltonian (1.11) becomes block off-diagonal,

$$\mathcal{H} = \begin{pmatrix} & h \\ h^\dagger & \end{pmatrix}. \tag{2.30}$$

Class BDI

Class BDI shares the same symmetries as class DIII apart from the fact that U_T is now symmetric[19]. We choose a representation in which time-reversal symmetry is represented by the identity, the blocks h in eq. (2.30) become real matrices and the Dirac matrix Γ in the

---

[18]Or put differently, F is a pseudo-orthogonal matrix.
[19]Recall $u_{i=C,T} \in U(N)$ with $u_i u_i^* = \pm \mathbb{1}$ and hence u_i is either symmetric $(+1)$ or skew-symmetric (-1).

kinetic part of $\mathcal{H}$ has to be purely imaginary. We therefore set

$$\Gamma = \begin{pmatrix} & i\gamma^{\mathrm{T}} \\ -i\gamma^{\mathrm{T}} & \end{pmatrix},$$

with γ real, and the normalisation $\Gamma^2 = \mathbb{1}$ ensures that γ is a real orthogonal matrix. Accordingly, the Eilenberger $\mathcal{Q}$-function is then constructed as usual and decomposed into two real sub-blocks $\mathcal{Q} = \oplus_{i=1}^{2}\mathcal{Q}_i$, where both blocks are symmetry related,

$$\mathcal{Q}_1^{\dagger} = -\gamma\mathcal{Q}_2\gamma^{\dagger}, \quad \mathcal{Q}^{\dagger} = -\Gamma\mathcal{Q}\Gamma. \tag{2.31}$$

Note that there is no need to introduce the auxiliary Eilenberger function $\tilde{\mathcal{Q}}$, since we do not rely on skew-symmetry here.

The $\mathbb{Z}$ invariant in class BDI is then given by

$$\mathcal{M} = \frac{1}{2}\left(\operatorname{tr}\mathcal{Q}_{i,+} - \operatorname{tr}\mathcal{Q}_{i,-}\right).$$

To prove that the number of zero energy states (of each sub-block) is given by $\mathcal{M}$ we again consider the secular equation[20] $\det\mathcal{D}_i = \det(\mathcal{Q}_{i,-} + \mathcal{Q}_{i,+}) = 0$. Each sub-block $\mathcal{Q}_{i,\pm}$ can be diagonalised as

$$\mathcal{Q}_{i,\pm} = T_{i,\pm}\Lambda_{i,\pm}(T_{i,\pm})^{-1},$$

where the signature matrices are given by

$$\Lambda_{i,\pm} = \begin{pmatrix} \mathbb{1}_{M-n_{\pm}} & \\ & -\mathbb{1}_{n_{\pm}} \end{pmatrix},$$

with M being the dimension of the sub-block and $n_{\pm}$ is the number of negative eigenvalues of $\Lambda_{i,\pm}$. With $T_i := (T_{i,-})^{-1}T_{i,+}$ we may rewrite the secular equation as follows

$$\det(\mathbb{1} + \Lambda_{i,-}T_i\Lambda_{i,+}T_i^{-1}) = 0.$$

The matrices T_i are composed by rectangular matrices, the size of each matrix is given according to

$$\left(\begin{array}{c|c} (M-n_-) \times (M-n_+) & (M-n_-) \times n_+ \\ \hline n_- \times (M-n_+) & n_- \times n_+ \end{array} \right).$$

---

[20] We again introduce the object $\mathcal{Q}_M$ which has the same defining properties as $\mathcal{Q}_i$. Desisting from the introduction of a new notation and using the properties of the determinant in eq. (2.25), we arrive at this expression.

The secular matrix $\mathcal{D}_i$ therefore takes the form

$$T_i + \Lambda_{i,-}T_i\Lambda_{i,+} = 2 \begin{pmatrix} t_{(M-n_-)\times(M-n_+)} & \\ & t_{n_-\times n_+} \end{pmatrix},$$

where t_d denotes a rectangular block matrix of dimension d. Again, thanks to the rank-nullity theorem, there are at least $\mathcal{N} \equiv |n_- + n_+|$ independent solutions of the secular equation and thus we conclude

$$\mathcal{M} = \frac{1}{2}(\operatorname{tr} \mathcal{Q}_{i,+} - \operatorname{tr} \mathcal{Q}_{i,+}) = \frac{1}{2}(\operatorname{tr}\Lambda_{i,+} - \operatorname{tr}\Lambda_{i,-}) = \frac{1}{2}(M - 2n_+ - (M - 2n_-)) = \pm\mathcal{N}.$$

Classes AIII and CII

In case of class CII, the blocks h in eq. (2.30) are not real but satisfy the constraint

$$h = \tau_2 h^* \tau_2,$$

where $\tau_{i=1,2,3}$ are Pauli matrices acting in spin-space now. The same is true for the entries of the Dirac matrix

$$\gamma = \tau_2 \gamma^* \tau_2.$$

Apart from this, the relations (2.31) still hold. Taking the time-reversal symmetry ($T^2 = -1$) into account, one finds[21]

$$\mathcal{Q}_i^* = \tau_2 \mathcal{Q}_i \tau_2.$$

Time-reversal symmetry does not play any role in the upper derivation of the topological invariant, neither does charge-conjugation symmetry. The derivation is therefore applicable for all chiral classes leading to the same invariant as discussed above. There is however, an additional factor $\frac{1}{2}$ appearing in class CII, since all zero-energy states come in pairs (they are two-fold degenerate) due to Kramer's theorem (recall $T^2 = -1$). Thus including this additional factor, the invariant counts the number of Kramers pairs.

This completes the construction of the topological invariants in terms of the terminal Eilenberger $\mathcal{Q}$-functions. The technical proof identifying the number of zero-energy bound states with the topological invariants, is evacuated to the appendix A.

---

[21] Note that in general on finds $\mathcal{Q}^* = U_{\mathrm{T}}\mathcal{Q}U_{\mathrm{T}}$, which in the case of BDI (in which we can choose $U_T = \mathbb{1}$) leads to real blocks.

2.4 Examples

We now present some well-deserved examples, in particular one example for a $\mathbb{Z}$-topological insulator of class DIII and one for a $\mathbb{Z}_2$-topological insulator of class AIII (or BDI). For class D we refer to the second part of this work as we devote an entire chapter to Majorana quantum wires of class D. In addition, an example of class BDI (as a single-channel reduction of class D multi-channel wires) can be found in the same chapter.

2.4.1 Class DIII: $d_{x^2-y^2}$-wave superconductor with Rashba spin-orbit coupling

Before we turn to concrete model, let us first make a few general remarks. Earlier we have argued that in class DIII, due to its chiral nature, the Hamiltonian can be brought to a block off-diagonal form with skew-symmetric blocks and that the Eilenberger function $\mathcal{Q}$ becomes block diagonal. Consider the spinors $\Psi = (\psi_\uparrow, \psi_\downarrow, \bar{\psi}_\uparrow, \bar{\psi}_\downarrow)^{\mathrm{T}}$ and $\bar{\Psi} = (\bar{\psi}_\uparrow, \bar{\psi}_\downarrow, \psi_\uparrow, \psi_\downarrow)$ in the direct product space of particle-hole and spin space (additional structure is again left implicit). The most general Bogolioubov-de Gennes Hamiltonian describing the wire is given by

$$\mathcal{H} = \frac{1}{2} \int \bar{\Psi}(x)\, H \Psi(x)\, \mathrm{d}x = \frac{1}{2} \int \bar{\Psi}(x) \begin{pmatrix} \hat{h} & \hat{\Delta} \\ \hat{\Delta}^* & -\hat{h}^{\mathrm{T}} \end{pmatrix} \Psi(x)\, \mathrm{d}x, \qquad (2.32)$$

where the order parameter is skew-symmetric, $\hat{\Delta}^{\mathrm{T}} = -\hat{\Delta}$. For readability we use σ_i and τ_i for Pauli matrices acting in particle-hole space and spin space, respectively, i.e $\sigma_i = \sigma_i^{\mathrm{ph}}$, $\tau_i = \sigma_i^{\mathrm{sp}}$. In this representation time-reversal, particle-hole and chiral symmetry are represented by $U_{\mathrm{T}} = \mathbb{1} \otimes \tau_2$, $U_C = \sigma_1 \otimes \mathbb{1}$ and $U_S = \sigma_1 \otimes \tau_2$, respectively. Note that $U_i U_i^* = +\mathbb{1}$ and $U_{\mathrm{T}} U_{\mathrm{T}}^* = -\mathbb{1}$ for $i = C, S$, defining the symmetry class DIII. The matrices $\hat{h}$ and $\hat{\Delta}$ in eq. (2.32) obey the symmetry constraints $\tau_2 \hat{h}^{\mathrm{T}} \tau_2 = \hat{h}$ and $\tau \hat{\Delta}^* \tau_2 = \hat{\Delta}$. To illustrate the block off-diagonalisation of $\mathcal{H}$, we introduce a unitary transformation V which acts on the spinors $\Psi' = V\Psi$. The rotated Hamiltonian is then given by $H' = V H V^\dagger$, and the symmetries in this basis take the form $U_S' = V U_S V^\dagger$, while $U_i' = V^* U_i V^\dagger$ for $i = C, \mathrm{T}$. We fix the unitary transformation $V = \frac{1}{\sqrt{2}}(\mathbb{1} \otimes \tau_2 + \sigma_2 \otimes \tau_3)$. Using the hermiticity of V, it follows that the bilinear form $\bar{\Psi} H \Psi$ transforms as $\bar{\Psi} H \Psi = \bar{\Psi}' H \Psi'$, and the symmetry matrices take the particularly simple form, $U_S' = \sigma_3$, $U_C' = \sigma_1$ and $U_{\mathrm{T}}' = \sigma_2$. The Hamiltonian H' thus decomposes into the block off-diagonal form

$$H' = \begin{pmatrix} & D \\ D^\dagger & \end{pmatrix}, \qquad (2.33)$$

with $D^{\mathrm{T}} = -D$, where $D = -\tau_1(ih\tau_3 - \Delta\tau_1)$ and $D^\dagger = \tau_3(ih\tau_1 - \Delta\tau_3)$. Taking an additional chiral (R/L) structure[22] in the spinors into account, the symmetry matrices U_{T} and U_C act

---

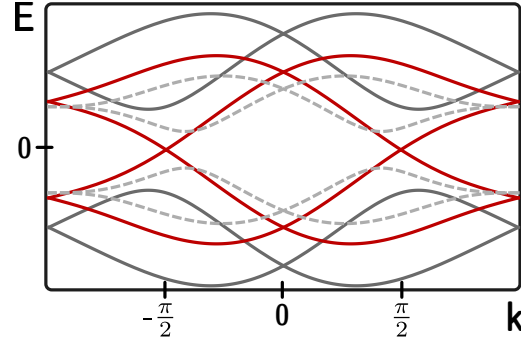[22]Due to the linearisation around the Fermi momenta.

Figure 2.2: Spectrum of $d_{x^2-y^2}$-wave superconductor with Rashba spin-orbit coupling for different values of μ. $\mu > \alpha$ (grey solid curve), $\mu < \alpha$ (light grey dashed curve) and $\mu = \alpha$ (red solid curve). Spectrum derived from eq. 2.4.1.

in the chiral space, $U_{T/C} \otimes c_1$, where $c_i = \sigma_i^{RL}$ are the Pauli matrices acting in this chiral space. The blocks in the rotated Hamiltonian (2.33) are then related by $c_1 D^T c_1 = -D$. The skew-symmetry of the blocks is restored by defining

$$\tilde{H} = \begin{pmatrix} c_1 & \\ & \mathbb{1} \end{pmatrix} H' \begin{pmatrix} c_1 & \\ & \mathbb{1} \end{pmatrix} \equiv \begin{pmatrix} & \tilde{D} \\ \tilde{D}^\dagger & \end{pmatrix}.$$

With this additional chiral structure the unitary transformation V' becomes

$$V' = \begin{pmatrix} c_1 & \\ & \mathbb{1} \end{pmatrix} V = \frac{1}{\sqrt{2}} \begin{pmatrix} \tau_1 \otimes c_1 & -i\tau_3 \otimes c_1 \\ i\tau_3 \otimes \mathbb{1} & \tau_1 \otimes \mathbb{1} \end{pmatrix}_{ph},$$

and with redefined spinors[23], $\Phi \equiv V'\Psi$ the Hamiltonian reads

$$\mathcal{H} = \frac{1}{2} \int \bar{\Phi}(x)\, \tilde{H}\, \Phi(x)\, \mathrm{d}x,$$

which is indeed block off-diagonal with skew-symmetric blocks.

We now consider a one-dimensional $d_{x^2-y^2}$-wave superconductor with Rashba spin-orbit coupling. In ref. [65] it was shown that such a system in strictly one dimension hosts a Majorana Kramers doublet at each end of the topological superconductor. Such a doublet is a pair of Majorana end states that is protected by time-reversal symmetry. Upon introducing an external magnetic field, the system is driven into class D removing the doublet and leaving the system with a single Majorana end state at each end of the wire (cf. chapter 4.1). In

---

[23]Note that $\bar{\Phi} = \Phi^T \cdot (\sigma_1 \otimes c_1)$.

momentum space, the Hamiltonian is given by eq. (2.29) with

$$h_k = -2t\cos(k) - \mu + \alpha\sin(k)\tau_2, \quad \Delta_k = i\tau_2\Delta\cos(k),$$

where t is the hopping amplitude, Δ is the superconducting pairing amplitude and α denotes the Rashba spin-orbit strength [65]. The spectrum is illustrated in fig. 2.2 for different values μ. The system is in the topologically non-trivial phase provided that $|\alpha| > |\mu|$, and due to Kramers degeneracy each state is double degenerate. For the block D_k we find

$$D_k = (2t\cos(k) + \mu - i\Delta\cos(k))\tau_2 + \alpha\sin(k),$$

which satisfies $D_{-k}^{\mathrm{T}} = -D_k$. Assuming that $t \ll \max\{\mu, \alpha, \Delta\}$, one can linearise the Hamiltonian around the two Fermi momenta $k_\pm = \pm\pi/2$ (see fig. 2.2) and with $k_\pm = \pm\pi/2 + p$ one obtains two chiral copies of D,

$$D_p^R = (-(v - i\Delta)p + \mu)\tau_2 + \alpha, \quad D_p^L = ((v - i\Delta)p + \mu)\tau_2 - \alpha,$$

where we set $v = 2t$. The blocks are related via $(D_p^R)^{\mathrm{T}} = -D_{-p}^L$ and hence, the operator

$$\tilde{D}_p = \begin{pmatrix} & D_p^L \\ D_p^R & \end{pmatrix}$$

is skew-symmetric. Note that the Pfaffian[24] $\mathrm{Pf}\,\tilde{D}_{p=0} = \mu^2 - \alpha^2$, indicating the two distinct phases discussed earlier.

To construct the terminal Eilenberger function we note that

$$\gamma = \frac{\Delta + iv}{\sqrt{\Delta^2 + v^2}}(c_2 \otimes \tau_2).$$

The evolution operator for the clean case is easily constructed and is given by

$$\mathcal{L}_\epsilon = \begin{pmatrix} L_1 & -i\epsilon\gamma \\ -i\epsilon\gamma^\dagger & L_2 \end{pmatrix},$$

where

$$L_{1,2} = \frac{\Delta \pm iv}{\sqrt{\Delta^2 + v^2}}(\mu c_3 \mp \alpha\tau_2).$$

The $\mathcal{Q}$-matrix is as usual constructed by considering the sign of the real part of the eigenvalues

---

[24]The Pfaffian is well defined since $\tilde{D}_{p=0}$ is skew-symmetric matrix.

of[25] $\mathcal{L}_{\epsilon=0}$,

$$\Lambda = \begin{cases} c_3, & \mu > \alpha \\ -\sigma_3 \otimes \tau_2, & \mu < \alpha. \end{cases}$$

Finally the block matrices $\tilde{\mathcal{Q}}_{1,2}$ are given by

$$\tilde{\mathcal{Q}}_{1,2} = \frac{\Delta \pm iv}{\sqrt{\Delta^2 + v^2}} \begin{cases} -ic_1 \otimes \tau_2, & \mu > \alpha \\ \pm c_2, & \mu < \alpha \end{cases},$$

and their Pfaffians (in units of $(\frac{\Delta \pm iv}{\sqrt{\Delta^2 + v^2}})^2$) are given by

$$\operatorname{Pf} \tilde{\mathcal{Q}}_{1,2} = \begin{cases} -1, & \mu > \alpha \\ +1, & \mu < \alpha. \end{cases}$$

Replacing the left terminal in our setup (fig. 2.1) with the trivial vacuum, we find that $\mathcal{M} = \operatorname{Pf} \tilde{\mathcal{Q}}_{i,+} / \operatorname{Pf} \tilde{\mathcal{Q}}_{i,-} = \operatorname{Pf} \tilde{\mathcal{Q}}_{i,-} = \pm 1$, as desired.

2.4.2 Class AIII/BDI: Su-Schrieffer-Heeger model

For class AIII we consider the Su-Schrieffer-Heeger (SSH) model of a conducting poly-acetylene [66]. The model describes spinless fermions on a one-dimensional lattice with alternating hopping amplitudes, and is illustrated in fig. 2.3. Due to the alternating hopping amplitudes the chain exhibits an energy gap separating the highest occupied state and the lowest unoccupied state of the bulk, therefore describing a band insulator. The Hamiltonian is given by

$$H = \psi_k^\dagger h(k) \psi_k,$$

where $\psi_k^\dagger = (c_{A,k}^\dagger, c_{B,k}^\dagger)$ and $c_{i,k}^\dagger$ creates a fermion at site i with momentum k. If we denote the hopping amplitudes for sites A and B by t_1 and t_2, respectively, we find

$$h(k) = (t_1 - t_2 \cos(k))\sigma_x + t_2 \sin(k)\sigma_y. \tag{2.34}$$

The model exhibits two limits in which it becomes particularly simple, in which the system is fully dimerised. To this end consider the hopping t_2 to be zero, i.e. there is no inter-cell hopping. In this case the chain breaks apart into a series of cells (dimers). The Hamiltonian in this case reads $h(k) = \sigma_x$ (we choose $t_1 = 1$ for simplicity). In the opposite limit, the inter-cell hopping is kept finite ($t_2 = 1$) but the intra-cell hopping vanishes, $t_1 = 0$. The

---

[25]Note that we skip trivial products with the identity, i.e. $c_3 = \sigma_0 \otimes c_3 \otimes \tau_0$, whenever possible.
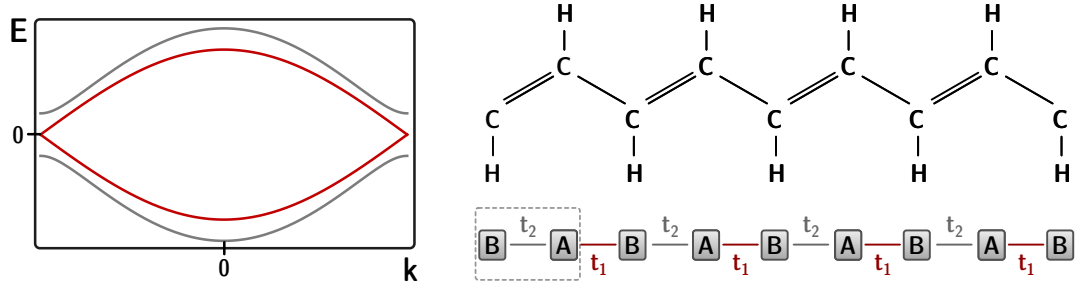
Figure 2.3: Left: Band structure of the poly acetylene chain for $t_1/t_2 = 1$ (red curve) and $t_1/t_2 = 2/3$ (grey curve). Right: Poly acetylene chain and the corresponding SSH model. A unit cell consists of two atoms A and B and is indicated by a dashed rectangle. Inter-cell hopping (red) and intra-cell hopping (grey) are present.

Hamiltonian in this limiting case reads

$$H(k) = \sigma_x \cos(k) + \sigma_y \sin(k).$$

At the chains edges the cells break apart into two monomers, of which one is coupled to the neighbouring cell. Since the system is chiral, the corresponding eigenstates of the uncoupled monomers have energy zero and the bulk gap is closed. Note that these edges might not necessarily be the real end of the full chain, but could be local distortions such as disorder. Figure 2.3 shows the band structure of the SSH model for different ratios of t_1/t_2. We are now in a position to linearise the Hamiltonian (2.34) around $p = k - \pi$ and find

$$h(p) \simeq (t_1 - t_2)\sigma_x - t_2\sigma_y p.$$

After identifying $\Gamma = -\sigma_y$, $v = t_2$ and $\hat{m} = (t_1 - t_2)\sigma_x$, the evolution operator reads

$$\mathcal{L}_\epsilon = -\frac{i}{t_2} \left(\hat{\epsilon} - (t_1 - t_2)\sigma_x\right) \sigma_y.$$

The Eilenberger function is as usual constructed using the sign-structure of the real part of the eigenvalues $\lambda_\pm$ of $\mathcal{L}_{\epsilon=0}$,

$$\lambda_\pm = \pm \left((t_1 - t_2)/t_2\right),$$

and it trivially follows that $\mathcal{Q}$ is given by

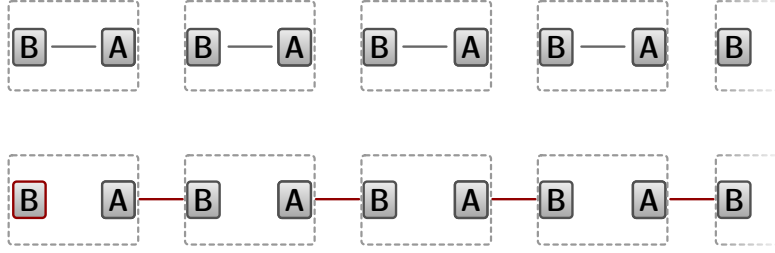$$\mathcal{Q} = \eta\sigma_z,$$

Figure 2.4: Two limiting cases of the SSH model. Top: Pure intra-cell hopping corresponds to the trivial case. Bottom: Pure inter-cell hopping corresponds to the non-trivial case. In the latter case, each edge contains a singe zero-energy eigenstate (red boundary).

where $\eta = \text{sgn}\left[\text{Re}\left((t_1 - t_2)/t_2\right)\right]$. If we take two terminals with equivalent η ($\eta_+ = \eta_-$), the system exhibits no boundary states. If however, the phases of the terminals are inequivalent ($\eta_+ \neq \eta_-$), a distortion in the chain is present at which a boundary mode is present. The topological invariant is then given by

$$\mathcal{M} = \frac{1}{2}(\text{tr }\mathcal{Q}_{1,+} - \text{tr }\mathcal{Q}_{1,-}) = \frac{1}{2}(\eta_+ - \eta_-) = \delta_{\eta_+, \eta_-}.$$

Note that in the case of $t_1 = t_2$ one recovers the usual tight-binding problem (signalising a gap closure). We also note that for real hopping amplitudes $t_i = 1 + (-1)^{i+1}\alpha \in \mathbb{R}$ the system belongs to class BDI.

2.5 Two-dimensional topological insulators and superconductors

With the one-dimensional case checked, it is natural to consider a possible extension to two dimensions. It turns out, that the construction of the quasiclassical $\mathcal{Q}$-function can be extended to two dimensions. The latter is possible, if the second coordinate in subjected to periodic boundary conditions, allowing for a mixed (coordinate and momentum) representation of $\mathcal{Q}$. By representing the (non-)linear response kernel, appearing as a coefficient in a Chern-Simons effective action, in terms of $\mathcal{Q}$-matrices the generalisation to two dimensions is completed. In case of $\mathbb{Z}_2$-topological insulators this procedure involves a dimensional reduction from a three- or four-dimensional parent system. Before we plunge into the details of this extension, we shortly comment on the concept of dimensional reduction within context of topological insulators and superconductors.

2.5.1 Dimensional reduction

In a seminal work by Zhang *et. al.* [27] the concept of dimensional reductions (or Kaluza-Klein compactification [67]) was introduced within the context of time-reversal invariant

topological insulators. In a later work Ludwig *et al.* extended this method to the remaining symmetry classes, [3]. In ref. [27], the reduction was based on a topological field theoretical description [68]. We review the basic ideas behind the technique, and highlight the important aspects and restrict ourselves to the discussion of Dirac Hamiltonians.

The general strategy can be summarised as follows: Given an even-dimensional topological insulator characterised by an integer[26], and ignoring the complex cases A and AIII (since they are either trivial or $\mathbb{Z}$-topological insulators), can we construct from it a topological invariant in lower dimensions, i.e. by reducing the dimension of our parent system? Table 1.2 shows a reappearing pattern $\mathbb{Z} \to \mathbb{Z}_2 \to \mathbb{Z}_2$ if one reduces the symmetries from $d \to d-1 \to d-2$. A $\mathbb{Z}_2$ classification in the first $(d-1)$ or second descendants $(d-2)$ is possible, provided the parent in d-dimensions was classified by an integer and was either particle-hole or time-reversal symmetric. Obviously there are two mechanisms to be explained here, the first one is the procedure of dimensional reduction and the second one is the construction of $\mathbb{Z}_2$-classifications in the descendants.

We begin with the reduction scheme. Consider a d-dimensional topological insulator (d does not necessarily need to be even now) described by a Hamiltonian $H_d(k)$, where $k = (k_1, k_2, \ldots, k_d)$ is the momentum vector in d dimensions. In a Dirac representation the latter is given by

$$H_d(k) = \sum_{i=1}^{d} k_i \Gamma^i + m\Gamma^0,$$

where the $(d+1)$-dimensional Dirac Γ-matrices satisfy the usual Clifford algebra $[\Gamma^i, \Gamma^j]_+ = \delta_{ij}\mathbb{1}$. Note that if we would (in a very naive manner) simply replace the mass term m by an additional momentum k_{d+1}, we could end up with a gapless Hamiltonian $H_{d+1}(k)$, which would be $(d+1)$ dimensional. Let us minimally couple $H_d(k)$ to a $U(1)$ gauge field a, i.e. $H_d(k) \to H_d(k+a)$. For the dimensional reduction we apply a Kaluza-Klein compactification to $H_d(k)$, to this end we single out the d-th spatial direction and compactify it to a circle S^1. The system becomes periodic in one direction, while open in the remaining directions. It turns out that k_d is quantised[27] and is a good quantum number. The quantisation is of the form $k_d = 2\pi N_d/r$ where r is the radius of S^1 and $N_d \in \mathbb{Z}$. By sending the radius $r \to 0$, the energies of levels with non-vanishing N_d become very large. For $N_d = 0$ however, the energies remain unchanged. This induces a separation of energy scales which allows us to keep only $N_d = 0$ modes. The minimally coupled Hamiltonian $H_d(k+a)$ then reads

$$H_d(k+a) = \sum_{i=1}^{d} (k_i + a_i)\Gamma^i + m\Gamma^0.$$

---

[26]Following ref. [27] we only consider non-chiral systems for concreteness, i.e. classes AI, D, AII and C.
[27]There are some subtleties involved in this process, which are discussed in ref. [27] and [37].

Upon the identification of $(k_d + a_d) \equiv \Theta$ (remember the d-direction was compactified and a controllable parameter) the Hamiltonian reduces to a $(\bar{d} = d - 1)$-dimensional Dirac Hamiltonian

$$H_{\bar{d}}(\bar{k}, \Theta) = \sum_{i=1}^{\bar{d}} k_i \Gamma^i + \Theta \Gamma^d + m \Gamma^0,$$

where $\bar{k} = (k_1, \ldots, k_{d-1})$. Note that we also removed the field components $(a_{i=1,\ldots,\bar{d}} \equiv 0)$ for clarity. In a way, the procedure consists of three steps: couple the Hamiltonian to an external $U(1)$ gauge field, compactify one direction and replace the corresponding momentum by a parameter. This procedure can of course be iterated, leading to $H_{d-2}((k_1, \ldots, k_{d-2}), \Theta, \phi)$.

(a) **(b)**
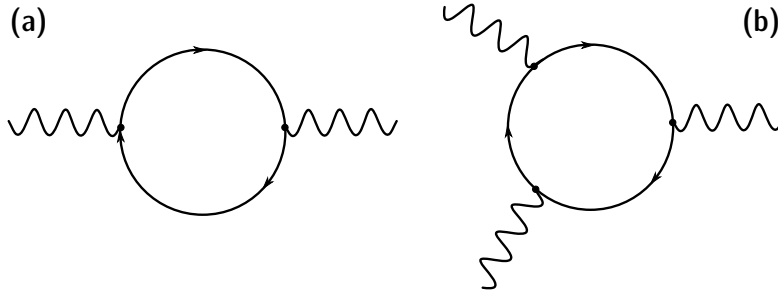
Figure 2.5: Feyman diagrams leading to the Chern-Simons actions in $(2+1)$ dimensions (a) and $(4+1)$ dimensions (b). The external legs correspond to the gauge fields.

The coupling to an external gauge field indicates that a field theoretical description and a (non)-linear response has to be considered. To this end, we recall that the quantum Hall conductivity tensor can be derived as the linear dc response to an external field $a(q)$ coupled to the $(2+1)$-dimensional band insulator[28] [1, 27],

$$\sigma_{ij} = \lim_{\omega \to 0} \frac{i}{\omega} Q_{ij}(\omega + i\delta),$$

$$Q_{ij}(i\nu_m) = \frac{1}{\Omega \beta} \sum_{k,n} \mathrm{tr}\left(J_i(k) G(k, \omega_n + \nu_m) J_j(k) G(k, \omega_n)\right). \tag{2.35}$$

In the upper expression Ω is the area of the system, $J_i(k) = \partial_{k_i} h(k)$ is the dc current (in $i = x, y$ directions) and $G(k, \omega_n) = (i\omega_n - h(k))^{-1}$ is the single-particle Green's function. We are only interested in the non-trivial transverse conductance $\sigma_H = \sigma_{xy}$, which is of course (see sec. 1.4), up to a physical constant (e^2/h), given by the first Chern number [1]. The

---

[28]We now explicitly keep the additional time dimension.

non-vanishing Hall conductance leads to the Hall response,

$$j^\mu = \frac{C_1}{2\pi}\epsilon^{\mu\nu\tau}\partial_\nu a_\tau,$$

where $\mu, \nu, \tau = 0, 1, 2$ are the time and space indices. The response can be derived from the topological Chern-Simons field theory [68]

$$S_{\text{eff}} = \frac{\sigma_H}{2}\int a \wedge \mathrm{d}a = \frac{\sigma_H}{2}\int \mathrm{d}^2x\mathrm{d}t a_\mu\epsilon_{\mu\nu\tau}\partial_\nu a_\tau, \tag{2.36}$$

via

$$j^\mu = \frac{\partial S_{\text{eff}}}{\delta a_\mu}. \tag{2.37}$$

In two dimensions, the coefficient C_1 can be calculated by the Feynman loop integral shown in fig. 2.5a.

Let us now consider $(4+1)$ dimensions, the effective Chern-Simons action is given by

$$S_{\text{eff}} = \frac{C_2}{24\pi^2}\int \mathrm{d}^4x\mathrm{d}t \epsilon^{\mu\nu\rho\sigma\tau}a_\mu\partial_\nu a_\rho\partial_\sigma a_\tau,$$

with the space-time indices $\mu, \nu, \rho, \sigma, \tau = 0, 1, \ldots, 4$, [27]. The coefficient C_2, the second Chern number, has to be calculated from the nonlinear-response[29] one-loop Feynman diagram, shown in fig. 2.5b (see caption for details). The integral yields

$$C_2 = -\frac{\pi^2}{15}\frac{1}{(2\pi)^5}\epsilon^{\mu\nu\rho\sigma\tau}\int \mathrm{d}^4q\mathrm{d}\omega\,\mathrm{tr}\prod_{i=\mu,\nu,\rho,\sigma,\tau}\left(G\partial_{q^i}G^{-1}\right) \tag{2.38}$$

where $q^\mu = (\omega, k_1, k_2, k_3, k_4)$ and again G denotes the single-particle Green's function.

We recall that C_1 represented the winding number of a map $\hat{h}$ from the 2-torus (the Brillouin zone) to the 2-sphere. Analogously, C_2 represents the winding number of the map from the 4-torus to the 4-sphere. We see that the Hall response, as well as the Hall conductivity (two and four dimensional), can be derived from an effective action, via eq. (2.37). The coefficient (the $\frac{d}{2}$-nd Chern number if d is even) can be calculated by a (non)linear-response Feynman diagram. A generalisation to higher even dimensions can be achieved [37].

Now consider a $(4+1)$-dimensional insulator coupled to a $U(1)$ gauge field a. We know that the Hamiltonian, if the fourth coordinate is compactified, and the corresponding momentum $k_4 + a_4$ is identified with an adiabatic parameter Θ, which takes values from 0 to 2π, is reduced to a $(3+1)$-dimensional Hamiltonian. For this lower dimensional version, the effective field

---

[29]Note that for dimensions $d > 2$, nonlinear terms in the derivation of S_{eff} have to be taken into account, resulting in a nonlinear response.

theory can be constructed in the same fashion as for $(4+1)$ dimensions. However, due to the replacement of one momentum by the control parameter Θ, the coefficient C_2 now depends on Θ, as the integration over $k_4 \to \Theta$ in the corresponding Feynman integral (fig. 2.5b) is not performed. If we denote this coefficient by $c_3(\Theta)$ the following sum rule relates it to the *full* Chern number (assuming that the Hamiltonian stays gapped),

$$\int\limits_0^{2\pi} c_3(\Theta)\mathrm{d}\Theta = C_2, \tag{2.39}$$

and is frequently called Chern character. The explicit form of $c_3(\Theta)$ is given by eq. (2.38) without the integral over k_4. The Chern number C_2 represents a winding number, correspondingly c_3 is sometimes related to the magneto-electric polarisation or axion background field [36, 69] $P_3(\Theta)$, by $c_3(\Theta) = \partial_\Theta P_3(\Theta)$. The effective $(3+1)$-dimensional action can then be expressed as [36]

$$S_{3D} = \frac{1}{4\pi}\int \mathrm{d}^3x\mathrm{d}t P_3(x,t)\epsilon^{\mu\nu\rho\tau}\partial_\mu a_\nu\partial_\rho a_\tau.$$

The polarisation is proportional to the flux, $\phi = \oint \mathrm{d}x_4 a_4(x,t,x_4)$, induced by the field component a_4 through the compactified direction x_4. Before we construct the $\mathbb{Z}_2$-invariant in $(3+1)$ dimensions, let us stress that a further reduction to $(2+1)$ dimensions works completely analogously. One compactifies a second direction and then replaces the corresponding coupled momentum by a parameter $(k_3 + a_3) \equiv \phi$. In the two-dimensional effective field theory the coefficient $c_3(\Theta)$ will be replaced by the Chern character $c_4(\Theta,\phi)$, whose explicit form is again given by eq. (2.38) without the integrals over k_3 and k_4. The Chern character integrates to the second Chern number, $\int \mathrm{d}\Theta \mathrm{d}\phi c_4 = C_2$.

To construct a $\mathbb{Z}_2$-classification for time-reversal invariant systems in $(3+1)$ dimensions, we consider its parent $(4+1)$-dimensional time-reversal invariant Hamiltonian $H_4(k)$. Given two Hamiltonians $H_3^1(k)$ and $H_3^2(k)$, one can define a homotopy[30] $h_4(k,\Theta)$ between these Hamiltonians[31],

$$h_4(k,0) = H_3^1(k), \ h_4(k,\pi) = H_3^2(k),$$

which is assumed to be gapped for any Θ. Equally important is the fact that we impose that $h_4(k,\Theta)$ is time-reversal symmetric. Since it is periodic in Θ, we can define the second Chern number $C_2(h_4(k,\Theta))$ of h_4. For any two homotopies $h_4^1(k,\Theta)$ and $h_4^2(k,\Theta)$, the resulting

---

[30] Apart from the fact that such an interpolation is not always trivial to find, there is again a slight subtlety in proving the existence of such an interpolation. However, we do not care about such details at this point and refer to ref. [27] for a more detailed discussion.

[31] We denote Hamiltonians here by a capital H with the subscript indicating its (spatial) dimension. Homotopies are denoted by a lower case h, where the subscripts indicates the (spatial) dimension after replacing the free parameter by an additional coordinate, e.g. $h_4(k,\Theta \to k_4) \to H_4(k)$.

Chern numbers $C_2(h_4^i(k, \Theta))$ in general differ. However, it turns out (see e.g. ref. [36, 37] for proofs), that time-reversal symmetry confines the difference between two such Chern numbers to be even. Consequently, one defines the relative Chern parity $(-1)^{C_2(h_4(k,\Theta))}$ for two $(3+1)$-dimensional Hamiltonians $H_3^{i=1,2}(k)$. We choose $H_3^2(k)$ to be the trivial vacuum Hamiltonian. If the Hamiltonian $H_3^1(k)$ can continuously be transformed to the vacuum, it follows that the corresponding relative Chern parity is $(-1)^{C_2(h_4(k,\Theta))} = +1$. If however, such a deformation is not possible without turning gapless, the latter yields $(-1)^{C_2(h_4(k,\Theta))} = -1$. In this way, a $\mathbb{Z}_2$-classification is constructed in $(3+1)$-dimensions[32].

A $\mathbb{Z}_2$-classification in the further reduced $(2+1)$-dimensional systems, is constructed in the same way, since the relative Chern parity in $(3+1)$ dimensions is independent on the choice of interpolation. Consider a homotopy $h_3(k, \Theta)$ such that

$$h_3(k, 0) = H_2^1(k), \quad h_3(k, \pi) = H_2^2(k),$$

for two $(2+1)$-dimensional Hamiltonians. Following the arguments from above, we can define a $\mathbb{Z}_2$ invariant for $h_3(k, \Theta)$. A second time-reversal invariant homotopy $h_4(k, \Theta, \phi)$ can be constructed, such that

$$h_4(k, \Theta, 0) = h_3^1(k, \Theta), \quad h_4(k, \Theta, \pi) = h_3^2(k, \Theta)$$

and

$$h_3(k, 0, \phi) = H_2^1(k), \quad h_3(k, \pi, \phi) = H_2^2(k),$$

where h_3^1 and h_3^2 are two different interpolations. For $h_4(k, \Theta, \phi)$ one is in a position to define the second Chern number $C_2(h_4(k, \Theta, \phi))$ and accordingly a parity $(-1)^{C_2(h_4(k,\Theta,\phi))}$. It can be proven, that the latter is always positive and that the parity for the $(2+1)$-dimensional system is nothing but the relative Chern parity for $h_3(k, \theta)$.

Note that the above strategy is not tied to the dimensional sequence $(4+1) \to (3+1) \to (2+1)$, nor is it tied to time-reversal symmetry. In fact for the symmetry classes under inspection, the construction for the sequence $(2+1) \to (1+1) \to (0+1)$, is based on the same arguments as above but with particle-hole symmetry instead of time-reversal symmetry.

As an example, we consider class D in $(2+1)$ dimensions with a Dirac Hamiltonian given by eq. (1.10). Due to the particle-hole symmetry (represented by σ_1) the gapped Hamiltonian is given by $H(k) = m\sigma_3$. The requirement of an insulator leaves us with two choices, $m > 0$ or $m < 0$. Now consider two Hamiltonians $H^1(k)$ and $H^2(k)$ with two masses m^1 and m^2, respectively. The interpolation $H(k, \Theta)$ between these two Hamiltonians will define a map $\hat{h}(k, \Theta)$ from the torus to the sphere. We fix $m^1 > 0$ and the vector $\hat{h}(k, 0)$ will point to the north-pole. If m^2 has the same sign as m^1, the vector will evolve under $\hat{h}(k, \Theta)$ and

---

[32]Equivalently, using eq. (2.39) one finds that $P_3 = 0$ indicates a topologically trivial system, while for $P_3 = \frac{1}{2}$ the system is non-trivial.

eventually end up at the north-pole. If on the other hand, the signs differ, the vector will end up at the south-pole. This two inequivalent trajectories can be used to define a Z_2 (cf. our discussion in section 3.2.2).
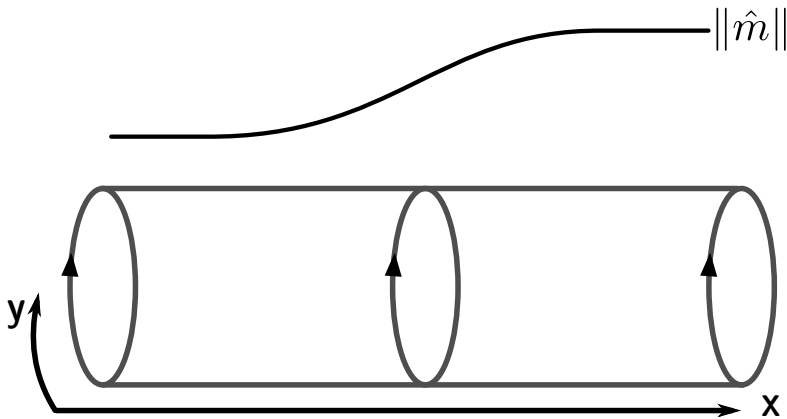

Figure 2.6: Schematic construction of the two-dimensional $\mathcal{Q}$ matrix. While the x coordinate is open, periodic boundary conditions are imposed on y. The system parameters, encoded in the mass term $\hat{m}$, are changing only as a function of x.

2.5.2 Topological invariants in two dimensions

For the Chern insulators (class A, D and C) in two dimensions, the coefficient in the Chern-Simons action (2.36) is given by the Chern number. Our strategy is based on a representation of these coefficients in terms of the quasiclassical Eilenberger functions. We will focus on class A, since the technique can straightforwardly applied to the remaining two $\mathbb{Z}$-topological classes.

We consider the two-dimensional massive Dirac Hamiltonian of class A,

$$H = -iv(\partial_x \sigma_x + \partial_y \sigma_y) + m\sigma_z.$$

In order to construct the two-dimensional Eilenberger function, we assume periodic boundary conditions in the y-direction. The system parameters are however assumed to vary in x-direction only. This assumption is justified in a thin cylindrical geometry. In fig. 2.6 we illustrate the procedure. Due to the periodic boundary conditions, the four-point Green's function $G(x, x', y - y', \epsilon)$ depends only on the difference of $y - y'$, and we can define the two-dimensional Eilenberger function in a mixed representation

$$\mathcal{Q}_\epsilon(x, k_y) = \lim_{x \to x'} 2i \left[vG(x, x', k_y; \epsilon)\sigma_x - \text{sgn}(x - x') \right]. \tag{2.40}$$

In class A, the transverse Hall conductance can be derived as the linear response of the

system to an external field a. The current kernel is given by the one-loop Feynman integral fig. 2.5a. Note that the Kubo formula (2.35) depends on the full Green's function and due to the current operators taken at different spatial points, a direct substitution of the latter by $\mathcal{Q}$ is not possible. However, using that the evolution of G is determined by a set of linear differential equations similar to eq. (2.7), the Green's function can be reconstructed from $\mathcal{Q}$ using

$$G(x, x', k_y; \epsilon) = -\frac{i}{2v} \left[\mathcal{Q}_\epsilon(x, k_y)\sigma_x + \sigma_x \operatorname{sgn}(x - x') \right] e^{-\mathcal{L}|x-x'|}. \qquad (2.41)$$

Since the Hamiltonian is linear, the current operators are given by $J_i = v\sigma_i$ and the Hall conductance reads

$$\sigma_{xy} = \lim_{\omega \to 0} \frac{i}{2\pi\omega\Omega} \operatorname{tr} \int \mathrm{d}x \mathrm{d}k_y \mathrm{d}x' \sum_n \left(v^2 \sigma_x G_{\epsilon_n - \omega_n/2}(x, k_y)\sigma_y G_{\epsilon_n}(-x, -k_y) \right).$$

With the identification (2.41) we see, that the above integral in general contains four terms. However, terms that are odd functions in x and terms which are proportional to σ_z, will not contribute due to the integration and the trace, respectively. Defining[33] $\mathcal{Q}_\pm \equiv \mathcal{Q}_{\epsilon_n \pm \omega_n/2}(\pm x, \pm k_y)$ and $\mathcal{L}_\pm$ correspondingly, we find

$$\sigma_{xy} = \operatorname{tr}_y \frac{-i}{8\pi\Omega\omega} \int \mathrm{d}x \mathrm{d}x' \left(\sigma_x \mathcal{Q}_+ e^{-\mathcal{L}_+|x-x'|}\sigma_x \sigma_y \mathcal{Q}_- e^{-\mathcal{L}_-|x-x'|}\sigma_x \right),$$

where the trace tr_y now contains the frequency limit, the integration over k_y as well as the energy summation. As usual we choose $\mathcal{L}$ to be diagonalised as $\mathcal{L}_\pm = T_\pm \operatorname{diag}(\lambda_\pm^1, \lambda_\pm^2) \otimes \sigma_z T_\pm^{-1}$. Since the real parts of the eigenvalues $\lambda_\pm^{1,2}$ are again chosen to be real, it follows that

$$\sigma_{xy} = \lim_{\omega \to 0} \frac{1}{2\pi\omega} \int \mathrm{d}k_y \mathrm{d}\bar{x} \sum_{n,\alpha,\beta} \int_0^\infty \left(e^{-\lambda_+^\alpha \bar{x}} P_{\alpha\beta} N_{\beta\alpha} \right)$$

$$= \lim_{\omega \to 0} \frac{1}{2\pi\omega} \int \mathrm{d}k_y \sum_{n,\alpha,\beta} \left(\frac{1}{\lambda_+^\alpha + \lambda_-^\beta} P_{\alpha\beta} N_{\beta\alpha} \right),$$

where we introduced the relative coordinate $\bar{x} \equiv x - x'$ and the matrices $P \equiv T_+^{-1}\sigma_z \mathcal{Q}_- T_-$, $N = T_-^{-1}\mathcal{Q}_+ T_+$. The indices $\alpha, \beta = 1, 2$ refer to the particle-hole structure of the eigenval-

---

[33]Note that subscript refers to the energy arguments not to the terminals.

ues, and in case of Dirac Hamiltonians[34] we arrive at the following expression

$$\sigma_{xy} = \lim_{\omega \to 0} \frac{1}{2\pi\omega} \int \mathrm{d}k_y \sum_n \frac{1}{\lambda_+ + \lambda_-} \operatorname{tr} P \cdot N.$$

In appendix B we show that the remaining trace in the above expression leads to the final result,

$$\sigma_{xy} = \frac{1}{(4\pi)^2} \int \mathrm{d}\epsilon \mathrm{d}k_y \operatorname{tr}(\partial_{k_y}\mathcal{Q})\mathcal{Q}(\partial_\epsilon \mathcal{Q}). \tag{2.42}$$

Equation (2.42) gives the Hall conductance in terms of the quasiclassical Eilenberger function defined in eq. (2.40). We can readily give the evolution operator and the $\mathcal{Q}$-matrix

$$\mathcal{L}_\epsilon = -i\sigma_x \epsilon + iv\partial_y \sigma_z + m\sigma_y,$$
$$\mathcal{Q}_\epsilon = \frac{-v\sigma_z k_y + m\sigma_y - i\sigma_x \epsilon}{\sqrt{v^2 k_y^2 + m^2 - \epsilon^2}}.$$

The Hall conductance is then given by

$$\sigma_{xy} = -2m \lim_{\omega \to 0} \frac{1}{2\pi\omega} \int \mathrm{d}k_y \sum_n \omega \frac{\lambda_+^{-1}\lambda_-^{-1}}{\lambda_+ + \lambda_-} = m \int \mathrm{d}k_y \int \mathrm{d}\epsilon \lambda^{-3}.$$

With eigenvalue $\lambda = \sqrt{m^2 + k_y^2 v^2 - \epsilon^2}$, we find (in units $e = \hbar = 1$)

$$\sigma_{xy} = \frac{1}{4\pi} \frac{m}{|m|}.$$

Note that in the final result an additional factor $\frac{1}{2}$ appears due to the Dirac description. We took into account that in the limit of zero temperature, a Wick rotation leads to the replacement of $\epsilon \to i\epsilon$. The responses of class D and C can be calculated in the fashion.

Classes DIII and AII however, are $\mathbb{Z}_2$-topological insulators and thus the Chern number vanishes. We use class AII to demonstrate that the Chern character in $(2+1)$ dimensions can be derived from the $(4+1)$-dimensional Chern-Simons action, expressed in terms of the Eilenberger $\mathcal{Q}$-function. A $\mathbb{Z}_2$-invariant (the Chern parity) can then be constructed following the analysis presented in the previous section.

---

[34]For Dirac Hamiltonians the indices α, β are actually redundant since the eigenvalues come in pairs (± 1), their presence in the upper expression is thus merely for the sake of completeness.

The four-dimensional Dirac Hamiltonian is given by

$$\mathcal{H} = -iv \sum_{i=1}^{4} \Gamma_i \partial_i + \Gamma_0 \hat{m},$$

where we have chosen a representation in which $\Gamma_0 = \sigma_3$, $\Gamma_{i=1,2,3} = \sigma_1 \otimes \sigma_i$ and $\Gamma_4 = \sigma_2$. It follows that $\mathcal{H} = U_{\mathrm{T}}^{\dagger} \mathcal{H}^T U_{\mathrm{T}}$ with $U_{\mathrm{T}} = \sigma_0 \otimes \sigma_2$ and $U_{\mathrm{T}} U_{\mathrm{T}}^* = -\mathbb{1}$, which confirms the systems membership in class AII.

We will closely follow the lines of ref. [27] (as outlined in the previous section) and make use of the dimensional reduction to construct the Chern character in $(2+1)$ dimensions. To this end, we note that the very construction of our higher-dimensional $\mathcal{Q}$-matrix facilitates the procedure of compactification. We minimally couple the Hamiltonian to an external field a and replace the momentum operators $k_3 \to k_3 + a_3 \equiv \Theta$ and $k_4 \to k_4 + a_4 \equiv \Phi$, by two controllable parameters Θ and Φ, respectively. The object c_2 describes the non-linear response given by eq. (2.38) without the integrals over k_3 and k_4. In analogy to the Kubo formula, we therefore consider the object

$$\frac{c_2}{2\pi} = \lim_{q_2, \omega_3 \to 0} \frac{G_2^x}{q_2 \omega_3}, \tag{2.43}$$

where G_2^{μ} is given by the Feynman diagram in fig. 2.7. G_2^{μ} is obtained from a three point current correlation function

$$G_2^{\mu} = \frac{1}{(2\pi)^2} \int \mathrm{d}k_y \mathrm{d}\epsilon \mathrm{d}x \, \mathrm{tr} \Big(G(x_1 - x_3, k_y, \epsilon) J_A^{\mu} G(x_2 - x_1, k_y - q_2 - q_3, \epsilon - \omega_2 - \omega_3) J_{\Theta}$$

$$\times \, G(x_3 - x_2, k_y + q_2 + q_1, \epsilon - \omega_3) J_{\Phi} \Big), \tag{2.44}$$

where $J_a^{\mu} = \partial\mathcal{H}/\partial a_{\mu} = \Gamma_{\mu}$ and the Green's function is defined as in eq. (2.41) with σ_x replaced by Γ_1.

Similar to the $(2+1)$-dimensional case, only one contribution in eq. (2.44) survives the integral and trace. Following the same steps as in $(2+1)$ dimensions, setting $x_1 = 0$, $q_1 = -(q_2 + q_3)$ (and ω_1 accordingly) after some algebra we arrive at

$$G_2^x \sim \int \mathrm{d}\epsilon \mathrm{d}k_y \left(\frac{\sum_{i=1}^{3} \lambda_i}{(\lambda_1 + \lambda_2)(\lambda_1 + \lambda_3)(\lambda_2 + \lambda_3)\lambda_1\lambda_2\lambda_3} \right) \mathrm{tr}(P \cdot N \cdot V), \tag{2.45}$$

where we defined the matrices

$$P \equiv T_3^{-1} \Gamma_1 \Gamma_4 \mathcal{Q}_{\epsilon}(k_y) T_1,$$

$$N \equiv T_1^{-1} \mathcal{Q}_{\epsilon - \omega_2 - \omega_3}(k_y - q_2 - q_3) T_2,$$

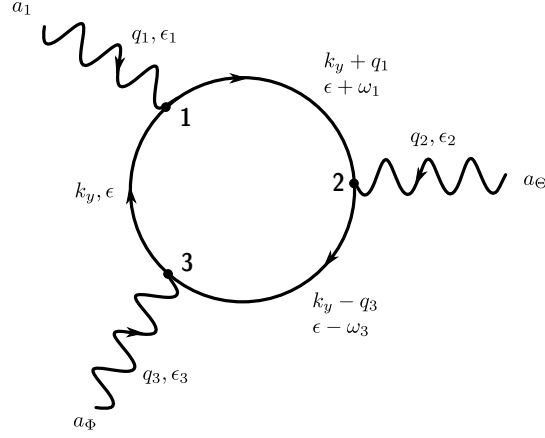$$V \equiv T_2^{-1} \Gamma_1 \Gamma_3 \mathcal{Q}_{\epsilon - \omega_3} T_3,$$

Figure 2.7: Feynman diagram of a three-point current correlation function, leading to the Chern-Simons action in $(4+1)$ dimensions.

and the constant c is determined later. Here the index $i = 1, 2, 3$ refers to the Green's functions (and corresponding operators $\mathcal{Q}$ and $\mathcal{L}$) $G(x_1 - x_3, k_y, \epsilon), G(x_2 - x_1, k_y - q_2 - q_3, \epsilon - \omega_2 - \omega_3)$ and $G(x_3 - x_2, k_y + q_2 + q_1, \epsilon - \omega_3)$, respectively. The trace $\mathrm{tr}(P \cdot N \cdot V)$ is calculated in appendix B and the final expression reads

$$c_2(\Theta, \Phi) = \frac{3}{32\pi} \int \mathrm{d}k_y \mathrm{d}\epsilon \, \mathrm{tr}(\partial_\Phi \mathcal{Q}) \mathcal{Q}(\partial_\omega \mathcal{Q})(\partial_\Theta \mathcal{Q})(\partial_{k_y} \mathcal{Q}). \qquad (2.46)$$

We have thus shown that the Chern character can be expressed in terms of the quasiclassical Eilenberger functions. Note that opposed to the Chern number this object still depends on two parameters Φ and Θ. It is easily checked that $\mathrm{tr}(P \cdot N \cdot V) \propto (\lambda_1 \lambda_2 \lambda_3)^{-1}$, and consequently the second Chern number is then obtained by integrating over the both parameters,

$$C_2 = \frac{1}{2\pi} \int \mathrm{d}\Phi \mathrm{d}\Theta c_2(\Theta, \Phi) = \frac{3}{8\pi^2} \int \mathrm{d}k_y \mathrm{d}\epsilon \mathrm{d}\Phi \mathrm{d}\Theta \frac{m}{\lambda^5}$$

$$= \frac{3}{8\pi^2} \int \mathrm{d}k_y \mathrm{d}\epsilon \mathrm{d}\Phi \mathrm{d}\Theta \frac{m}{\sqrt{m^2 + \Theta^2 + \Phi^2 + \epsilon^2 + m^2}^5} = \frac{1}{2} \frac{m}{|m|}.$$

As we have already discussed in the previous section, G_1^x can be used to construct a $\mathbb{Z}_2$-invariant in $(2+1)$-dimensions. In class DIII this invariant can be derived starting from a $(3+1)$-dimensional Hamiltonian and reducing it to $(2+1)$-dimensions, leads to a similar expression of the form $G_1^x \sim \int \mathrm{d}k_y \mathrm{d}\epsilon \, \mathrm{tr}(\partial_\Phi \mathcal{Q}) \mathcal{Q}(\partial_\omega \mathcal{Q})(\partial_{k_y} \mathcal{Q})$, which integrates to C_2. After an analytic continuation of the energy, the quasiclassical $\mathcal{Q}$-function becomes an element of the Grassmannian $U(2)/U(1) \times U(1) \simeq S^2$ in $(2+1)$ dimensions and $O(4)/O(2) \times O(2)$ in $(4+1)$ dimension, respectively. Following our discussion in sec. 1.3, we find that σ_{xy} and C_2 represent the winding number of a map from the two- or four-sphere to a Grassmannian.

This concludes our extension of the quasiclassical approach to two-dimensional topological insulators.

2.6 Summary

We provided a quasiclassical approach to one- and two-dimensional topological insulators and superconductors. Modelling the one-dimensional systems by a disordered quantum wire connected to two topological insulator (or superconductor) terminals, we provided topological invariants for all five non-trivial symmetry classes. It turned out, that the transfer matrices incorporating electron scattering at disorder in the scattering region, play no role in the construction of these invariants. The latter solely depend on the Eilenberger functions of the terminals. These Eilenberger functions can be analytically constructed in the clean limit for isotropic system parameters. The topological invariants give the number of edge modes present. A detailed proof of this relation is given in appendix B. In two-dimensional systems, we were able to show that a $\mathcal{Q}$-matrix can be constructed in a mixed Wigner-like representation, by imposing periodic boundary conditions on one coordinate. It was then proven that the Chern-Simons characters appearing in the corresponding topological field theory of the topological insulator (or superconductor) can be expressed in terms of the two-dimensional Eilenberger function. Which in return can be used to construct invariants in two dimensions.

Part II

Majorana Fermions in disordered quantum wires

3

Topological superconductors and Majorana fermions in condensed matter systems

Topological superconductors provide the possibility to create a very elusive kind of particles at their edges, the so-called Majorana particles. These topological excitations constitute their own anti-particles and are interesting for both fundamental aspects as well as practical reasons. Thanks to their unconventional exchange statistics and topological protection, they have become one of the most promising candidates for quantum computing. Although originating from a very simple tight-binding model, these states have proven to be very hard to realise experimentally. In this section, we review the role of Majorana particles in condensed matter physics. We discuss the nature of these elusive particles and their theoretical prediction in spinless p-wave superconductors due to Kitaev [9]. Superconductor-semiconductor sandwich geometries, in particular one-dimensional quantum wires, are discussed both from a theoretical as well as experimental point of view. We show how Majorana particles emerge in these systems and what difficulties experimentalists face. In anticipation of the next chapter, we restrict our discussion to (quasi) one-dimensional systems and closely follow the lines of [70, 71].

3.1 Topological superconductors

Topological superconductors are the natural extensions of topological insulators to superconducting systems. On a mean-field level, superconductors are described by a Bogoliubov-de Gennes (BdG) Hamiltonian. The fermionic quasi-particle spectrum of the BdG-Hamiltonian shows a superconducting energy gap, set by the pairing potential Δ. Superconducting systems come with an intrinsic particle-hole symmetry which relates states at opposite energies.

Possible end states of a one-dimensional superconductor are represented by a conjugated pair of states within the gap, with energies $\pm\epsilon$. Formally the creation, $c_\epsilon^\dagger$ and annihilation operators c_ϵ for a quasi-particle state are related by $c_\epsilon^\dagger = c_{-\epsilon}$. The latter property allows to draw an interesting analogy to the concept of bulk-boundary correspondence introduced in the first part of this work. Figure 3.1 shows the spectrum of end states in a one-dimensional topological superconductor for spinless fermions. For finite energy, these states are symmetrically distributed. These end states are topologically trivial and not protected by topology since they can simply be removed by absorbing them into the bulk of states with $\epsilon > |\Delta|$, without closing the superconducting gap. For zero-energy, where the particles localise at vortices or edges, the quasi-particle operator becomes hermitian $c_0^\dagger = c_0$. Since the state lacks a partner, it cannot be absorbed and thus the state is topologically protected by particle-hole symmetry. As a consequence, these states are immune to local perturbations that do not close the energy gap and can only be removed by a topological quantum phase transition (which in return is characterised by a gap closing). The presence or absence of such a zero-energy state defines a topological $\mathbb{Z}_2$ invariant. Edge-states with hermitian creation operators, called Majorana modes, and their possible realisations in one-dimensional systems, will be the main object of interest for the remainder of this work. Although we focus on one-dimensional systems henceforth, the analogy between topological superconductors and insulators can be illustrated considering the IQHE and QSHE introduced in chapter 1. We recall that the IQHE arose in systems of class A with no symmetries present, while the QSHE was present in class AII with unbroken time-reversal symmetry ($T^2 = -1$). The former was classified by an integer invariant while the latter was a $\mathbb{Z}_2$ topological insulator. Class D can be *constructed* from class A by introducing an unbroken particle-hole symmetry ($C^2 = +1$), and indeed topological insulators in class D in two dimensions are also classified by an integer invariant. The chiral edge modes in class A have their counterparts, chiral Majorana edge modes, in class D. The latter can be found at edges of spinless $p_x + ip_y$ superconductors [72]. The superconducting counterpart of class AII is class DIII ($C^2 = -1$), which is a $\mathbb{Z}_2$-topological superconductor in two dimensions. The time-reversal symmetry protected edge modes are counter-propagating helical Majorana modes. Further analogies are discussed in [73]. We now focus on one-dimensional topological superconductors hosting Majorana states at their ends.

3.2 Majorana Fermions in condensed matter systems

In recent years the notion of Majorana particles saw a huge uprising in the condensed matter community. Originated from a work in high-energy physics by Ettore Majorana [10] in 1937, the presence of particles being their own anti-particles was predicted. Majorana realised a representation in which the generally complex Dirac equation, describing a relativistic spin-$\frac{1}{2}$ fermion, possesses a real solution. This solution describes fermions that are eigenstates to the charge-conjugation operator and therefore are their own anti-articles. While such a property
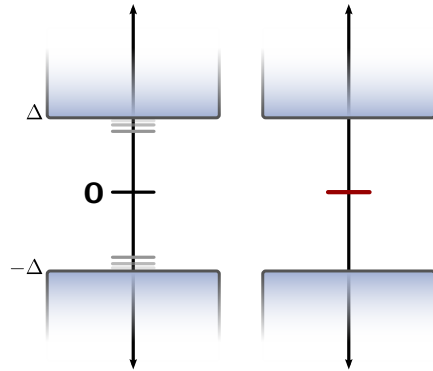
Figure 3.1: Edge states spectrum of one-dimensional topological insulator. Shaded blue re-
gions indicate bulk of states. Left: In the trivial phase two states of opposite
energy (dark grey lines) are present. Both can be absorbed and removed from
the gap (indicated by light grey lines) . Right: In the non-trivial phase there is a
single unpaired state (red). This state cannot be removed and the corresponding
quasi-particle operator is hermitian.

is nothing special for bosons, it is for fermions. Majorana even went so far to claim that
neutrinos belong to this illustrious kind of particles, a claim that has yet to be clarified. While
the high-energy community still cherishes a hope that Majorana particles can be discovered
in their experiments, condensed matter physicists started their own journey for these exotic
states [69–72, 74]. The motivation is twofold: Firstly, and this also holds for the high-energy
colleges, Majorana particles by themselves are interesting from a fundamental point of view.
Secondly, Majorana particles are tailor-made for quantum computational applications.

In addition to the obvious discrepancy in energies/temperatures, Majorana particles in
high-energy physics describe fundamental particles, which is different in condensed matter
systems[1]. It is obvious that excitations like electrons or holes cannot represent Majorana
fermions since they carry a charge, and are therefore described by two physically distinct
operators. So if $c_\sigma^\dagger$ is the creation operator for an electron with spin σ and c_σ for a hole with
spin σ, the operators are distinct and therefore not their own anti-particles. Only non-trivial
excitations, such as composites/superpositions can (if at all) be responsible for the presence
of Majorana particles in condensed matter systems. It stands to reason that superconduct-
ing systems are tailor-made candidates, since the underlying excitations are superpositions of
electron and hole excitations. However, the common s-wave superconductors do not answer
the purpose since the appearing quasi-particle operators are of the form $d = u_1 c_\uparrow^\dagger + u_2 c_\downarrow$, [70].
Due to the spin, this state is physically distinct from its conjugate $d^\dagger = u_2^* c_\downarrow^\dagger + u_1^* c_\uparrow$. In
fact, the spin prevents hermiticity for the quasi-particle operator as charge does for the elec-

---

[1]We point out that Majorana fermions in high-energy physics, opposite to their condensed matter quasi-
particle representatives, can be massive and spinfull and obey usual Fermi statistics.

trons. One therefore has to consider non-trivial excitations, e.g. spinless superconductors. In such systems, the spin components are equivalent and allow for the construction of creation operators $\gamma = uc_\sigma^\dagger + u^* c_\sigma$, which are hermitian (i.e. $\gamma = \gamma^\dagger$) or equivalently, their own anti-particle. Due to the Pauli principle, the order parameter $\Delta(k) \propto \langle c_\sigma(k) c_\sigma^\dagger(-k) \rangle$ has to be an odd function in momentum. The latter is often called *odd parity pairing* and can be found in p-wave superconductors in one dimension and in $p + ip$ superconductors in two dimensions [75]. Realisations of such excitations are expected to occur in the $\nu = \frac{5}{2}$ fractional quantum Hall state, and p-wave superconductivity. Although predicted for the ground state of Sr_2RuO_4 [76, 77], p-wave superconductivity [78] has yet to be discovered experimentally. However, as we will see later, due to the topological nature of Majorana fermions, experimentally more accessible models were proposed, sharing the topological properties without relying on the presence of p-wave superconducting materials. Before we discuss the details of Majorana fermions in p-wave superconductors, we shall comment on their possible use in quantum information theory[2].

3.2.1 Non-abelian statistics and quantum computing

One of main reasons for the great interests in Majorana fermions in condensed matter physics, is their possible application to quantum computing [11]. The latter is related to the exchange statistics of these particles and although we abandon the idea of giving any fruitful insight into the topic of quantum computing, we will elaborate a bit on the statistics. By construction, Majorana particles are their own anti-particles and therefore described by an hermitian creation (annihilation) operator $\gamma = \gamma^\dagger$. However, we cannot assign an occupation number to it since a real fermionic state f is constructed by a pair of Majorana states $\gamma_{1,2}$, i.e. $f = \frac{1}{2}(\gamma_1 + i\gamma_2)$. This construction suggests the interpretation of γ_1 as the real and γ_2 as the imaginary part of a fermion f. Such a construction sounds rather academic, since due to the overlap of both states, a discrimination between the two Majorana states is impossible. Nevertheless, the construction above allows for superpositions of two spatially separated Majorana states and as a consequence, f is a highly non-local object. Since local perturbations can only affect one of the two Majorana fermions, these non-local objects are protected from almost all types of decoherence. This property by itself makes it very interesting for quantum computation applications but would be useless without a proper way to manipulate states, i.e. to perform quantum gate operations. This is where the non-abelian exchange statistics of Majorana states come to play. Exchange statistics characterise the effect of exchanging two indistinguishable particles. Upon such an exchange, fermions and bosons acquire a factor $+1$ or -1, respectively, while for abelian anyons the wave functions pick up a phase factor $e^{i\theta}$ (which interpolates between $+1$ and -1). For non-abelian anyons however, the story is more-interesting in that the states can be fundamentally different quantum states after exchanging/braiding them. One may now naively argue that in one dimension, exchange

---

[2]A claim that has been exploited by the community to attract the attention of various referees and editors. Shamefully, we do not bother to resist and jump on the bandwagon ourselves.

statistics of particles are not relevant since there is no way for the particles to avoid each other. But in arranging one-dimensional superconductors in networks, one is in a position to exchange Majorana states bound to the ends of the latter, again leading to non-abelian statistics. It is thus evident that even if possible Majorana fermion suspects are experimentally identified, probing this non-trivial behaviour will winnow truth from falsehood. A possibility to probe non-abelian statistics is therefore much desired and is an active field of research. We refer to ref. [79, 80] for further reading.

3.2.2 Majorana states in spinless p-wave superconductors

The simplest model of a one-dimensional spinless p-wave superconductor hosting Majorana states was introduced by Kitaev [9]. The tight-binding Hamiltonian introduced, describes spinless fermions hopping on a chain with N-sites, exposed to long-range-ordered p-wave superconductivity. If we denote the annihilation operator by c_x and the associated number operator by $n_x = c_x^\dagger c_x$, the Hamiltonian reads

$$H = -\mu \sum_x n_x - \frac{1}{2} \sum_x \left(t c_x^\dagger c_{x+1} + \Delta e^{i\phi} c_x c_{x+1} + \text{h.c.} \right), \tag{3.1}$$

where the chemical potential μ, the nearest-neighbour hopping t and the pairing amplitude Δ are considered to be homogeneous (note that we introduced a superconducting phase ϕ). Kitaev showed that upon splitting each fermion into a pair of Majorana fermions, the system exhibits two phases, of which one hosts two unpaired Majorana fermions at the end of the chain. Before we turn to a Majorana fermion description and investigate the edges of the chain, it is illusive to understand the two different phases by investigating the bulk first. To this end we impose periodic boundary conditions on the system. The momentum-space representation of eq. (3.1) reads

$$H = \sum_k E(k) \tilde{c}_k^\dagger \tilde{c}_k,$$

where the sum runs over the whole Brillouin zone, and $\tilde{c}_k = u_k c_k + v_k c_{-k}^\dagger$. The precise form of the eigenstates u_k and v_k are of no interest at this point, contrary to the bulk energies

$$E(k) = \sqrt{(-t \cos k - \mu)^2 + (\Delta \sin k)^2}.$$

One recognises the opening of a gap in the spectrum due to the pairing amplitude. The odd pairing amplitude $\Delta_k = \Delta \sin(k)$ of a p-wave superconductor and the Pauli principle ensure that the system has to be gapless at isolated points. Indeed for $k = 0$ and $k = \pm \pi$ we see that these isolated points[3] are reached at $\mu = \pm t$. It is therefore evident, that one

---

[3] Since the Pauli principle excludes Cooper pairs at isolated points, they can be added to the Hamiltonian with energy zero, which would correspond to a gap closure in the bulk energy.

has to distinguish between the cases $\mu < -t$ and $|\mu| < t$ (since particle-hole symmetry is present). Note however, that at this point it is by no means clear whether these regimes actually describe different phases. The argument for the latter is of topological nature and will be discussed later. Nevertheless, one easily recognises that both regimes behave physically different. For $|\mu| < t$, there exists a filled band that is gapped because of the p-wave nature of the system, whereas the case of $\mu < -t$ is homotopic to the vacuum[4] and can therefore be considered as trivial. This rather basic arguments hint at the presence of two distinct phases, for a more quantitative discussion we refer to ref. [72].

Let us return to the discussion of Majorana states and relax our periodic boundary conditions. In fact, at least for the phase $\mu < -t$, which we identified to be trivial, it is clear that the results should be invariant as we expect no Majorana states at the boundaries. The idea of Kitaev [9] was to represent each spinless fermion in the chain, described by eq. (3.1), by a superposition of two Majorana fermions $\gamma_{x,i=1,2}$. Formally each fermion operator c_x is decomposed into its real and imaginary part. The Majorana operators are then given by

$$\gamma_{x,1} = c_x^\dagger + c_x,$$
$$\gamma_{x,2} = i(c_x^\dagger - c_x), \tag{3.2}$$

where the index $i = 1, 2$ now labels the two Majorana states that form the fermion at site x. Note that for simplicity we set the superconducting phase to $\phi = 0$. These operators are indeed hermitian $\gamma_{x,i} = \gamma_{x,i}^\dagger$ and obey the fermion anti-commutation relations, $[\gamma_{x,i}, \gamma_{y,j}]_+ = 2\delta_{ij}\delta_{xy}$. The representation of H in terms of the Majorana fermions is straightforward, yet in order to understand the manifestations of Majorana states and the distinction between the two phases, we only consider two special cases of parameter configurations in which the discussion becomes particularly simple.

By choosing $\mu < 0$ and $\Delta = t = 0$ we define a state within what we identified to be the trivial phase. The Hamiltonian in this case is given by

$$H = -\frac{\mu}{2} \sum_{x=1}^{N} (1 + i\gamma_{x,2}\gamma_{x,1}),$$

and contains only couplings between Majorana states $\gamma_{x,2}$ and $\gamma_{x,1}$ at the same site of the chain. Despite the fact that this is merely a rewriting of the Hamiltonian for periodic boundary conditions, we recognise two things: First, the ground state is unique and is given by the vacuum as discussed earlier. Second, adding a fermion to the chain comes with the energy cost of $|\mu|$ and thus the system exhibits a gap. An illustration of the setup is shown in the upper part of fig. 3.2. As a second limiting case, we choose $\mu = 0$ and $t = \Delta \neq 0$
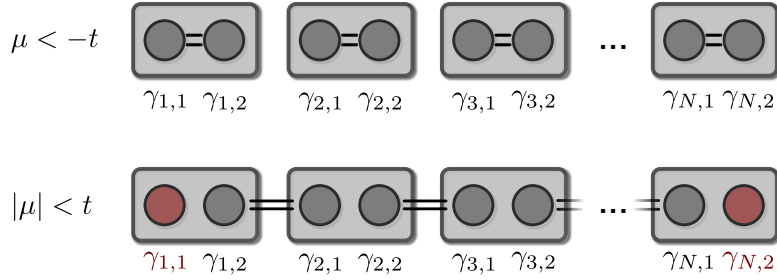
---

[4]Consider the limit $\mu \to -\infty$.

Figure 3.2: Two phases of the Kitaev model. Boxes symbolise fermions while the circles indicate Majorana fermions that constitute the latter. Top: In the trivial phase $\mu < -t$ all Majorana partners are paired (indicated by the double lines) within the fermions at the same site and no free Majorana particle is present. Bottom: In the non-trivial phase $|\mu| < t$, the pairing is between Majorana partners at different sites, leaving two unpaired (red) Majoranas at the end of the chain.

arbitrary, which puts the chain in the non-trivial phase and leads to the Hamiltonian

$$H = -i\frac{t}{2} \sum_{x=1}^{N-1} \gamma_{x,2}\gamma_{x+1,1}.$$

We illustrated the situation in lower part of fig. 3.2 and, opposite to the previous discussion, we see that the coupling is introduced between Majorana states of adjacent sites. For convenience one introduces the corresponding fermion operator $d_x = \frac{1}{2}(\gamma_{x+1,1} + i\gamma_{x,2})$ and the Hamiltonian in this basis reads

$$H = t \sum_{x=1}^{N-1} \left(d_x^\dagger d_x - \frac{1}{2} \right).$$

Which clearly signalises the presence of a gap. The crucial difference lies in the ground state of this representation, which is now two-fold degenerate. Since both end points of the chain, $\gamma_{1,1}$ and $\gamma_{N,2}$, are missing from the Hamiltonian, they can form a fermion $f = \frac{1}{2}(\gamma_{1,1}+i\gamma_{N,2})$, which can be added with zero-energy cost. The system therefore hosts zero-energy Majorana states localised at the end of the chain. The end of the chain is connected to the vacuum, which as we have discussed earlier, is a limiting case of the $\mu < -t$ phase. One thus concludes, that these edge states appear at the border of the trivial and non-trivial phase. The origin of this effect is of topological nature since one is not able to smoothly interpolate between both phases without closing the gap. And since it is topological, it is clear that the results above are not tied to the chosen parameters. As long as changing the parameters does not change the phase the system is in, the results remain valid.

The Kitaev model is a member of class D since only particle-hole symmetry is present[5], and a $\mathbb{Z}_2$-topological insulator in one dimension. We note that the standard BdG Hamiltonian for the Kitaev chain is given by $H = \frac{1}{2} \sum_k \Psi_k^\dagger H_k \Psi_k$, where the sum again runs over the whole Brillouin zone, $H_k = E(k)\sigma_3 + \Delta_k \sigma_2$ and $\Psi_k, \Psi_k^\dagger$ denote the Nambu-spinors. However, to keep the story more general, we can assume that H_k represents the general two-level system in eq. (1.10). Since $\sigma_1 H_k^T \sigma_1 = -H_{-k}$, particle-hole symmetry is represented by $U_C = \sigma_1$. Thus all components but $i = 3$ have to be odd functions in k, i.e. $h_{i=1,2}(-k) = -h_{i=1,2}(k)$ while $h_3(-k) = h_3(k)$, where we again ignored the innocent shift in energy proportional to h_0. Similar to our discussion of time-reversal symmetry in the context of topological insulators, it follows that due to the particle-hole symmetry we can focus on the (effective) Brillouin zone, i.e. $k \in [0, \pi]$. In addition, we define the map $\hat{h} = h/|h|$ from the Brillouin zone to the sphere S^2. Particle-hole symmetry requires that the vector $\hat{h}$ at the boundaries $\bar{k}$ of the effective Brillouin zone, is given by

$$\hat{h}(\bar{k}) = \hat{h}_3(\bar{k})e_3,$$

where $\bar{k} = 0, \pi$. The coefficients $\hat{h}_3(\bar{k})$ are determined by the sign of the kinetic energy[6] (relative to E_F) in the Hamiltonian. It is easy to see that in the trivial phase of the Kitaev model, both signs are equal and $\hat{h}(0) = \hat{h}(\pi)$ is the north pole in S^2. Whereas in the non-trivial phase, $\hat{h}(0) = -\hat{h}(\pi)$ and the vectors is either pointing towards the north or south pole. The product of both functions defines a natural $\mathbb{Z}_2$ invariant

$$\nu = \hat{h}_3(0)\hat{h}_3(\pi).$$

Tracking the image of $\hat{h}$ on S^2 will result in a curve that starts and ends at the north pole (trivial phase) or starts at the north and ends at the south pole (non-trivial), as illustrated in fig. 3.3. Thus $\nu = \pm 1$ corresponds to two inequivalent trajectories. From the construction above it is evident that $\hat{h}(k)$ is ill-defined when the bulk gap closes and a sign change in ν appears. The latter corresponds to the obstruction to connect the non-trivial phase to the trivial vacuum in the Kitaev model.

3.2.3 Splitting of edge states

Earlier we have chosen two explicit sets of parameters corresponding to two distinct phases of the Kitaev model. However, since the appearance of the phases is of topological origin we are of course not fixed to this setting. As long as the parameters are chosen in a way that the chain is in one of the two phases, everything said above is still valid. When deviating from the limit $\mu = 0 \neq t = \Delta$, the distribution of the Majorana modes decays exponentially within

---

[5]Indeed there is an artificial time-reversal symmetry present which however does not alter the class D membership, as we discuss later.

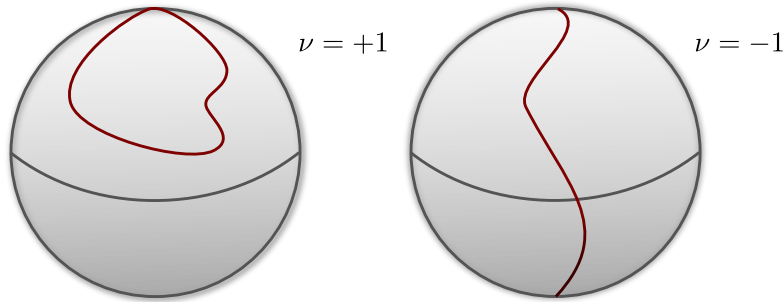[6]The kinetic term is proportional to $E(k)\sigma_3$.

Figure 3.3: Trajectory of the map $\hat{h}$ on the sphere. Left: In the trivial case with $\nu = +1$, the vector starts and ends at the north pole. Right: In the non-trivial case, the map explores the sphere from the north to the south pole, thus $\nu = -1$. Image inspired by ref. [71].

the bulk. Thus, if the chain L is not long enough, the two modes talk to each other as their wave functions overlap. As a result, there will be an exponential splitting of the Majorana modes which happens on the scale of $e^{-L/\xi}$, where ξ is the coherence length. Therefore, in order to avoid such entanglement the wire has to be sufficiently long, $L \gg \xi$.

3.3 Majorana fermions in real (one-dimensional) life — Quantum wires

Experimental realisation of p-wave superconductors remains an open problem. Besides the justified scepticism towards an actual realisation of p-wave superconductors, one might be sceptical about their applicability to real world topological quantum computing. Stable realisations are most likely lacking sufficient superconducting correlations of long-range order, necessary for effectively spinless systems. Furthermore, strong correlations lead to possible problems regarding the controllability. However, despite this rather devastating jeremiad against the realisation of p-wave superconductors, the possible experimental realisation of Majorana fermions is saved by - who else but - topology. Since the occurrence of Majorana particles in odd parity pairing systems is a universal feature, an experimentally more accessible system of the same symmetry class will host the latter without the need for an actual p-wave superconductor. Among the first to realise this were Fu and Kane [75, 81] who considered a thin semiconducting film sandwiched between a magnetic insulator and an s-wave superconductor. Such a two-dimensional system hosts Majorana fermions at vortices and while the actual realisation of these systems proved to be very challenging, the direction towards sandwiched hybrid systems, given by the authors was hugely useful and paved the way for a plethora of proposals (see ref. [71] and [82] and references within). Experimentally, the most promising candidates for the realisation of Majorana fermions are one-dimensional quantum wires. In two seminal works [14, 15], the realisation of Majorana fermions at the ends of one-dimensional (semiconductor) wires with sufficient spin-orbit coupling proximity

coupled to a conventional s-wave superconductor together with an external magnetic field, was suggested. We now review the emergence of Majorana particles in such quantum wires following ref. [14, 15][7].

The setup is illustrated in fig. 3.4, with the quantum wire put on top of the superconductor. The Rashba spin-orbit coupling [83] is assumed to be perpendicular to the wire and along the axis of the superconductor. An external magnetic field B is introduced which is considered to be perpendicular to both, the spin-orbit coupling and the wire. We fix the axes according to fig. 3.4, i.e. the magnetic field $B = -B(z)e_z$, the spin-orbit coupling $\alpha = \alpha e_y$ and the wire is lying along the x-axis. The s-wave superconductor induces a pairing amplitude Δ in the wire due to the proximity effect ([14, 84]).
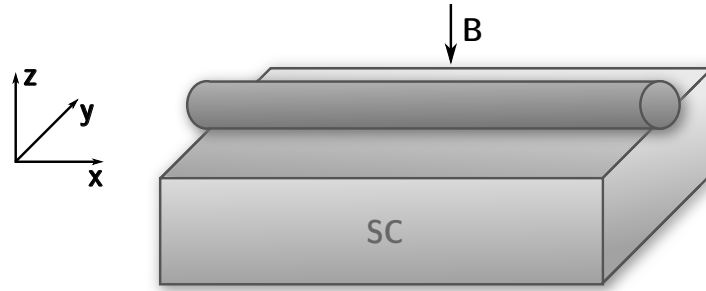
Figure 3.4: Model of a Rashba spin-orbit coupled, quantum wire in proximity to an s-wave superconductor. A magnetic field B is applied perpendicular to the wire axis. The spin-orbit coupling is perpendicular to the wire and lies along the superconductor axis. Majorana fermions are localised at the ends of the wire, decaying exponentially into the wire if the latter is finite (the decay length is non-zero for finite systems and it vanishes in the infinite limit).

Following the description in the previous paragraph, we can readily give the Bogoliubov-de-Gennes (BdG) Hamiltonian

$$\mathcal{H} = \frac{1}{2} \int \mathrm{d}x \, \Psi^\dagger(x) \begin{pmatrix} H_0 & i\sigma_y\Delta^* \\ -i\sigma_y\Delta & -H_0^{\mathrm{T}} \end{pmatrix} \Psi(x), \tag{3.3}$$

where

$$H_0 = -\partial_x^2/2m - \mu(x) + B(z)\sigma_z - i\alpha\sigma_y\partial_x,$$

and the Pauli matrices σ_i act in the spin space. The spinors acting in the product space of

---

[7]Although both works differ in details the general strategy behind both proposals is equivalent.

particle-hole and spin are defined by

$$\Psi(x) = (\psi_\uparrow, \psi_\downarrow, \psi_\uparrow^\dagger, \psi_\downarrow^\dagger)^{\mathrm{T}}.$$

Before exploring the mechanism behind the emergence of Majorana fermions, we discuss the symmetries of the system. H_0 as well as $(-\tau_y \otimes \sigma_y \Delta)$ is a symmetric matrix[8], where the τ-matrix acts in particle-hole space now. We can rewrite the Hamiltonian as

$$\mathcal{H} = \frac{1}{2} \int \mathrm{d}x \, \Psi^\dagger(x)(\tau_z \otimes H_0 - \Delta\tau_y \otimes \sigma_y) \, \Psi(x), \tag{3.4}$$

with particle-hole symmetry represented by $U_C = \tau_x$. However, since $\mathcal{H}$ is symmetric, the system possesses an 'artificial' chiral symmetry represented by $U_S = U_C = \tau_x$ and therefore an 'artificial' time-reversal symmetry. According to the classification given in table 1.1, in case of a single channel the system would belong to class BDI. However, as we will see in a moment, the spin-degree of freedom is effectively frozen out by spin-polarisation due to the magnetic field (keep in mind that our goal is to construct an effectively spinless p-wave superconducting phase). Therefore, a physical time-reversal symmetry is not present and the system can be regarded as a member of class D. In the single-channel case, at most one Majorana fermion per end can be present negating a distinction between class D and BDI, both classified by a $\mathbb{Z}_2$-topological invariant. Note that the same arguments hold for the Kitaev model introduced in section 3.2.2. As a direct consequence, the Majorana particles at the end of the wire are invariant under the introduction of explicitly time-reversal breaking terms in the Hamiltonian (3.3). One important consequence of the particle-hole symmetry is that a Majorana fermion, represented by $\Psi_i = \Psi_i^\dagger$, has to be tied to zero energy since for each non-zero energy ϵ_i solution, there exists a solution of the BdG equation with energy $-\epsilon_i$. Thus, Majorana fermions, if present, have to be localised at zero-energy.

Let us return to the Hamiltonian (3.4). The effect of the spin-orbit coupling can be illustrated at the single-particle spectrum in the case of vanishing magnetic field and pairing amplitude, $B = \Delta = 0$. In this case, due to the spin-orbit coupling, the spectrum is given by two intersecting parabolas,

$$E_\pm(k) = k_x^2/2m - \mu \pm \sqrt{B^2 + (\alpha k_x)^2},$$

one for each spin component, shifted from the origin (illustrated in fig. 3.5). Independent of the value of μ, a spin-degeneracy is always present and an effective spin-less regime, as desired for the p-wave superconductivity, is impossible to reach. Upon increasing the magnetic field $B \neq 0$, this degeneracy is lifted as a gap opens at $k = 0$ (with each part of the spectrum comprised by two spin components). If the chemical potential μ is placed within this gap, the spectrum has no spin-degeneracy and an effective spinless regime can be achieved,[9] illustrated

---

[8]We have chosen Δ to be real.

[9]Note however, that the spin direction still depends on the momentum.
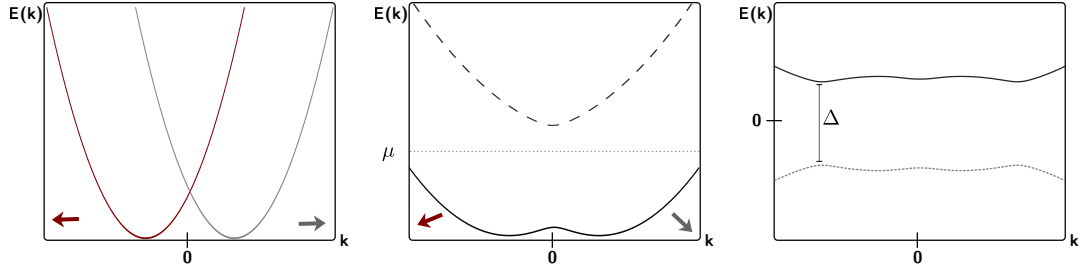
Figure 3.5: Band structure of the quantum wire. Left: $B = \Delta = 0$. Spin-orbit coupling splits two parabolas with different spin polarisation (red, grey). Middle: Small but finite magnetic field $B > 0$ opens a gap at $k = 0$ allowing for an effective spinless representation. Spin-polarisation does still depend on momentum, though. The chemical potential (dotted) is placed inside the gap. The upper band (dashed) can be projected out, provided $B \gg \Delta$. Right: Superconducting gap $\Delta > 0$ is present and the band structure is mirrored due to the BdG structure. Note that the upper band has been projected out.

in fig. 3.5. As we will see later, the gap should be chosen sufficiently large (by increasing B) to allow for disorder or thermal fluctuations in the chemical potential. With increasing magnetic field, the alignment of each spin component within each band increases. Since the latter aggravates the introduction of proximity-coupled superconductivity, the magnetic field has to be chosen appropriately. For $\Delta \ll B$, the upper unoccupied band can effectively be projected out and the only partially polarised electrons in the lower band are effectively p-wave paired (see fig. 3.5).

Assuming that the chemical potential is placed within the gap, it can be shown that the system in this state can continuously be mapped onto the Kitaev model of p-wave superconductors with $|\mu| < t$, [11]. Thus, the system is in the topological non-trivial state. From the inspection of the spectrum in presence of the superconductor at $k_x = 0$,

$$ E_\pm = \pm \sqrt{B^2 + \Delta^2 + \mu^2 \pm 2\sqrt{B^2 \Delta^2 + B^2 \mu^2}}, $$

it can be seen that with increasing Δ, the gap decreases and closing is achieved at the critical point $B_C = \sqrt{\Delta^2 + \mu^2}$. Upon further increase, the gap reopens with the wire in the topologically trivial state and the effective spinless regime is lost. Thus, one concludes that the quantum wire is in the topologically non-trivial phase if $B > B_C$ while it is trivial if $B < B_C$. Note however, that instead of modulating the magnetic field B or the order parameter Δ, it turns out that it is experimentally more convenient to change the chemical potential μ, [15]. Assuming that $B > \Delta$ the Majorana fermion is located at the interface between the regions with $\mu^2 < \mu_c^2$ and $\mu^2 > \mu_c^2$, with the critical chemical potential $\mu_c = \sqrt{B^2 - \Delta^2}$. As described in ref. [15], such a variation of the chemical potential can be achieved by gate

electrodes under the wire.

3.3.1 Clash of parameters — Spin-orbit coupling vs. magnetic field

We leave our safety zone of a completely idealised system for a moment to attempt grasping a few issues experimentalists face. Following the discussion above, it would be tempting to chose a very large magnetic field to ensure the presence of a large topological regime and to enlarge the gap at zero momentum. The latter is especially desired since it minimises the susceptibility of the system to disorder fluctuations (or effects like temperature) in the chemical potential. On the downside, a large magnetic field strongly polarises the spins of the system which in return complicates the introduction of p-wave pairing and thus a semiconductor with a large g-factor has to be chosen for the quantum wire [71]. As if this would not be enough, the strength of the spin-orbit coupling proves to be a crucial parameter. Consider a magnetic field large compared to the spin-orbit coupling, i.e. the ratio of magnetic field B to the spin-orbit energy $E_{\mathsf{SO}} = \frac{m}{2}\alpha^2$ is large. In this case, due to the strong polarisation of spins near the Fermi level, time-reversal symmetry is strongly violated. As a consequence, the gap may be closed due to disorder fluctuations. If however, the ratio B/E_{SO} is small, spin-orbit coupling ensures a *local* time-reversal symmetry at the Fermi level, which renders the system more stable against disorder [84, 85]. We conclude by noting that finding the right balance of parameters; to provide a sufficiently large stable topological regime to operate in, while protecting the system against disorder is a very delicate manner. Promising candidates were found in InAs and InSb wires. Both materials provide high g factors, a good susceptibility to proximity induced superconductivity as well as long mean free paths [71]. Unfortunately, it turns out that due to the small energy scale of E_{SO}, these systems give experimentalists a hard fight to reach the topological phase and disorder effects play an important role (a point we will discuss in length later).

Note that recently very promising proposals in cold atom experiments, free from disorder, have been formulated [86–88]. Inspired by ref. [14, 15], an enormous amount of proposals regarding the construction of Majorana fermions (in various systems and dimensions) in experiments, have seen the light of day. An extensive list and discussion can be found in ref. [71]. Among the suggestions, multi-channel quantum wires promised to be very well suited for the actual realisation of Majorana fermions in one dimension. The latter can be considered as the quasi-one-dimensional extension of the quantum wire systems discussed earlier. It turns out, that multi-channel wires are more suitable to describe InAs and InSb semiconducting wires used in experiments. The reason being that in these systems multiple subbands are occupied and multi-channel wires do not require a complicated gating to the lowest of these bands, but rather only rely on the presence of an odd number of partially occupied bands (a requirement that is trivially fulfilled). A detailed theoretical discussion of multi-channel wires can be found in section 4.2.

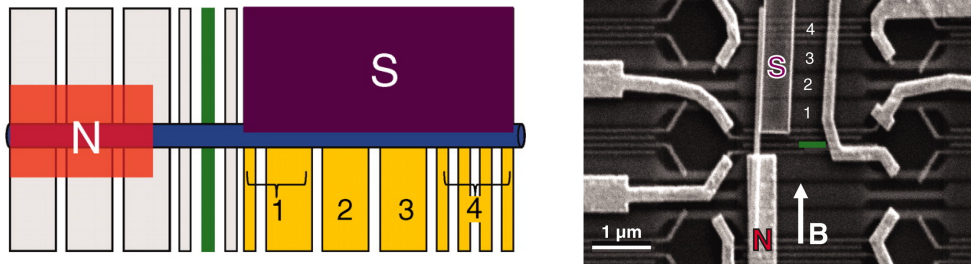## 3.4 Experimental *observation* of Majorana fermions in tunnelling experiments

Figure 3.6: A schematic representation (left) and the real experimental setup (right) used in [12]. The quantum wire is in contact with a superconductor (S) and a normal lead (N), separated by a tunnel barrier (green rectangle). The magnetic field B is applied along the wire axis. Underlying gates are indicated by numbered yellow rectangles. A possible Majorana fermion will localise at the contact point of tunnel barrier and quantum wire. Picture taken from [12].

Several experimental groups reported the observation of Majorana fermions in spin-orbit coupled semiconductor nano wires coupled to an s-wave superconductor [12, 13, 89, 90]. The evidence was drawn from zero-bias conductance peaks in local conductance measurements. In the most prominent experiment [12], on which we focus now, an InSb nano wire was brought in contact with NbTiN (a superconductor) and an Au lead. The setup is illustrated in fig. 3.6. As discussed earlier, InSb shows a high g-factor in addition to strong (Rashba) spit-orbit coupling, with $g \simeq 50$ and $\alpha \simeq 0.2$eVÅ [74], respectively. A bias voltage is applied between the superconductor and the normal lead. By applying a negative voltage to a narrow gate in the region between the superconductor and the metallic lead, a tunnel barrier is created. At this tunnel barrier the Majorana fermion has to localise, if the system is brought to the topological phase. The differential conductance $\mathrm{d}I/\mathrm{d}V$ is then measured as a function of the voltage for different values of the magnetic field. A zero-bias conductance peak is expected if the magnetic field exceeds the critical field and the system is in the topological phase. The experimental data are shown in fig. 3.7 and for a field exceeding about 100mT a peak is present. Notice the splitting of the peak for large magnetic fields (a point to which we return later).
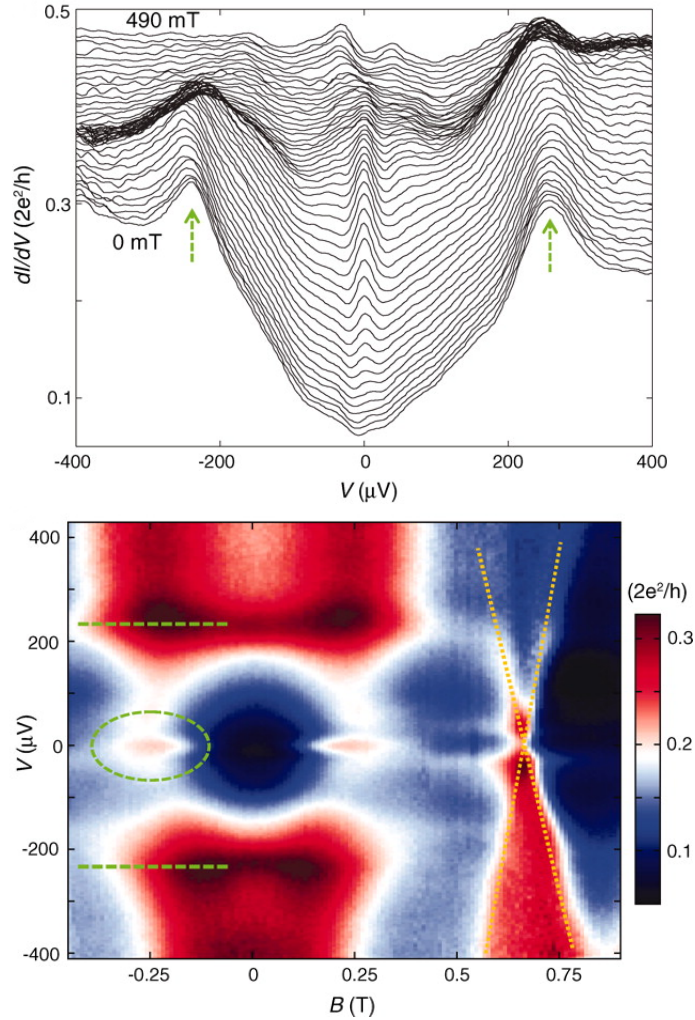
Figure 3.7: Magnetic field-dependent spectroscopy results. Top: The differential conductance $\mathrm{d}I/\mathrm{d}V$ versus voltage V is shown for different magnetic fields B. The green arrows indicate the induced gap. A zero-bias central peak is visible for a range of field strengths before splitting. Bottom: Density plot of the differential conductance versus voltage V and field B. The zero-bias central peak is marked with a dashed ellipse and green dashed lines indicate the gap. For a field of approx. 0.6T the peak splits (yellow dotted lines). Picture taken from [12].

4

Quasiclassical theory of disordered multi-channel Majorana quantum wires

In 2012 several experimental groups [12, 13, 89] reported the successful observation of Majorana fermions in spin-orbit and proximity coupled quantum wires [14, 15]. A zero-bias spectral peak in the tunnelling conductance into the wire was provided as evidence for the presence of a Majorana fermion. The claim was further substantiate by an investigation regarding the field dependence of the peak. Shortly after the ostensible discovery, it was pointed out by ref. [19] that for a multi-channel system, small amounts of disorder are sufficient to lead to a signature in the averaged density of states, that is almost indistinguishable from the Majorana peak observed in the experiments. This disorder induced *spectral peak* mimics the Majorana peak in almost all relevant aspects and therefore leaves the presented experimental results inconclusive. Its origin however, is solely due to strong midgap quantum coherence. Loosely speaking, the absence of energy repulsion between Andreev levels in symmetry class D may lead to clustering of Andreev bound states around zero-energy [4]. Given the limited resolution of tunnelling spectroscopy, this structure may superficially merge into a single peak.

In this chapter we discuss disordered multi-channel Majorana quantum wires in the context of the quasiclassical approximation introduced in chapter 2. We derive the Bogoliubov-de Gennes Hamiltonian for the disorder multi-channel quantum wire and discuss its symmetries. Under the assumption that the spin-orbit energy exceeds the magnetic field and the pairing amplitude, the quasiclassical approximation, i.e. the linearisation of the Hamiltonian, is justified. The experimental setup is then mapped to the prototypical model discussed in section 2.2, granting access to the results of chapter 2. We represent the $\mathbb{Z}_2$-topological invariant in terms of the Eilenberger function of the terminal regions to which the quan-

tum wire is connected. The latter indicates the presence or absence of Majorana fermions localised at the ends of the wire, depending on the chosen parameters. In this regard, the present chapter serves as an extended example for the application of the formalism to class D.

Drawing on the relative simplicity of the Green's functions within the quasiclassical approach, we present an effective numerical method to calculate the Eilenberger function for the full disordered system. The averaged density of states at the tunnel barrier is then calculated. The latter clearly signals the coexistence of two peaks, a topological Majorana fermion and a 'trivial' disorder induced one. While the former is only present in the topological regime, the latter is shown to appear in the trivial regime. Our results support the scepticism towards the experimental evidence based on zero-bias conductance peaks, addressed in ref. [19].

In the final part of this chapter we present results of an ongoing study of disorder stabilised topological excitations. Using the numerical method presented in this chapter, we investigate systems at criticality and the influence of disorder fluctuations. Numerical results hint towards the possible formation of stable topological excitations at local domains within the system, induced by disorder.

Parts of the results discussed in this chapter can be found in ref. [91] and [92].

4.1 Class D spectral peak

In the experiments discussed in the previous chapter, evidence for the presence of Majorana fermions in proximity coupled spin-orbit quantum wires was drawn from a zero-bias spectral peak in the tunnelling conductance. Representing an irrefutable proof in an idealised system (cf. section 3.2.2), the spectral peaks cogency is drastically reduced in a more realistic situation, involving multiple channels and disorder. The tunnelling conductance is directly related to the local density of states and the presence of a Majorana fermion should result in a band centre anomaly in the latter.

The presence of even moderate amounts of disorder in a multi-channel quantum wire may lead to the emergence of a second band centre anomaly, originating not from topology but from strong midgap quantum interference [19]. This peak, called *class D spectral peak*, in the averaged local density of states has striking similarities in all relevant features of the Majorana peak. It is rigidly locked to zero energy, its width is of the order of the mean level spacing and it relies on the same parametric conditions as those required for a Majorana fermion (a point to be discussed in details later). However, contrary to the latter it requires a moderate amount of disorder. The non-linear-sigma-model for a multi-channel variant of the model used in ref. [15], was derived by Bagrets and Altland [19]. The resulting averaged density of states (in rescaled energy units s) for the system [93] are given by

$$\nu(s) = 1 + (-1)^N \sin(s)/s + \frac{1}{2}(1 + (-1)^{N+1})\delta(s/2\pi),$$

where N denotes the number of channels present. Only in the non-trivial case of an odd number of channels, the density of states shows a Majorana peak at zero energy, represented by the delta distribution $\delta(s/2\pi)$. In this case the symmetry class is called B. For N even, the averaged density of states shows a broadened peak ($\sim \sin(s)/s$), the aforementioned *class D spectral peak* and the symmetry class in this case is D. Class D and B share the same symmetries, time-reversal symmetry broken and intrinsic particle-hole symmetry present, differ however by the number of levels. The formation of the anomaly in class D is solely due to diffusion modes and has no topological origin. A schematic profile of the averaged density of states is shown in fig. 4.1.
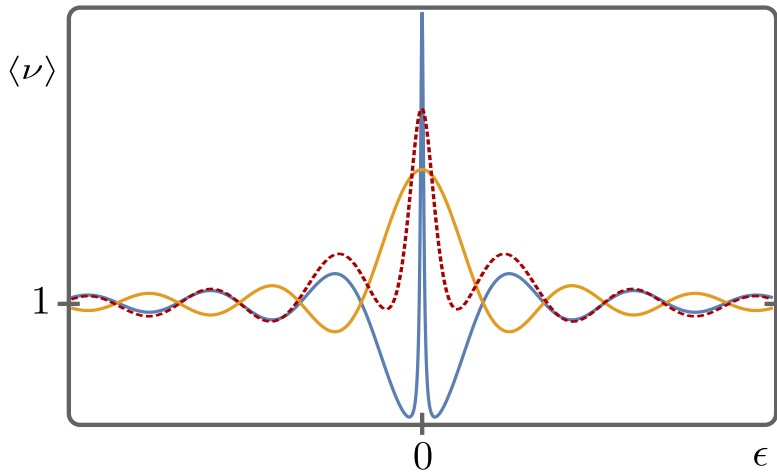
Figure 4.1: Averaged density of states $\langle \nu(\epsilon) \rangle$ for class D (orange) and class B (blue) obtained from random matrix theory. In both cases a peak at zero energy is present. Class B possesses a δ-peak bound to the band centre due to a Majorana fermion. The broadened version of this peak is given by the dashed red curve. In class D the spectral peak is due to clustering of energy states around zero energy.

Both density of states profiles, superficially look very alike. Since the spectral weight of both is of the same order, a distinction of both structures is limited by a very fine resolution (which is of the order of the mean level spacing δ). Consequently, the unambiguous identification of Majorana fermions in tunnelling spectroscopy experiments with resolutions limited to scales larger than the mean level spacing, may prove difficult.

Before turning to a more detailed description of disordered multi-channel quantum wires, we demonstrate the deceptive nature of the class D anomaly, using a random matrix toy model (see refs. [94–96] for reviews on random matrix theory). Figure 4.2b shows the spectrum of a class D random matrix ensemble, where a system parameter r is varied. In the experiments the latter would correspond to the magnetic field B for instance. Accidental level crossings at zero energy are present. In fig. 4.2b the ensemble-averaged density of states is shown as a

function of energy and system parameter r. It appears as if a peak localised at the band centre ($E = 0$) is present for a large range of r before splitting. Qualitatively, these picture shows striking similarity to the experimental observation in fig. 3.7. In the latter, the peak splits into two Andreev bounds states for a magnetic field B exceeding 0.5T, and no satisfactory explanation was provided by the authors. In the random matrix toy model of class D, no Majorana state is present and the peak is merely superficial, as it can be seen from fig. 4.2a. The appearance of the peak is due to the finite resolution, which fuses the close crossings and splitting. A band with a series of crossings at zero energy that have a very narrow support, renders the ensemble-averaged density of states of class D to be indistinguishable from a non-trivial system. These simple arguments underline that a midgap spectral peak does not serve as an unambiguous evidence for a Majorana fermion[1]. Figure 4.2a shows the same plots for class C. Systems of class C are only constraint by particle-hole symmetry. However, in class C spin-rotation symmetry is not violated ($C^2 = -1$) and the class is trivial in one dimension, hosting no Majorana fermions. Due to the particle-hole symmetry the levels with energies $\pm\epsilon$ repel each other in class C, whereas in class D this level-repulsion is absent at the Fermi level and clustering is possible, [4]. As a consequence, the midgap spectral peak in the latter case is turned into a midgap spectral dip in class C. As it is clearly visible in the top panel of fig. 4.2a, no level crossing occurs.

4.2 Multi-channel quantum wire

We now turn to the detailed analysis of multi-channel Majorana quantum wires. We consider the setup shown in the upper part of fig. 4.3, representing the experimental setup of ref. [12] discussed in section 3.4. A semiconductor quantum wire subjected to strong spin-orbit coupling is proximity coupled to an s-wave superconductor (S). Through a tunnel barrier (T) the wire is connected to a normal metal lead (N), to which a small excess voltage, V, is applied and thus a tunnel current into the central region is induced. In order to extract the density of states, the differential conductance $\mathrm{d}I/\mathrm{d}V$ is measured relative[2] to the chemical potential μ. As mentioned earlier, an anomaly in the density of states at the band centre ($V = 0$) is believed to correspond to the presence of a Majorana fermion localised at the tunnel barrier. In the lower part of fig. 4.3, the profiles for the gate-induced potential V, the chemical potential μ, as well as the order parameter Δ are presented. Andreev bound states, which will be present in the scattering region, are indicated by dashed lines in this figure. The latter prove to be crucial for the emergence of the class D spectral peak, as we will see later.

---

[1] The attentive reader might have noticed, that we have already discussed a possible effect leading to the splitting of the spectral peak for high magnetic fields in sec. 3.3.1. A high magnetic field might destroy the possibility to introduce p-wave superconductivity in the quantum wire. For completeness we note that in ref. [13] this issue was addressed and the aforementioned splitting was utilised to underline the findings of a Majorana particle. At any rate, the results remain inconclusive.

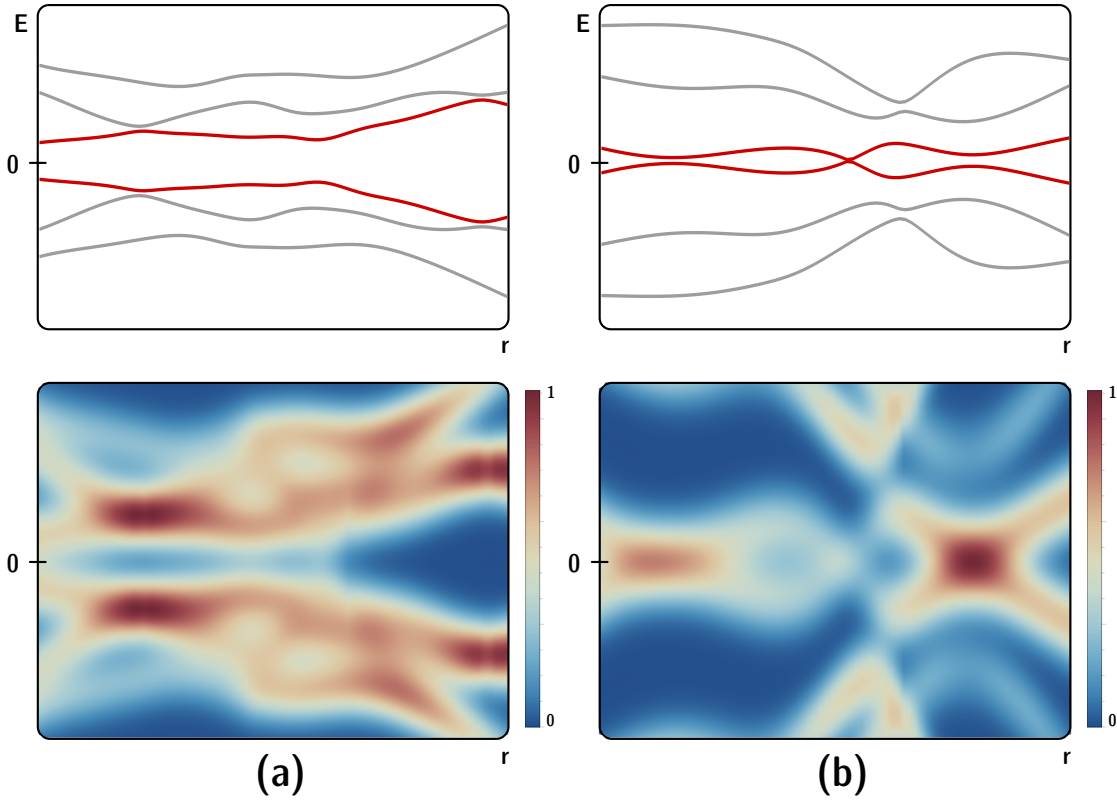[2] Note that we chose the units $e = \hbar = c = 1$.

Figure 4.2: Top left: Spectrum of a random matrix ensemble of class C, as a function of a system parameter r. Over the whole range of r the lower bands repel each other. Bottom left: The corresponding ensemble-averaged density of states profile, as a function of energy and r. Clearly no central peak is visible. Top right: Spectrum of a random matrix ensemble of class D. At zero-energy band crossings occur. Bottom right: The corresponding ensemble-averaged density of states. A spectral peaks are visible at the left and right end. The splitting of the right peak into two peaks is visible.

4.2.1 Hamiltonian of the model

We consider a multi-band quantum wire, proximity coupled to an s-wave superconductor and subject to Rashba spin-orbit coupling and a magnetic field. We assume that the wire lies along the x-axis and is of length l_x and of width l_z. The magnetic field B is applied along the wire axis and the spin-orbit coupling is along the z-axis, while the y-axis is perpendicular to the superconductor surface. The BdG Hamiltonian $\mathcal{H}$ for the system in the xz-plane is a
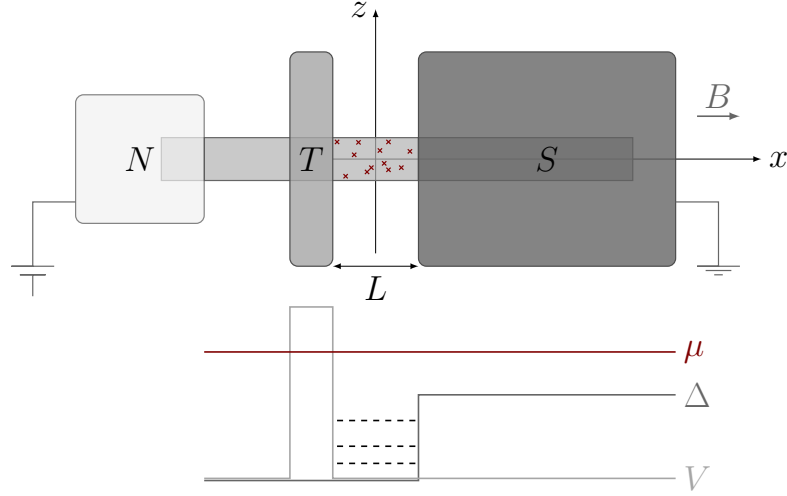
Figure 4.3: Top: Model of the quantum wire composed of a spin-orbit nano wire terminated by a tunnel barrier (T) and a superconductor (S). A magnetic field B is applied along the wire axis. Bottom: Profiles of the superconducting gap $\Delta(x)$, the chemical potential $\mu(x)$ and the gate induced potential $V(x)$. The dashed lines illustrate Andreev bound states present in the scattering region of length L. Picture taken from [91].

variant of eq. (3.3) and reads

$$\mathcal{H} = \frac{1}{2} \int \bar{\Psi}(x,z) \begin{pmatrix} \hat{H}_0 + \hat{H}_{\text{so}}^{\perp} + \hat{W} & i\sigma_y^{sp}\Delta^* \\ -i\sigma_y^{sp}\Delta & -\hat{H}_0^{\text{T}} - (\hat{H}_{\text{so}}^{\perp})^{\text{T}} - \hat{W}^{\text{T}} \end{pmatrix} \Psi(x,z)\,\mathrm{d}x\,\mathrm{d}z, \quad (4.1)$$

with

$$\hat{H}_0 = -\frac{(\partial_x^2 + \partial_z^2)}{2m} - \mu(x) + B(x)\sigma_x^{sp} - i\alpha(\sigma_z^{sp}\partial_x). \tag{4.2}$$

Here we have chosen the spinor Ψ to be arranged as $\Psi = (\psi_\uparrow, \psi_\downarrow, \bar{\psi}_\uparrow, \bar{\psi}_\downarrow)$. The superconducting pairing amplitude $\Delta = \Delta(x)$ is induced by the proximity to the superconductor and the magnetic field is given by[3] B. The Rashba spin-orbit coupling with respect to both, the transverse and the longitudinal momentum, is represented by the two terms $-i\alpha\partial_{x,z}$, where α is the coupling constant. For reasons that will become clear later, we combine the transverse contributions in a separate Hamiltonian

$$\hat{H}_{\text{so}}^{\perp} = i\alpha\sigma_x^{sp}\partial_z, \tag{4.3}$$

---

[3]More exactly, B is related to the actual applied external field H via $B = \frac{1}{2}g\mu_B H$.

where the Pauli matrices σ^{sp} act in spin space. Disorder is modelled by adding the random Hamiltonian $\hat{W}$, which is assumed to preserve the symmetries of $\mathcal{H}$. Details of $\hat{W}$ will be discussed later. We assume a quasi one-dimensional geometry, i.e. a thin wire with a width that is small compared to its length ($l_z \ll l_x$) and therefore introduce quantisation along the transverse direction. Since $\hat{H}_0$ is separable with respect to the coordinates x and z, we can decompose the fields into

$$\psi_\sigma = \sum_{n\sigma} \Phi_n^\sigma(z)\psi_\sigma^{(n)}(x),$$

and $\bar{\psi}_\sigma$. We denote the transverse wave functions by $\Phi_n^\sigma(z)$, with spin index $\sigma = \uparrow, \downarrow$ and band index n. The transverse wave functions for an ideal wave guide are given by $\Phi_n^\sigma(z) = \sqrt{\frac{2}{l_z}} \sin\left(\frac{n\pi}{l_z}z\right)$. Taking the band index (n) into account, the Hamiltonian (4.1) takes the form

$$\mathcal{H} = \frac{1}{2}\int \bar{\Psi}^{(n)} \begin{pmatrix} \hat{H}_0^{(n)}\delta_{nm} + (\hat{H}_{\mathsf{SO}}^\perp)_{nm} + \hat{W}_{nm} & i\sigma_y^{sp}\Delta^*\delta_{nm} \\ -i\sigma_y^{sp}\Delta\delta_{nm} & -(\hat{H}_0^{(n)})^{\mathrm{T}}\delta_{nm} - (\hat{H}_{\mathsf{SO}}^\perp)_{mn} - \hat{W}_{mn}^{\mathrm{T}} \end{pmatrix} \Psi^{(m)}\mathrm{d}x,$$

where $\hat{H}_0^{(n)}$ is given by

$$\hat{H}_0^{(n)} = -\frac{\partial_x^2}{2m} + \mu_z^{(n)} - \mu(x) + B(x)\sigma_x^{sp} - i\alpha\sigma_z^{sp}\partial_x. \tag{4.4}$$

The chemical potential of the n-th band $\mu_z^{(n)}$ can be calculated directly using the kinetic term in z-direction, yielding

$$\mu_z^{(n)} = \tfrac{\pi^2 n^2}{(2ml_z^2)}. \tag{4.5}$$

Next we argue that the transverse spin-orbit coupling, $\hat{H}_{\mathsf{SO}}^\perp$, does not contribute in a disorder dominated regime and will therefore be absorbed into the random Hamiltonian. To this end we notice that the spin-orbit interaction can be directly integrated to

$$(H_{\mathsf{SO}}^\perp)_{nm} = \frac{2i\pi\alpha m}{l_z}\sigma_x^{sp}\int_0^{l_z} \sin\left(\frac{n\pi z}{l_z}\right)\cos\left(\frac{m\pi z}{l_z}\right)\mathrm{d}z$$

$$= -\frac{2i\alpha}{l_z}\frac{nm}{n^2-m^2}(1-(-1)^{n+m})\sigma_x^{sp}.$$

We assume a thin wire, i.e. $l_z \lesssim l_{\mathsf{so}} = \hbar/(m\alpha)$ with l_{so} being the spin-orbit length. Under this assumption, the above expression is small compared to the kinetic part (4.5), i.e. $(H_{\mathsf{SO}}^\perp)_{nm} \ll \mu_z^{(n)}$. This assumption is indeed justified since the estimated wire length and spin-orbit length

in the experiments [12] are approximately given by $l_z \approx 100$nm and $l_{so} \approx 200$nm, respectively. Therefore the spin-orbit contribution can be treated perturbatively. In order to do so, we diagonalise the high-energy part of the Hamiltonian, $(\mu_z^{(n)} \delta_{nm} + (H_{so}^\perp)_{nm})$ with help of a unitary transformation $\hat{U}$. Since the perturbation $H_{so}^\perp$ is very weak, $\hat{U}$ is essentially the identity and its generators $\hat{X}$, i.e. $\hat{U} = \exp(i\hat{X}) \simeq 1 + i\hat{X}$ are of order $\mathcal{O}(l_Z/l_{so})$. The latter are calculated by perturbation theory and to first-order are given by

$$\hat{X}_{nm} \simeq \frac{i(H_{so}^\perp)_{nm}}{\mu_z^{(n)} - \mu_z^{(m)}}, \text{ for } n \neq m,$$

$$\hat{X}_{nn} = 0.$$

To keep our notation simple, or at least to not exacerbate it, we absorb the unitary transformation $\hat{U}$ into the definition of the spinor fields, i.e. $\Psi \rightarrow \hat{U}\Psi$ and $\bar{\Psi} \rightarrow \bar{\Psi}\hat{U}^\dagger$, as well as into the disorder potential $\hat{W} \rightarrow \hat{U}\hat{W}\hat{U}^\dagger$. Recalling the definition of the one-dimensional Hamiltonian $\hat{H}_0^{(n)}$ in (4.4), we notice that only the (longitudinal) spin-orbit term does not commute with the generators $\hat{X}$. The same holds for the superconductor contribution. To take these contributions into account, we introduce small corrections to the Hamiltonian for both, the spin-orbit coupling $V := \alpha[\hat{X}, \sigma_z^{sp}]_-\partial_x$ and the pairing amplitude $\delta\hat{\Delta} := -\Delta[\hat{X}, \sigma_y^{sp}]_-$. The approximate Hamiltonian then reads

$$\mathcal{H} \simeq \frac{1}{2} \int \bar{\Psi}^{(n)} \begin{pmatrix} \hat{H}_0^{(n)}\delta_{nm} + \hat{V}_{nm} + \hat{W}_{nm} & i\sigma_y^{sp}\Delta\delta_{nm} + (\delta\hat{\Delta})_{nm} \\ -i\sigma_y^{sp}\Delta\delta_{nm} + (\delta\hat{\Delta})_{nm}^* & -(\hat{H}_0^{(n)})^{\mathrm{T}}\delta_{nm} - \hat{V}_{mn}^{\mathrm{T}} - \hat{W}_{mn}^{\mathrm{T}} \end{pmatrix} \Psi^{(n)}\mathrm{d}x \quad (4.6)$$

Given that we are interested in the low-energy physics, in a regime where the effects of disorders are dominant, we can safely neglect the contributions of $\hat{V}$ and $\delta\hat{\Delta}$ and therefore omit both terms henceforth.

4.2.2 Topological band

For single-channel quantum wires we learned that the wire is in the topologically non-trivial phase (i.e. it can formally be mapped to the non-trivial phase of a p-wave superconductor), if the magnetic field B exceeds a certain critical field B_c. For the multi-band wire we now assume that the chemical potential μ lies close to the bottom of the N-th band, i.e. $\mu \simeq \mu_z^{(N)}$. Due to the absence of inter-band scattering, it is this band that determines whether the system is topologically trivial or not, hence we refer to this specific band as *topological band*. In analogy to our single-channel discussion, the critical field is then given by
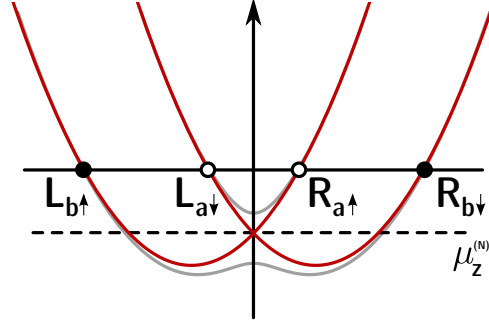
$$B_c = \sqrt{\Delta^2 + (\mu - \mu_z^{(N)})^2}.$$

Figure 4.4: One-dimensional chiral fermions (R/L) are introduced in the spin-orbit quantum wire. The open and filled dots represent channels a and b, respectively. The dispersion relation for the a-channel is affected by the magnetic field B only if the chemical potential lies close to $\mu_Z^{(N)}$.

If we assume the following hierarchy of energy scales: $\mu_z^{(N)} - \mu_z^{(N-1)} \gg E_{\mathrm{so}} \gg \Delta \sim B$, it follows that given the critical field B_c, all bands with $n < N$, are automatically in the trivial phase, since $B^2 \ll \Delta^2 + (\mu - \mu_z^{(n<N)})^2$.

4.2.3 One-dimensional chiral fermions and quasiclassical approximation

We are interested in constructing a low-energy description of the system at energy scales $\lesssim E_{\mathrm{so}}$, and in order to draw on the techniques introduced in chapter 2, a Hamiltonian linear in momentum is imperative. Following our discussion of the emergence of Majorana fermions in quantum wires in section 3.3, we consider the eigenvalues of $\hat{H}_0^{(n)}$ (4.4). In the limit of strong spin-orbit coupling, $E_{\mathrm{so}} \gg B$, we recognise the reappearance of two shifted, intersecting parabolas in the spectrum of $\hat{H}_0^{(n)}$ (cf. our discussion in 3.3). The two Fermi momenta for each band are given by

$$k_n^c = \mp \alpha m + \sqrt{2m \left(\mu_z^{(N)} - \mu_z^{(n)} + E_{\mathrm{so}} \right)},$$

where we introduced the index $c \in \{a, b\}$. Aiming for a low-energy description, we introduce a set of chiral, (R) right and (L) left moving fermions and represent the field operators $\psi_\sigma^{(n)}$ in terms of a superposition of the latter ones, i.e.

$$\psi_\uparrow^{(n)} \simeq R_{a\uparrow}^{(n)}(x) \exp(ik_n^a x) + L_{b\uparrow}^{(n)}(x) \exp(-ik_n^b x),$$
$$\psi_\downarrow^{(n)} \simeq L_{a\downarrow}^{(n)}(x) \exp(-ik_n^a x) + R_{b\downarrow}^{(n)}(x) \exp(ik_n^b x).$$

The spectrum of the wire as well as the introduced chiral fermions are illustrated in figure 4.4. A conducting channel is defined by modes of the same modulus of the Fermi momentum

and is indicated by open and filled dots, respectively. Since each channel carries either index a or b, we henceforth refer to c as the channel index and it is the latter that defines the spin direction of the chiral fermion. In channel a for instance, right moving (R) fermions have spin up while the left moving (L) ones have spin down, for channel b it is reversed. Within the N-th band, the a-channel has a vanishing Fermi momentum $k_N^a = 0$ and a magnetic field would open a gap separating the two parabolas (indicated by the grey curves in fig. 4.4, cf. discussion in section 3.3). However, for strong spin-orbit coupling solely the a-channel is strongly effected by the magnetic field. As an immediate consequence, the phase of the wire is exclusively determined by this channel, and following our procedure of name-giving, we refer to this channel as *topological channel* and ignore the effects of the magnetic field on all other channels. Note however, that the effect of the pairing amplitude, appearing in the off-diagonal entries of the BdG-Hamiltonian, is far from being nugatory. The Hamiltonian eq. (4.6) can then be linearised around the Fermi momenta. Oscillatory contributions, i.e. terms with phases $i(\sum_{i=a,b} \pm k_i)x$, can be omitted since due to the large spin-orbit energy, the Fermi length $\lambda_F \sim \max(1/k_a, 1/k_b)$ is much bigger than the typical lengths involved ($\xi \sim \Delta/v$ and $l_B \sim B/\alpha$). The linearised Hamiltonian is conveniently represented in a basis with the spinors arranged as follows (leaving the band index (n) implicit)

$$\Psi = (R_{a\uparrow}, R_{b\downarrow}, L_{a\downarrow}, L_{b\uparrow}, \bar{R}_{a\uparrow}, \bar{R}_{b\downarrow}, \bar{L}_{a\downarrow}, \bar{L}_{b\uparrow})^{\mathrm{T}}, \tag{4.7}$$

and the conjugated vector is given by $\bar{\Psi} = (\sigma_x^{ph}\Psi)^{\mathrm{T}}$. Notice that due to the particle-hole symmetry, the introduction of two chiral fermions (R/L), two channels (a, b) and N bands, the spinor now acts in the $8 \times N$-dimensional product space. With the Fermi velocity (of the n-th channel) $v_n = \sqrt{2m(\mu_z^{(N)} - \mu_z^{(n)} + E_{\mathrm{SO}})}/m$ and the chemical potential defined relative to $\mu_z^{(N)}$, $\hat{H}_0^{(n)}$ is linearised to[4]

$$\hat{H}_0^{(n)} = -i\sigma_z^{RL} - \mu + (B/2)\sigma_0^{RL} \otimes (\sigma_0^{ab} + \sigma_z^{ab})\delta_{Nn}.$$

Note that the Kronecker delta δ_{Nn} takes into account that only the N-th channel is sensible to the magnetic field. In representation (4.7) the full linearised Hamiltonian is given by

$$\mathcal{H} = \frac{1}{2} \int \bar{\Psi}^{(n)}(x) \begin{pmatrix} \hat{H}_0^{(n)}\delta_{nm} + \hat{W}_{nm} & i\Delta\sigma_y^{RL} \otimes \sigma_z^{ab}\delta_{nm} \\ -i\Delta\sigma_y^{RL} \otimes \sigma_z^{ab}\delta_{nm} & -(\hat{H}_0^{(n)})^{\mathrm{T}}\delta_{nm} - \hat{W}_{mn}^{\mathrm{T}} \end{pmatrix}_{ph} \Psi^{(m)}(x)\mathrm{d}x. \tag{4.8}$$

---

[4]In the simplistic notation we use, trivial extensions of the operators are omitted whenever possible. Therefore, a solitary Pauli matrix σ_i appearing in a higher-dimensional expression has to be understood as $\sigma_i \otimes \sigma_{d-2}$, where d is the dimension the dimension of the expression.

Notice that the particle-hole symmetry of the first-quantised single particle Hamiltonian is defined by

$$\hat{H} = -U_c^{-1}\hat{H}^{\mathrm{T}}U_c, \tag{4.9}$$

i.e. $\hat{H}$ is pseudo-skew symmetric[5] with $U_c = \sigma_z^{ph}$.

4.2.4 Majorana representation

The Hamiltonian (4.8) is already linear in momentum, but for the quasiclassical description, it is more convenient if the symmetry eq. (4.9) is represented by a skew-symmetric Hamiltonian matrix

$$\hat{H}^{\mathrm{T}} = -\hat{H}.$$

We begin with defining a set of eight Majorana fields, which combined to a spinor will later replace our field operator Ψ,

$$\begin{aligned}
\xi_a^R &= (R_{a\uparrow} + \bar{R}_{a\uparrow})/\sqrt{2}, \\
\xi_b^R &= (R_{b\downarrow} + \bar{R}_{b\downarrow})/\sqrt{2}, \\
\eta_a^R &= (R_{a\uparrow} - \bar{R}_{a\uparrow})/\sqrt{2i}, \\
\eta_b^R &= (R_{b\downarrow} - \bar{R}_{b\downarrow})/\sqrt{2i}.
\end{aligned}$$

The corresponding fields for the left moving fermions are constructed analogously with reversed spins. The similarity to the Majorana operators defined in eq. (3.2) is of course not accidental and hence this representation is baptised *Majorana representation*. After arranging the Majorana fields into a spinor of dimension $8N$

$$\tilde{\chi} = (\xi_a^R, \xi_b^R, \xi_a^L, \xi_b^L, \eta_a^R, \eta_b^R, \eta_a^L, \eta_b^L)^{\mathrm{T}},$$

it relates to Ψ by a unitary transformation

$$\tilde{\chi} = U\Psi, \quad \tilde{\chi}^{\mathrm{T}} = \bar{\Psi}U^{\dagger},$$

where

$$U = \sigma_0^{ab} \otimes \sigma_0^{RL} \otimes \frac{1}{\sqrt{2}}\begin{pmatrix} 1 & 1 \\ i & -i \end{pmatrix}_{ph}. \tag{4.10}$$

---

[5]The kinetic part transposes as $\partial_x^{\mathrm{T}} = -\partial_x$.

In a last step we combine Majorana fields of same chirality, i.e. $\xi^C = (\xi_a^C, \xi_b^C)^{\mathrm{T}}$ and $\eta^C = (\eta_a^C, \eta_b^C)^{\mathrm{T}}$ with $C = R/L$, in order to rearrange them according to

$$\chi = (\xi^R, \eta^L, \eta^R, \xi^L)^{\mathrm{T}}. \tag{4.11}$$

The Hamiltonian (4.8) is then represented as follows

$$\mathcal{H} = \sum_{n,m=1}^{N} \frac{1}{2} \int \chi_n^{\mathrm{T}}(x) \tilde{\mathcal{H}}_{nm}(x) \chi_m(x) \mathrm{d}x,$$

with

$$\tilde{\mathcal{H}}_{nm}(x) = \begin{pmatrix} \hat{H}_-^{(n)}\delta_{nm} + i\hat{W}_{nm}^{--} & i\mu\sigma_z^{RL} \otimes \sigma_0^{ab}\delta_{nm} + i\hat{W}_{nm}^{-+} \\ -i\mu\sigma_z^{RL} \otimes \sigma_0^{ab}\delta_{nm} + i\hat{W}_{nm}^{+-} & \hat{H}_+^{(n)}\delta_{nm} + i\hat{W}_{nm}^{++} \end{pmatrix}, \tag{4.12}$$

where we defined

$$\hat{H}_\pm^{(n)} = -iv_n\sigma_z^{RL} \otimes \sigma_0^{ab}\partial_x - \sigma_y^{RL} \otimes \hat{\Delta}_\pm^{(n)},$$
$$\hat{\Delta}_\pm^{(n)} = \Delta\sigma_z^{ab} \pm (B/2)(\sigma_0^{ab} + \sigma_z^{ab})\delta_{Nm}.$$

Provided that the disorder potentials are constructed in a way[6] that $\hat{W}^{++}$ as well as $\hat{W}^{--}$ are skew-symmetric, while the off-diagonal entries are related by $(\hat{W}^{+-})^{\mathrm{T}} = -\hat{W}^{-+}$, the particle-hole symmetry is represented by the skew-symmetry $\tilde{\mathcal{H}}^{\mathrm{T}} = -\tilde{\mathcal{H}}$.

4.2.5 Disorder potential

We now specify the statistics of the disorder potential $\hat{W}$. $\hat{W}$ is chosen to be δ-correlated, Gaussian distributed with a zero mean value $\langle \hat{W}(x) \rangle$ and its explicit construction is given by

$$\hat{W}^{--} = \begin{pmatrix} \hat{w}_2^{RR} & -\hat{w}_1^{RL} \\ \hat{w}_1^{LR} & \hat{w}_2^{LL} \end{pmatrix}_{ab}, \quad \hat{W}^{-+} = \begin{pmatrix} -\hat{w}_1^{RR} & \hat{w}_2^{RL} \\ \hat{w}_2^{LR} & \hat{w}_1^{LL} \end{pmatrix}_{ab}.$$

The random matrices $\hat{W}^{RL}$ are constructed in terms of a real and imaginary part

$$\hat{W}^{CC} = \hat{w}_1^{CC} + i\hat{w}_2^{CC},$$

---

[6]Keep in mind that we introduced the disorder Hamiltonian in a way that it respects the symmetries of the system.

for $C \in \{R, L\}$ and $\hat{w}_{1,2}$ being a symmetric and a skew-symmetric matrix, respectively. The off-diagonal entries can then be constructed via the relations

$$\hat{W}^{+-} = -\sigma_z^{ab} \hat{W}^{-+} \sigma_z^{ab}, \quad \hat{W}^{++} = \sigma_z^{ab} \hat{W}^{--} \sigma_z^{ab}.$$

The variance of the disorder potential is

$$\langle w_z^{ij}(x) w_z^{i'j'}(x) \rangle = \frac{\gamma_W}{2} \delta(x - x') \left(\delta_{ii'} \delta_{jj'} + (-1)^{z+1} \delta_{ij'} \delta_{ji'} \right), \tag{4.13}$$

where $z = 1, 2$ and i, j label states in the product space of band, channel and chirality. Notice that by construction, these scattering matrices are breaking time-reversal and spin-rotation symmetry and therefore explicitly include spin-flip scattering. The coefficient γ_W, which defines the strength of the disorder, is correlated to the scattering rate of the normal conducting quantum wire by

$$\frac{1}{\tau} = 2\gamma_W^2 \sum_{n=1}^{N} \frac{1}{v_n}. \tag{4.14}$$

4.3 Quasiclassical approach to multi-channel quantum wires

The Hamiltonian (4.12) is linear in momentum and we are in a position to treat the model within quasiclassical framework introduced in chapter 2. In the latter we discussed that the terminology *quasiclassical approximation* in quasi one-dimensional geometries, as the ones discussed in this chapter, refers to the possibility to linearise the spectrum around the chemical potential. Note that the latter was possible due to the presence of the magnetic field in the coupling between left and right moving states for the topological channel (see discussion around eq. (4.8)), provided that $E_{\text{so}} \gg \max\{B, \Delta\}$. Once the model specific representation of the involved operators (such as U and Γ) have been identified, the technique can be applied straightforwardly. The familiar procedures thus include the calculation of the Eilenberger functions in the clean limit and the subsequent construction of the full Eilenberger function using transfer matrices. Following our strategy outlined in chapter 2, a topological invariant can be constructed using the symmetry relations of the Eilenberger function. By solving the full disordered Eilenberger equation numerically, a physical observable (the local density of states) can be calculated.

4.3.1 Eilenberger equation and Eilenberger function

The kinetic part of the already linearised Hamiltonian (4.12) was given by $\hat{H}_\pm^{(n)} \delta_{nm} + \sigma_y^{RL} \otimes \hat{\Delta}_\pm^{(n)}$, and thus if we comprise all remaining terms of the Hamiltonian in $\hat{m}$, the Hamiltonian

takes the form

$$\tilde{\mathcal{H}}_{nm}(x) = -iv_n\delta_{nm}\sigma_z^{RL} \otimes \sigma_0^{ab}\,\partial_x + \hat{m},$$

which resembles the Hamiltonian (2.4) with the identification

$$\Gamma = \sigma_z^{RL}.$$

Notice that the Majorana basis was constructed in a way that, the particle-hole symmetry is trivially represented by $U_C = \mathbb{1}$ and, according to eq. (2.10), $u_c = \sigma_3^{RL}$. The Green's function (2.5) takes the form

$$g_{nm}^{R/A}(x, x'; \epsilon) = \sqrt{v_n}G_{nm}^{R/A}(x, x'; \epsilon)\sigma_z^{RL}\sqrt{v_m},$$

where a band index is now present in G and the velocities v. The evolution operator follows directly from the definition eq. (2.6)

$$\mathcal{L}_\epsilon = -i\sigma_z^{RL}\left(\epsilon v_n^{-1}\delta_{nm} + \sqrt{v_n v_m}^{-1}\hat{m}_{nm}\right). \tag{4.15}$$

We start with the definition (2.8) and solve the isotropic Eilenberger eq. (2.9) for constant magnetic field and pairing amplitude, in an infinite clean wire. In this limit, the kinetic part as well as $\hat{m}$ are diagonal in channel-space and therefore all channels are completely decoupled, allowing us to single out the *topological channel* (channel a with band $n = N$). We concentrate on this particular channel, but the generalisation to the Eilenberger function of the remaining channels is easily constructed by rescaling the velocities, setting $B = 0$ and switching the overall sign of the pairing amplitude $\Delta \to -\Delta$ for the b-channels (cf. eq. (4.8)). If $\mathcal{Q}_\epsilon(B, \mu)$ is the corresponding reduced single-channel Eilenberger function (of dimension 4×4), and L_ϵ the reduced evolution operator, they have to commute $[\mathcal{Q}_\epsilon, L_\epsilon]_- = 0$ and $\mathcal{Q}_\epsilon$ has to obey the non-linear constraint $\mathcal{Q}_\epsilon^2 = \mathbb{1}$. The reduced version of eq. (4.15) is given by

$$L_\epsilon = -i\begin{pmatrix} \epsilon\sigma_z^{RL} - i\Delta_-\sigma_x^{RL} & -i\mu\sigma_0^{RL} \\ i\mu\sigma_0^{RL} & \epsilon\sigma_z^{RL} - i\Delta_+\sigma_x^{RL} \end{pmatrix},$$

and its eigenvalues are straightforwardly calculated

$$\lambda_\pm = \sqrt{\lambda_0 \pm \lambda}, \tag{4.16}$$

where

$$\lambda_0 = B^2 + \Delta^2 - \mu^2 - \epsilon^2,$$
$$\lambda = 2\sqrt{(B\Delta)^2 - (\Delta^2 - \epsilon^2)\mu^2}.$$

We introduce the eigenvalue matrix

$$\hat{\lambda} := \operatorname{diag}(\lambda_+, \lambda_-)$$

and assume that L_ϵ is diagonalised by a transformation T as follows

$$L_\epsilon = T(\hat{\lambda} \otimes \sigma_z^{RL})T^{-1}. \tag{4.17}$$

We have chosen the diagonalisation such that the real part of the eigenvalues is positive. For a detailed discussion we refer to chapter 2. This convention allows us to simply read off the signature matrix Λ, which is used to construct the Eilenberger function $\mathcal{Q}_\epsilon = T\Lambda T^{-1}$. Equation (4.17) thus tells us that $\Lambda = \sigma_z^{RL} = \Gamma$, $\mathcal{Q}_\epsilon$ satisfies the constraint $\mathcal{Q}_\epsilon^2 = \mathbb{1}$ and solves the isotropic Eilenberger equation $[\mathcal{Q}_\epsilon, L_\epsilon]_- = 0$.

   Given the solution of the homogeneous Eilenberger equation, we are in the position to define the topological invariant for the clean (terminal) system. To this end, we notice that particle-hole symmetry is represented by

$$\sigma_z^{RL}\mathcal{Q}_{-\epsilon}^{\mathrm{T}}(x)\sigma_z^{RL} = -\mathcal{Q}_\epsilon(x).$$

Consequently, at zero energy the object $\tilde{\mathcal{Q}}_{\epsilon=0} = \sigma_z^{RL}\mathcal{Q}_{\epsilon=0}$ is skew-symmetric. Skew-symmetry implies the existence of a Pfaffian and since[7]

$$\det \mathcal{Q} = \det \Lambda = 1 = \det \sigma_z^{RL} \det \Lambda = \det \tilde{\mathcal{Q}},$$

the Pfaffian (being the square-root of the determinant) of $\tilde{\mathcal{Q}}$ defines the desired $\mathbb{Z}_2$-invariant. Now consider the eigenvalues (4.16) at zero energy. The kernel of $L_{\epsilon=0}$ is only non-trivial if the magnetic field[8] B reaches a critical field strength $B_c = \sqrt{\Delta^2 + \mu^2}$. At this point, a Pfaffian cannot be defined since $\tilde{\mathcal{Q}}$ becomes singular, a fact to which we will return later. However, for $B \neq B_c$ we can construct the topological invariant

$$N = \operatorname{Pf}(\tilde{\mathcal{Q}}) = \frac{\lambda_+\lambda_-}{\Delta^2 + \mu^2 - B^2} = \begin{cases} +1, & B < B_c \\ -1, & B > B_c. \end{cases} \tag{4.18}$$

$N = +1$ thus indicates the topological trivial phase, while $N = -1$ indicates a non-trivial system. Hence, the topological phase of the terminal ($\tilde{\mathcal{Q}}_\pm$) is determined by eq. (4.18).

---

[7] *Mind the gap* in the sloppy notation, $\sigma_z^{RL} = \sigma_z^{RL} \otimes \mathbb{1}_2$ and thus $\det \sigma_z^{RL} = \det \sigma_z^{\,2}(\det \mathbb{1}_2)^2 = +1$

[8] It is important to mention that one could define an equivalent criteria for other system parameters, such as the chemical potential μ as it is done later in the text.

4.3.2 Density of states

The bulk density of states is defined in terms of the Eilenberger function $\mathcal{Q}_\epsilon$ as

$$\nu(\epsilon) = \frac{1}{2\pi v} \mathrm{Re}\, \mathrm{Tr}\, \sigma_z^{RL} \mathcal{Q}_\epsilon. \tag{4.19}$$

Notice that the upper expression depends on the product of $\Gamma \cdot \mathcal{Q}_\epsilon$ rather than just on $\mathcal{Q}_\epsilon$, which due to the invariance of trace would lead to homogeneous density of states. However, since $\nu(\epsilon)$ depends on the transformation matrices T, which are far from being trivial, we would like to make use of the invariance of the trace, in order to derive an expression that rather depends only on the evolution operator and its eigenvalues. To this end, we represent the Eilenberger function as[9]

$$\mathcal{Q}_\epsilon = \sum_{i=+,-} L_\epsilon / \lambda_i P^i, \tag{4.20}$$

where the projectors on the space of eigenstates of L_ϵ with eigenvalues $\pm\lambda_\pm$ are denoted by $P^\pm$. The latter are explicitly given by

$$P^\pm = \frac{1}{2} T \left(\mathbb{1}_2 \pm \sigma_z \right) \otimes \mathbb{1}_2 T^{-1},$$

and indeed we see that

$$T\mathcal{Q}_\epsilon T^{-1} = \frac{\hat{\lambda}}{2\lambda_+} \otimes \sigma_z^{RL} \cdot (\mathbb{1}_2 + \sigma_z) \otimes \mathbb{1}_2 + \frac{\hat{\lambda}}{2\lambda_-} \otimes \sigma_z^{RL} \cdot (\mathbb{1}_2 - \sigma_z) \otimes \mathbb{1}_2 = \mathbb{1}_2 \otimes \sigma_z^{RL} = \Lambda.$$

A T-independent representation of the projectors $P^\pm$ is achieved using that

$$L_\epsilon^2 = T(\hat{\lambda} \otimes \sigma_z^{RL})^2 T^{-1} = T \left(\mathrm{diag}(\lambda_+^2, \lambda_-^2) \otimes \mathbb{1}^{RL} \right) T^{-1}$$
$$= T \,\mathrm{diag}(\lambda_0 + \lambda, \lambda_0 - \lambda) T^{-1} = T\lambda_0 \mathbb{1}_4 T^{-1} + \lambda P^+ - \lambda P^-.$$

Hence the projectors are given by

$$P^\pm = \frac{1}{2} \left(\mathbb{1}_4 \pm \frac{1}{\lambda} (L_\epsilon^2 - \lambda_0 \mathbb{1}_4) \right),$$

and together with eq. (4.20) we arrive at a representation of $\mathcal{Q}$ that solely depends on L_ϵ and its eigenvalues. The clean density of states (4.19) can now be calculated straightforwardly.

Figure 4.5 illustrates the density of states profiles and spectra for different values of the chemical potential μ. The very definition of $\nu(\epsilon)$ shows that it is singular for vanishing

---

[9]In a way this step can be viewed as analogy to flattening of Hamiltonians described in section 1.3.
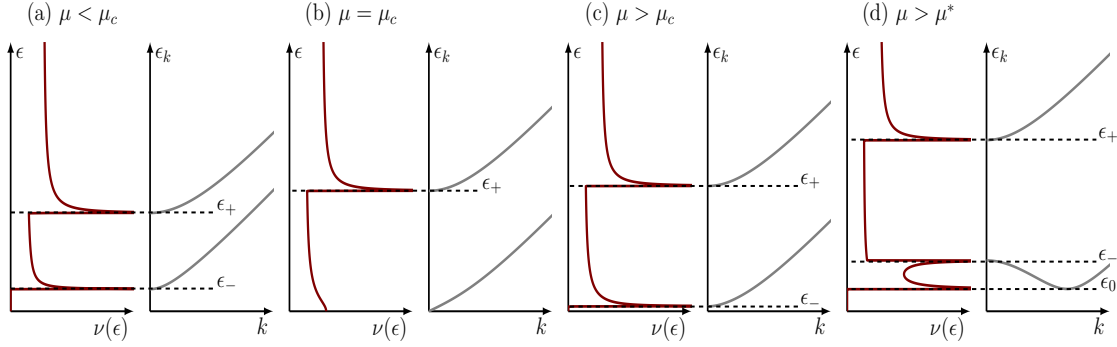
Figure 4.5: Spectrum and DoS profiles of the clean nanowire for various values of the chemical potential. The gap of the spectrum is open below the critical μ_c (a), is closed in at the critical point (b), and reopens in again beyond the critical point (c). For higher chemical potentials, the lower band develops two minima (d). Picture taken from [91].

eigenvalues $\lambda^{\pm}(\epsilon) = 0$ and the position (in energy) of this singularities are

$$\epsilon_{\pm} = |B \pm \sqrt{\Delta^2 + \mu^2}|.$$

At $B = B_c$, the lower singularity ϵ_- is located at zero-energy and the gap is closed.

In experiments, the chemical potential μ rather than the magnetic field B is used as tunable parameter. Fixing the magnetic field and pairing amplitude and assuming that $B > \Delta$, the critical point at which the gap closes translates to

$$\mu_c = \sqrt{B^2 - \Delta^2}.$$

Gap closing at $\mu = \mu_c$ is shown in fig. 4.5b, the two distinct phases can then be identified by $\mu < \mu_c$ (fig. 4.5a) or $\mu > \mu_c$ (fig. 4.5c). In the latter case the gap re-opens but with the system belonging to a different topological phase. Upon further increasing the chemical potential beyond

$$\mu_* = \sqrt{B^2 + B\sqrt{B^2 + 4\Delta^2}}/\sqrt{2},$$

the Fermi momentum k_a of the topological channel deviates from zero, resulting in an additional minimum in the spectrum and an additional van-Hove singularity in the density of states at

$$\epsilon_0 = \Delta\sqrt{1 - B^2/\mu^2},$$

as can be seen in fig. 4.5d.

4.3.3 Disordered case

Given the analytic solution for the clean system, we now solve the Eilenberger equation for a finite disordered wire. It is obvious that the solution will depend on the specific disorder realisation and a full analytic solution is out of hand. We will therefore make use of numerical computations in order to obtain observables averaged over many different realisations. The formal solution of the Eilenberger equation was already discussed in section 2.2.3 and we will draw on this results. We model the system by the prototypical setup shown in fig. 2.1 with two superconductors constituting the terminals at the end of the wire. The disorder scattering rate $\frac{1}{\tau} \sim N \gamma_W^2 \langle \frac{1}{v_n} \rangle$ is chosen in a way, that it does not exceed the energy gap, ϵ_- or ϵ_0 (depending on the value of μ) in the terminals, and we can therefore safely neglect the disorder in the terminals[10]. The symmetries of the evolution operator $\mathcal{L}$ as well as the transfer matrix M are given by eq. (2.18) and (2.19) with $\Gamma = u_C = \sigma_z^{RL}$. To connect the prototypical setup (fig. 2.1) to the experimental realisation (fig. 4.3), we replace the left superconducting terminal by a tunnel barrier and ignore effects like spin-flip scattering at the barrier, as well as inter-channel scattering. A glance at fig. 4.4 reveals that the chiral fermions at the tunnel barrier obey the following reflection conditions

$$R_{a\uparrow}(x_L) = \exp(i\phi) L_{b\uparrow}(x_L), \; R_{b\downarrow}(x_L) = \exp(i\phi) L_{a\downarrow}(x_L), \tag{4.21}$$

provided that the barrier conductance is vanishing, $g_T \ll 1$. In eq. (4.21) the reflected fields acquire an energy-depended phase ϕ, which at this point is undetermined. In the representation (4.7) these boundary conditions are equivalent to

$$(\mathbb{1} - R)\Psi(x_L) = 0, \quad \bar{\Psi}(x_L)(\mathbb{1} - R) = 0, \tag{4.22}$$

where the reflection matrix in particle-hole space is defined as

$$R = \mathrm{diag}(r, r^*)_{ph}$$

with

$$r = \begin{pmatrix} 0 & \exp(i\phi)\sigma_x^{RL} \\ \exp(-i\phi)\sigma_x^{RL} & 0 \end{pmatrix}.$$

Notice that the particle-hole symmetry in this representation ensures that $\bar{\Psi} = (\sigma_x^{ph}\Psi)^{\mathrm{T}}$ and $R^{\mathrm{T}} = \sigma_x^{ph} R \sigma_x^{ph}$. In order to translate the boundary conditions for the fields Ψ and $\bar{\Psi}$ to conditions on the Green's functions $g(x, x'; \epsilon)$ and ultimately on $\mathcal{Q}_\epsilon(x, x')$, we recall the definition of $g(x, x'; \epsilon)$, eq. (2.5). Together with the fact that $[\sigma_z^{RL}, r]_+ = 0$, it follows that

---

[10]Disorder due to the proximate superconductor can be ignored [85, 97].

eq. (4.22) translates to

$$(\mathbb{1} - R)(\mathbb{1} - \mathcal{Q}_L) = 0, \quad (\mathbb{1} + \mathcal{Q}_L)(\mathbb{1} + R) = 0.$$

For $R = -\mathcal{Q}_-$, the upper expression resembles the boundary conditions eq. (2.22). The matrix $\mathcal{Q}_-$ has yet to be transformed into the Majorana representation, which is straightforwardly done by conjugating $\mathcal{Q}_-$ with the matrix[11] $U \cdot (\mathbb{1} \otimes \sigma_+^{RL} + \sigma_x \otimes \sigma_-^{RL}) \otimes \mathbb{1}^{ab}$, with U taken from eq. (4.10). In the Majorana representation the Eilenberger function for the tunnel barrier $\mathcal{Q}_-$, thus reads

$$\mathcal{Q}_- = -(\sin(\phi)\sigma_z^{ph} + \cos(\phi)\sigma_x^{ph}) \otimes \sigma_x^{RL} \otimes \sigma_x^{ab}.$$

Normalisation is ensured since $R^2 = \mathcal{Q}_-^2 = \mathbb{1}$ and the boundary Eilenberger functions $\mathcal{Q}_L$ and $\mathcal{Q}_R$ can be obtained using eqs. (2.23).

Majorana number

Prior to the disordered case the topological quantum number N for the clean case (the terminal Eilenberger functions) was defined in eq. (4.18). For the tunnel barrier it follows[12]

$$\mathrm{Pf}(\sigma_z^{RL}\mathcal{Q}_-) = \mathrm{Pf}(i(\sin(\phi)\sigma_z^{ph} + \cos(\phi)\sigma_x^{ph}) \otimes \sigma_y^{RL} \otimes \sigma_x^{ab}) = +1,$$

and we conclude that the tunnel barrier is in the trivial phase. $\mathcal{Q}_+$ can be calculated following the scheme outlined in section 4.3.1 and the $\mathbb{Z}_2$-invariant of the wire (cf. our analysis in sec. 2.3.1) is given by

$$\mathcal{M} = \mathrm{Pf}(\sigma_z^{RL}\mathcal{Q}_+)\,\mathrm{Pf}(\sigma_z^{RL}Q_-), \tag{4.23}$$

i.e. the product of the invariants N for both terminal Eilenberger functions. A proof that in the case of $\mathcal{M} = -1$, the system hosts edge modes at zero-energy, identified as Majorana fermions, was given in sec. 2.3.1 and appendix A. The latter are localised in the disordered regime between the two terminals and for obvious reasons the invariant $\mathcal{M}$ is referred to as *Majorana number* [9].

4.3.4 Single-channel case

Before we proceed with the numerical computation of the Eilenberger function in class D, we use this opportunity to add yet another example to our collection of examples discussed in section 2.4. We construct the topological invariant for a system of class BDI. In case of a single channel, the multi-channel quantum wire of class D can be considered as a member

---

[11]The second matrix in this product represents the rearrangement in eq. (4.11).
[12]Notice that $\Gamma\mathcal{Q}_-$ opposite to $\mathcal{Q}_-$ is a skew-symmetric matrix.

of class BDI. Consider the Hamiltonian (4.12) in the Majorana representation. The clean single-channel version is given by

$$\tilde{\mathcal{H}}(x) = \begin{pmatrix} h_0^- & i\mu\sigma_z^{RL} \\ -i\mu\sigma_z^{RL} & h_0^+ \end{pmatrix},$$

where $h_0^\pm = -iv\partial_x\sigma_z^{RL} - \sigma_y^{RL}(\Delta \pm B)$. The Hamiltonian is skew-symmetric and anti-commutes with $U_S = \mathbb{1} \otimes \sigma_x^{RL}$ (recall BDI is a chiral classes). In order to transform the Hamiltonian into a block off-diagonal form, U_S is transformed to $\hat{U}_S = \sigma_z \otimes \mathbb{1}$ by virtue of the unitary transformation

$$R = \tfrac{1}{\sqrt{2}}\left(\mathbb{1} \otimes \begin{pmatrix} 1 & -i \\ 1 & i \end{pmatrix}\right) \cdot \begin{pmatrix} \Sigma_{11} & \Sigma_{21} \\ \Sigma_{12} & \Sigma_{22} \end{pmatrix},$$

where Σ_{ij} is a 2×2-matrix with only one non-vanishing entry at the ij-component, e.g. $\Sigma_{12} = \begin{pmatrix} 0 & 1 \\ 0 & 0 \end{pmatrix}$ and $\Sigma_{22} = \begin{pmatrix} 0 & 0 \\ 0 & 1 \end{pmatrix}$. The transformed Hamiltonian in this basis is given by

$$\hat{\mathcal{H}} = R^\dagger\tilde{\mathcal{H}}R = -\mu\sigma_y \otimes \sigma_y + \sigma_x \otimes (B\sigma_z - \Delta\mathbb{1}) - iv\partial_x\sigma_2 \otimes \mathbb{1}$$

and anti-commutes with $\hat{U}_S$. We immediately identify

$$\Gamma = \sigma_y \otimes \mathbb{1},$$
$$\hat{m} = -\mu\sigma_y \otimes \sigma_y + \sigma_x \otimes (B\sigma_z - \Delta\mathbb{1}).$$

The evolution operator at zero energy decomposes into block diagonal form

$$\mathcal{L}_0 = \text{diag}(\mathcal{L}_0^1, \mathcal{L}_0^2),$$

where the blocks are given by

$$\mathcal{L}_0^1 = \sigma_z B - \Delta\mathbb{1} - i\mu\sigma_y$$

and $\mathcal{L}_0^2 = -\sigma_z\mathcal{L}_0^1\sigma_z$.

The eigenvalues of the blocks are easily computed

$$\lambda_\pm^i = (-1)^{i+1}\Delta \mp \sqrt{B^2 - \mu^2},$$

where the index $i = 1, 2$ labels the blocks. Depending on whether the magnetic field B

exceeds the critical field $B_c \equiv \sqrt{\Delta^2 + \mu^2}$ or not, the signature matrix reads

$$\Lambda^i = \begin{cases} -\mathbb{1} \otimes \sigma_z, & B > B_c \\ \sigma_z \otimes \mathbb{1}, & B < B_c. \end{cases}$$

Since the topological invariant in class BDI is given in terms of traces of $\mathcal{Q}$, which is invariant under similarity transformations, there is no need to calculate the explicit form of $\mathcal{Q}$. The topological invariant for class BDI is then given by

$$\mathcal{M} = \tfrac{1}{2} \left(\operatorname{tr} \Lambda^i_+ - \operatorname{tr} \Lambda^i_- \right) = \begin{cases} 1, & \Lambda^i_- \neq \Lambda^i_+ \\ 0, & \Lambda^i_- = \Lambda^i_+, \end{cases}$$

as desired.

4.4 Numerical results and discussion

In this section we present the main results of this chapter. As an analytic solution of the disordered Eilenberger equation is out of question, we rely on an efficient numerical method to tackle the problem. The method used relies on the the fact that the disordered Eilenberger function can be obtained from the Eilenberger functions deep within the terminals (as solutions of the isotopic Eilenber equations), by evolving them using a transfer matrix. In order to calculate the disordered Eilenberger function $\mathcal{Q}(x)$, we apply the following scheme for a given disorder realisation:

  i. Construct the terminal Eilenberger function as solutions of the isotopic Eilenberger eq.

  ii. Compute the transfer matrix M by numerically solving the corresponding systems of linear first-order differential equations.

  iii. Compute the boundary (or interface) functions $\mathcal{Q}_R$ and $\mathcal{Q}_L$ by applying eq. (2.23).

  iv. Compute $\mathcal{Q}(x)$ by applying the transfer matrix $M(x, x_{R/L})$ to $\mathcal{Q}_{R/L}$.

Given $\mathcal{Q}(x)$, we find the local density of states (LDoS) $\nu_L(\epsilon) = (2\pi v)^{-1} \operatorname{Re} \operatorname{tr}(\sigma_z^{RL} \mathcal{Q}(x = x_L))$ at the left end of the wire, close to the tunnel barrier. The LDoS relates to the differential conductance of the system (measured in real experiments) by

$$\frac{\mathrm{d}I}{\mathrm{d}V} = \frac{e^2}{16\pi\hbar} g_T \int\limits_{-\infty}^{+\infty} \partial_\epsilon f_F(\epsilon - V) \frac{\nu_L(\epsilon)}{\nu} \mathrm{d}\epsilon,$$

where g_T is the tunnel conductance of the barrier, f_F is the Fermi distribution, ν is the DoS in the single chiral channel per unit length and the voltage V is applied to the left of the

normal lead (N in fig. 3.4). A possible Majorana peak in $\mathrm{d}I/\mathrm{d}V$ at $V = 0$ should thus be represented by a singularity in $\nu_L(\epsilon = 0)$.

4.4.1 Numerical realisation of boundary conditions and disorder potential

The tunnel barrier to the left of the system discussed in section 4.3.3, was considered to be in the limit of a high potential barrier, i.e. $\phi = \pi$. The topological invariant N_L for the left terminal is $N_L = +1$ and thus trivial. The topological phase of the right terminal (superconductor) however, is set by the parameters B, Δ and μ. According to eq. (4.23) the phase of the total system is then solely determined by the right superconducting terminal, i.e. it is non-trivial ($N_R = -1$) if $\mu > \mu_c$ and trivial ($N_R = +1$) for $\mu < \mu_c$.

The δ-correlated random potential introduced as an expansion in terms of eigenfunctions

$$\hat{W}(x) = \sum_{k=1}^{N_{max}} \sqrt{\frac{2}{l_x}} \sin\left(\frac{\pi x k}{l_x} + \frac{\pi k}{2}\right) \hat{W}_k,$$

vanishing at the ends of the scattering region. The matrix elements $(w^{ij}_{m=1,2})_k$ of $\hat{W}_k$ were taken from a Gaussian distribution with variance γ_W (cf. eq. (4.14)) and correlators as described[13] in eq. (4.13). In practice a maximum of $N_{max} = 10$ harmonics proved to be sufficient.

4.4.2 Disorder averaged local density of states

The numerically calculated LDoS for the disordered wire is by nature a random quantity, hence it exhibits mesoscopic fluctuations and a disordered averaged quantity is desired. Figure 4.6 shows such an averaged LDoS $\langle \nu_L(\epsilon) \rangle$ as a function of energy, averaged over approximatively 500 realisations of disorder configurations. The density of states were numerically calculated following the procedure outlined above. The figure shows the averaged LDoS at the left tunnel barrier for two sets of data, corresponding to both possible phases, i.e. Majorana number $\mathcal{M} = \pm 1$. The red solid curve corresponds to the topological non-trivial case, i.e. a situation with a Majorana bound state, while the green dashed curve corresponds to the trivial case without such a state. Remarkably, in both situations the density of states shows a zero-energy peak.

To understand this results, we consider the normal region between the tunnel barrier and the superconductor, to form an effective *quantum dot* hosting random quasi-particle subgap energy states. These Andreev bound states of different transport channels will hybridise in the presence of a moderate amount of disorder. Since only particle-hole symmetry is present, the chaotic Andreev quantum dot belongs to either class B or D, depending on the parity of

---

[13] Note that eq. (4.13) is given in real space, hence the delta distribution $\delta(x - x')$ needs to be replaced by the Kronecker delta $\delta_{kk'}$.
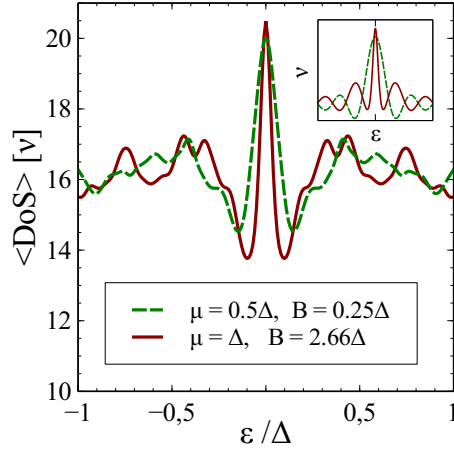
Figure 4.6: Disorder averaged local density of states (LDoS) at the left end of the spin-orbit quantum wire illustrated in fig. 4.3 (in units $\nu = 1/2\pi v$). The number of occupied bands $N = 2$ corresponds to four transport channels. Parameters are: (i) red solid line ($\mathcal{M} = -1$), $B = 2.66\Delta$, $\mu = \Delta$ — topological phase; (ii) green dashed line ($\mathcal{M} = +1$), $B = 0.25\Delta$, $\mu = 0.5\Delta$ — trivial phase. The wire length is $L = 4v/\Delta$, dimensionless strength of disorder $\gamma_w^2/v = 0.16\Delta$, which translates into the mean free path $l = 0.4L$. Tunnelling rate $\Gamma = 5 \cdot 10^{-2}\Delta$. Velocities in two bands were taken to be equivalent, $v_1 = v_2 = v$. The inset shows profiles of the DoS resulting from random matrix theory. Picture taken from [91].

the total number of subgap levels (counted for both, quasi-particle and quasi-hole states). Class B (an odd number of channels in our discussion in section 4.1) thus corresponds to the topologically non-trivial phase, i.e. $B > B_c$ for the topological channel.[14] While for $B < B_c$ in the topological channel, the system belongs to symmetry class D. In random matrix systems of class D the repulsion between quasi-particle and quasi-hole energy levels is absent and energy states cluster around zero-energy, [4]. Consequently will the averaged density of states develop a spectral peak which is rigidly tied to zero energy (fig. 4.1). This spectral peak is clearly present in the results shown in fig. 4.6. As the magnetic field B is varied, Andreev bound states emerge and abscond from the quasi-particle spectrum. However, at the critical field B_c the two lowest Andreev levels (conjugated pairs) merge into a single state, the Majorana bound state (compare fig. 3.1). Notice that this implies a change in level parity from even to odd. The insets in fig. 4.6 illustrates the DoS profile for class B and D (cf. fig 4.2) resulting from random matrix theory.

Figure 4.7 shows the three-dimensional averaged density of states profile of the wire. At the left end (x_L) the wire is connected to the tunnel barrier and the density of states signalises

---

[14]This identification follows from the fact, that we keep the number of channels fix and the topological channel solely determines whether the entire system is trivial or not.

a peak in both cases, the trivial and the non-trivial one, respectively. In agreement with the above discussion.

The numerical method used solves the Eilenberger equation for an energy that is shifted into the complex plane, $\epsilon \to \epsilon + i\eta$. The imaginary off-set η is due to the possibility for states in the scattering region to escape to the states in the lead through the tunnel barrier. The decay rate can be estimated as $\eta \sim g_T \delta$, where $\delta \sim \frac{\pi v}{2NL}$ is the mean level spacing in the scattering region of length L. It is for this off-set, that the Majorana peak ($\mathcal{M} = -1$) in fig. 4.6 acquires a finite width $\sim \eta$. For resolutions limited to the values of order of the mean level spacing δ, both structures in fig 4.6 look almost indistinguishable and may therefore hinder an unambiguous detection of a Majorana fermion by tunnel spectroscopy.

4.4.3 Sample-to-sample fluctuations

One of the most important features of random matrices is the repulsion of neighbouring eigenvalues (for uncorrelated levels). It is this repulsion of levels that leads to the rigidity of random matrix spectra. This rigidity manifests itself in weak sample to sample fluctuations[15]. Figure 4.8 shows the comparison of the averaged LDoS to the *typical* LDoS, i.e. the average $\sqrt{\langle v_L^2 \rangle}$. The strength of mesoscopic fluctuations is determined by the standard deviation

$$\delta\nu(\epsilon) = \langle (\nu(\epsilon) - \langle \nu(\epsilon) \rangle)^2 \rangle^{1/2},$$

and, as illustrated in fig. 4.8a, is relatively small, indicating the weakness of fluctuations. Consequently we expect the sample specific LDoS to show the same anomaly as the averaged quantity or put differently, the appearance of a disorder peak depends on the realisation.

Two realisations for the non-topological regime are shown in fig. 4.8b, no averages were taken and no Majorana state is present. The figure shows two possible scenarios: In the first (corresponding to the green dashed curve in fig. 4.8), the two lowest Andreev states ($\pm\epsilon_{min}$) are clearly separated and no zero-energy peak is visible. In the second scenario, these two states lie very close to the Fermi level and the energy difference does not exceed the broadening η, i.e. $\epsilon_{min} < \eta$. In this case the DoS will show a single peak indistinguishable from the anomaly due to the Majorana fermion.

4.4.4 Dependence on the magnetic field

In ref. [12] the dependence of the alleged Majorana peak on the magnetic field B was investigated in order to underline its topological nature. To this end, it was argued that the vanishing of the latter at zero-magnetic field as well as for a rotation of the field out of the plane, would substantiate the claim. However, we will now see that relatively simple arguments lead to the conclusion that such rotations of the magnetic field do not serve as an unambiguous evidence towards the topological nature of the peak.

---

[15]More precise the variance of the number of eigenvalues in an interval grows logarithmically with its length.
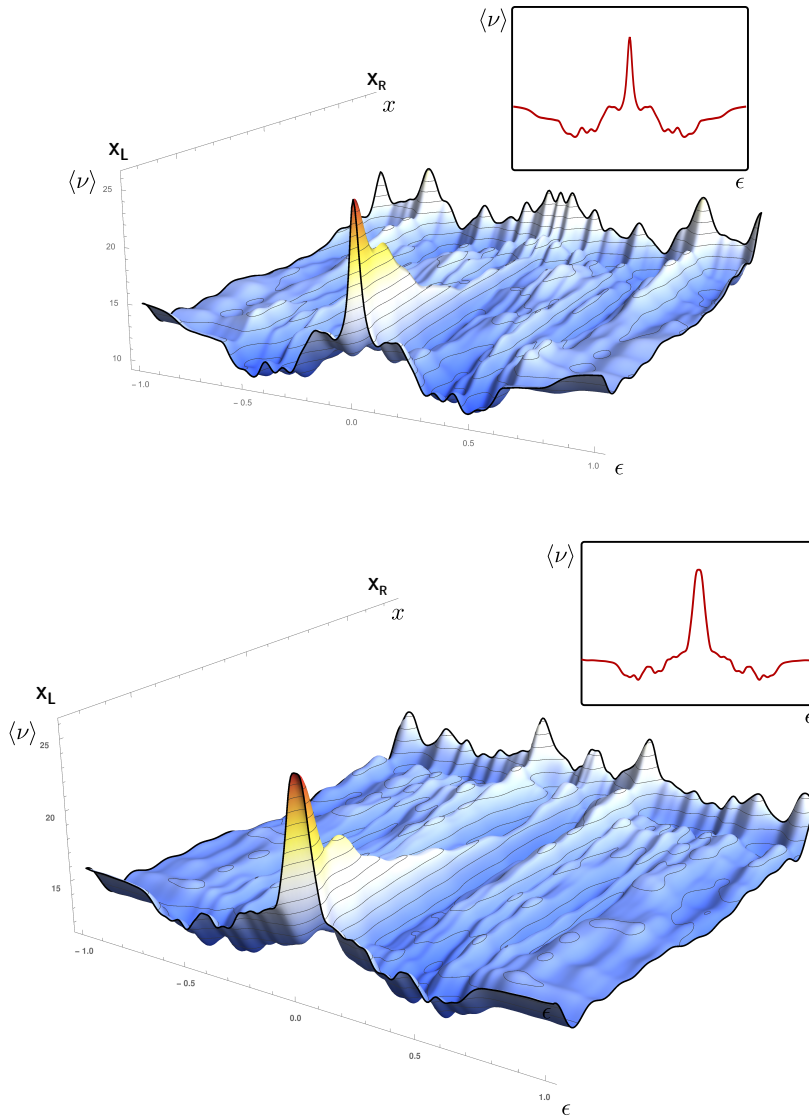
Figure 4.7: Averaged local density of states (averaged over approx. 100 samples) as a function of energy and coordinate for the system illustrated in fig. 4.3. The insets show cuts through the plot at the interface to the left end. Top: Topologically non-trivial. Bottom: Topologically trivial phase. Parameters as in fig. 4.6.

First we consider what happens in the case of vanishing magnetic field. Without an applied field the time-reversal symmetry is restored (the spinless regime is lost) and the wire migrates
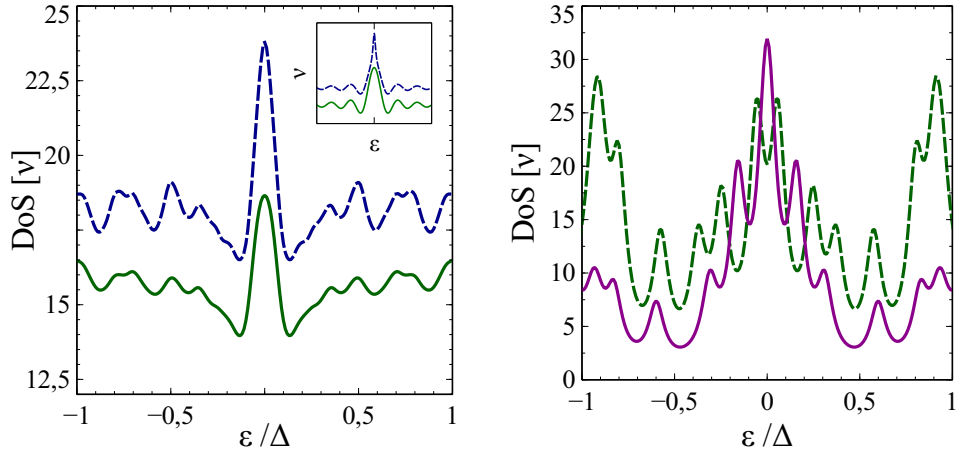
Figure 4.8: Left: The average LDoS (solid green line) and the square root of its second (reducible) moment $\langle \nu_L^2(\epsilon) \rangle^{1/2}$ (dashed blue line) at the left end of the spin-orbit quantum wire in the trivial phase ($\mathcal{M} = +1$). System parameters are chosen as in fig. 4.6. The inset shows profiles of the mean DoS and the square root of the two level correlation function resulting from random matrix theory. Right: The sample specific LDoS in the trivial phase without Majorana state ($\mathcal{M} = +1$) for two different disorder realisations. Tunnelling rate $\Gamma = 0.05\Delta$, other system parameters are the same as in fig. 4.6. Curves demonstrate two typical scenarios: (i) two conjugate Andreev bound states $\pm\epsilon_{\min}$ lying close to Fermi energy and having energy splitting $\sim \Gamma$ (dotted green line); (ii) particle and hole states have merged into a single zero-energy peak of width Γ and can not be resolved by tunnel spectroscopy (solid magenta line). For the chosen set of parameters the mean level spacing $\delta = 0.2\Delta$ and the gap in the S region $\epsilon_- = 0.87\Delta$. Thus one has approximately $N_{\mathrm{levels}} \simeq 8$ random Andreev levels. Picture taken from [91].

to class DIII. The averaged density of states for class DIII is given by [93]

$$\nu_{\mathrm{DIII}}(\epsilon) = \pi/2\epsilon \left(J_1'(\epsilon)J_0(\epsilon) + J_1^2(\epsilon) \right) \pm \pi/2J_1(\epsilon) - (1 - (-1)^N)/2\delta(\epsilon/2\pi),$$

where the dimension of the Hamiltonian is $2N \times 2N$ and $J_n(\epsilon)$ are the Bessel functions of first kind. The minimal dimension of the Hamiltonian describing our quantum wire is 4×4 and N turns out to be always even. Therefore the density of states (shown in fig. 4.9) vanishes at zero energy and no peak structure will be present, neither spectral nor Majorana peak.

The effect of rotating the magnetic field perpendicular to the wire, i.e. in z-direction, is similar. Consider the Hamiltonian (4.2), rotating the magnetic field perpendicular to the wire axis would result in the replacement of σ_x^{sp} by σ_z^{sp}. The spin-orbit contribution eq. (4.3) can
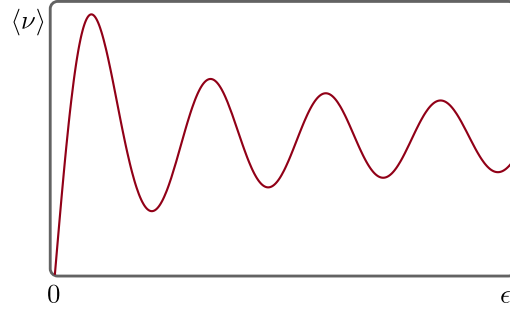
Figure 4.9: Averaged density of states $\langle \nu \rangle$ for class DIII as a function of energy with $N \in 2\mathbb{N}$. No zero-energy anomaly is present.

be neglected for a thin wire, $l_z \ll l_{\text{so}}$ and the BdG Hamiltonian $\mathcal{H}$ (4.1) is thus invariant under rotations about the z-axis, i.e. $[\mathcal{H}, \sigma_z^{ph} \otimes \sigma_z^{sp}]_- = 0$. A subsequent reordering of the spinor fields $\Psi \mapsto (\psi_\uparrow, \bar{\psi}_\downarrow, \bar{\psi}_\uparrow, \psi_\downarrow)$, decomposes the BdG Hamiltonian into two blocks (up to a trivial term) of the form $\mathcal{H}^{\#} = -\sigma_z((\sum_i \partial_i^2)/2m + \mu + i\alpha\partial_x) + B + \Delta\sigma_x$. The latter clearly belong to class A (no symmetry restrictions). As a member of the classical Wigner-Dyson classes, the density of states is flat showing no oscillations at all. And indeed, according to table 1.2 the system is a trivial insulator in one dimension, hosting no Marihuana particles.

We thus conclude that a proof for the topological origin of a Majorana fermions depending on the direction of the magnetic field, is not very reliable.

4.4.5 Mean free path and number of subgap states

The scattering rate is given by eq. (4.14) and since all quantities are expressed for uniform band velocities $(v_n = v = 1)$ the mean free path is given by $l = 1/2N\gamma_W^2$. For our numerical calculation a disorder strength $\gamma_W^2 = 0.16\Delta$ was chosen and accordingly the mean free path $l \simeq 0.4L$ is of the order of the length of the two-channel wire, $L = 4v/\Delta$. Thus the system underlying the numerical data in fig. 4.6 is at the border between a ballistic and localised regime[16]. However, despite being produced for a wire whose spectrum is not entirely chaotic, the similarities between the DoS profiles shown in fig. 4.6 and the averaged analytic DoS profiles from random matrix theory for class D and B shown in fig. 4.1, are eminent. It seems that close to the left barrier, the subgap states do indeed form an effective chaotic quantum dot as described earlier. As an additional cross-check we can check the number of subgap Andreev levels that constitute the dot. To this end we recall that the BCS gap $\epsilon_- = |B - \sqrt{\Delta^2 + \mu^2}|$ confines the subgap and thus inhabits approximately $N_{\text{subgap}} \simeq 2\epsilon_-/\delta$ Andreev levels, where the mean level spacing was given by $\delta \sim \frac{\pi v}{2NL}$. Now consider fig. 4.8b, with the chosen parameters the mean level spacing is $\delta = 0.2\Delta$ and the BCS gap is $\epsilon_- = 0.8\Delta$, resulting in approximately $N_{\text{subgap}} \simeq 8$ Andreev levels. The latter

---

[16]Notice that due to the relatively few number of channels, no true diffusive regime is present.

are easily confirmed by simply counting the peaks in fig. 4.8b in the interval $(-\epsilon_-, +\epsilon_-)$. Note that for the plot with the broadening exceeding the minimal energy spacing (magenta curve), the central peak has to be considered with a multiplicity of two.

4.5 Summary

In conclusion, we have studied disordered multi-channel Majorana wires using the quasiclassical approximation introduced in the second chapter of this work. The topological $\mathbb{Z}_2$ invariant of class D was explicitly derived using the terminal Green's functions. Since one of them is a trivial tunnelling barrier, the invariant solely depends on the phase of the proximity coupled superconductor terminal. The claimed experimental observation of Majorana fermions [12] at the end of such wires was been questioned. Using an efficient numerical method, based on the quasiclassical description, we proved that even small amounts of disorder (which are unavoidable) in the quantum wires, will lead to a deceiving signature (called class D spectral peak) in the spectrum, sharing key features with signatures of a Majorana fermion [91]. This signature is due to clustering of energy states around zero energy and is present in the topologically trivial regime. It is shown that this disorder induced spectral peak may aggravate an unambiguous detection of the Majorana fermion by tunnelling spectroscopy techniques, confirming the scepticism expressed in ref. [19]. In passing we note that similar conclusions have been reached in ref. [20, 21]. The latter of both references bases its conclusion on the weak anti-localisation effects, which however relies on the same physical mechanism, i.e. strong midgap quantum coherence.

A detection scheme involving the investigation of topological properties of the Majorana fermion, rather one that is purely based on spectral properties therefore remains highly desirable [82, 84, 98].

4.6 Disorder induced domain walls in quantum wires at criticality

In this section, we present an ongoing study on quantum wires at criticality. The results we present are preliminary and further investigations remain to be done. We discuss the influence of disorder on a class D quantum wire at criticality and address the question, whether disorder fluctuations lead to the emergence of local domain walls, separating large regions of different topological phases. At the transition separating the two phases, edge modes are expected to appear. Such disorder induced domain walls may hint towards the stabilisation of topological phases within the system. Possible approaches on how to distinguish robust topological excitations from local disorder-induced midgap sates, will be addressed as well. Throughout this section we make use of the numerical method introduced in the previous section. In ref. [99] the formation of such domain walls separating large regions in two different phases was studied using a renormalisation group approach. The observed non-universal contributions to certain low-energy properties indicated that such effects exist in

one-dimensional disordered superconductors.

As a warm-up, we start with a disorder-free toy model of the class D setup, as illustrated in fig. 2.1. We choose both terminals to be equivalent with constant system parameters B, Δ and μ throughout the whole system. In the absence of disorder, an analytic solution for $\mu = 0$ is at hand. To study the effects of disorder, we introduce domain walls *by hand* in the system. Such domains are created by modulating the profile of one parameter, say $\Delta = \Delta(x)$, as function of space. If these modulations locally change the phase of the system, e.g. changing from $\Delta < B$ to $\Delta > B$, we expect to find edge states at the boundaries. However, since the wire is finite, the support of the domains is limited. For short distances between two domain walls, the edge modes will be strongly hybridised, and split in energy (c.f. sec. 3.2.3). The splitting decreases exponentially with wire length (or distance) as it is illustrated in fig. 4.10. Figure 4.11 shows the local density of states as a function of energy, as well as space and the
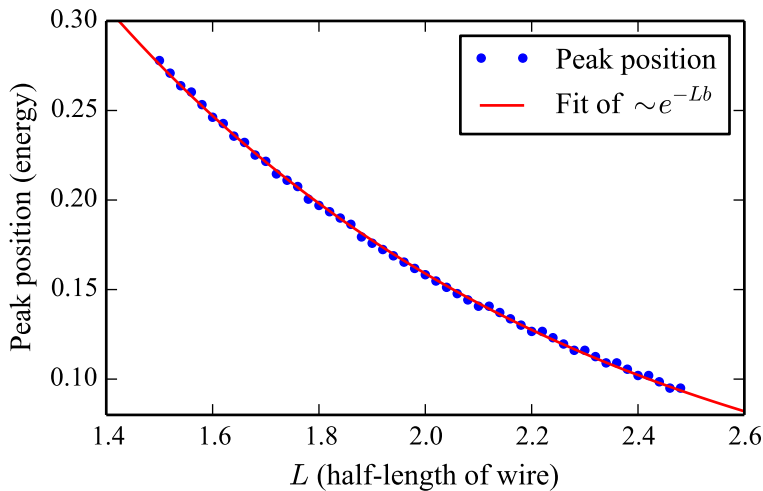
Figure 4.10: The splitting (in energy) of an edge mode is determined by the distance of the two split peaks. The splitting decreases exponentially with the wire length. Note that L denotes half of the wire length and the factor $b > 0$ is a fitting parameter.

corresponding profile of parameters. For simplicity we only show the left half of the wire. As expected, with increasing domain length (or decreasing distances) the states split in energy and hybridise with the partner states in the second half of the wire (not shown in the plots). The normalised spectral weight, i.e. the integral of energy and space of each peak is of the order of unity. Figures 4.12 and 4.13 show the density of states for a parameter profile which contains several domains of varying sizes. As in the previous discussion, the effects of splitting and hybridisation are visible. We therefore expect that short topological domains, introduced by disorder fluctuations, will not lead to (almost) zero-energy edge modes but to widely separated (in energy) pairs. Let us now reintroduce a finite chemical potential and

tune the system to criticality ($\mu = \mu_c$). In addition, we introduce disorder fluctuations in the chemical potential. Upon removing all artificial domains, the system is again effectively open since the system parameters are chosen to be homogeneous in the whole wire. Sufficient disorder fluctuations can locally drive the system from criticality to class B. Now if due to the disorder fluctuation the system becomes non-trivial over a sufficiently large region, there should be Majorana end states well localised at zero-energy. To investigate the possible emergence of such peaks, we study the evolution of a disorder configuration. To this end, two disorder realisations w_1 and w_1 are coupled by a system parameter r, according to $w_1 \cos r + w_2 \sin r$. For each r-step, the density of states as a function of space and energy is then calculated using the method introduced in sec. 4.4. Upon changing r, a plethora of peaks in the density of states will emerge and disappear, raising the natural question, how a Majorana peak is distinguished from a disorder-induced midgap peak. Such a midgap peak will be present, if two Andreev bound states are localised very close to zero energy and the resolution exceeds their distance. Indeed, such effects can be observed very frequently within the numerical simulations and these peaks can be excluded right away. In fig. 4.15 we illustrate the density of states landscape for a few consecutive steps. The fusion of peaks is clearly visible. There are however, very rarely peaks that seemingly emerge around zero-energy without any influence of surrounding peaks. These peaks are natural candidates for possible Majorana states, they are however hard to observe. Fig. 4.16 shows a sequence in which such a emergence without a visible fusion occurs. The task of identifying Majorana bound states turns out to be very delicate. Since the topological excitations are expected to be very robust, one possible criteria could be the stability of such peaks over a large range of r. In fig. 4.14a two peaks located at the end of the wire are shown, which remain unchanged over a large range of values of r. Figure 4.14b shows how the density of states evolves with r at a fixed position, which is given by the right peak in fig. 4.14a. We note that over a range from $r \sim 200$ to $r \sim 300$ these peaks (here only the right one is shown) are present before vanishing without a trace of splitting (green oval). A similar very sharp peak returns to this position for $r \sim 350$ to $r \sim 450$ (red oval). Since no obvious trace of a prior fusion of close lying Andreev bound states is present, these peaks might be considered as promising candidates for actual Majorana fermions. Note that there is an artefact at $r \sim 150$ which suggest a splitting of the peak. However, this artefact is very sharp and shows no traces of close lying Andreev states either. We therefore believe, that this splitting (or fusion) is due to the growth of the local domain(s). The latter reduces the splitting and two well localised states appear. In fig. 4.17 we see the signatures of a splitting (or fusion if the direction of r is reversed) of a peak into two close lying Andreev states (green ovals). Figure 4.18 illustrates however, that the traces of a splitting can be very hard to identify. Although a sharp peak is visible at $r \sim 200$, it seems to split very diffusively at $r \sim 280$. An additional cross-check that could be used to distinguish trivial and non-trivial peaks, is the investigation of the spectral weight. If the total weight of such a peak in the wire is denoted by 2δ, each Andreev state should contribute with δ. Consequently, the fused midgap state is expected to be of the order of 2δ. A single Majorana particles, with its partner somewhere far within the

system, contribution would be of order of δ. If a Majorana particle is split, each peak should thus have a spectral weight of the order of $\delta/2$. Although such calculations were performed for several candidates of Majorana fermions and Andreev bound states, the results remain inconclusive. The main reason being, that a clear identification of each peaks support, proves to be non-trivial.

We therefore conclude, that given the preliminary results presented above, within the numerical framework developed in sec. 4.4 it is possible to identify local domains of topologically distinct phases, stabilised by disorder fluctuations. The sharp nature of the observed peaks and their robustness over large ranges of r, suggests that we indeed observe Majorana bound states at the transition of such domains. The unambiguous identifications of the latter remains an open problem for future research.

———————————————————————————
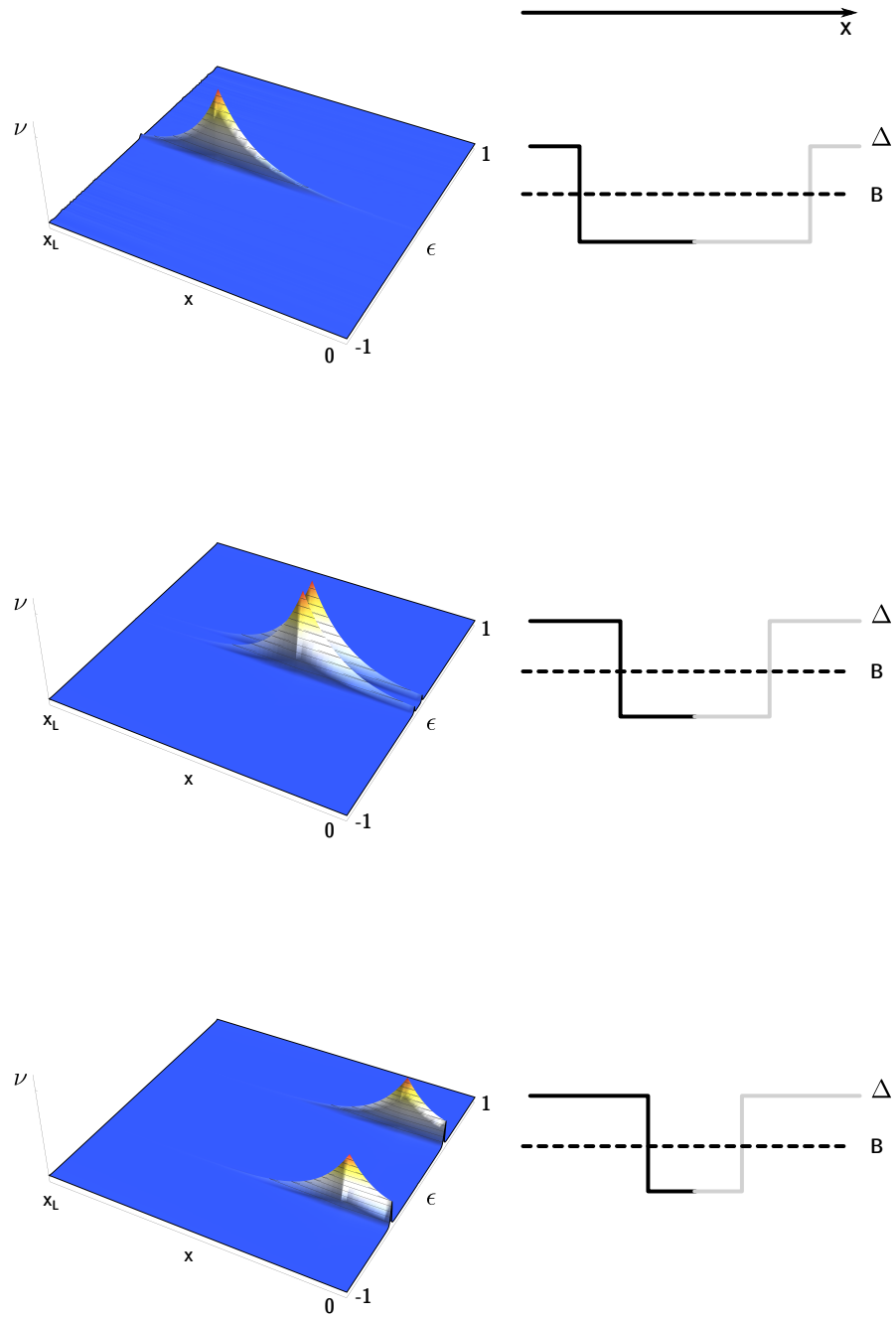
Figure 4.11: Density of states as a function of energy and position for the clean system (left). The corresponding parameter profiles shown are to the right. The left picture shows only one half of the system since it is symmetric (indicated by the black and grey profiles).
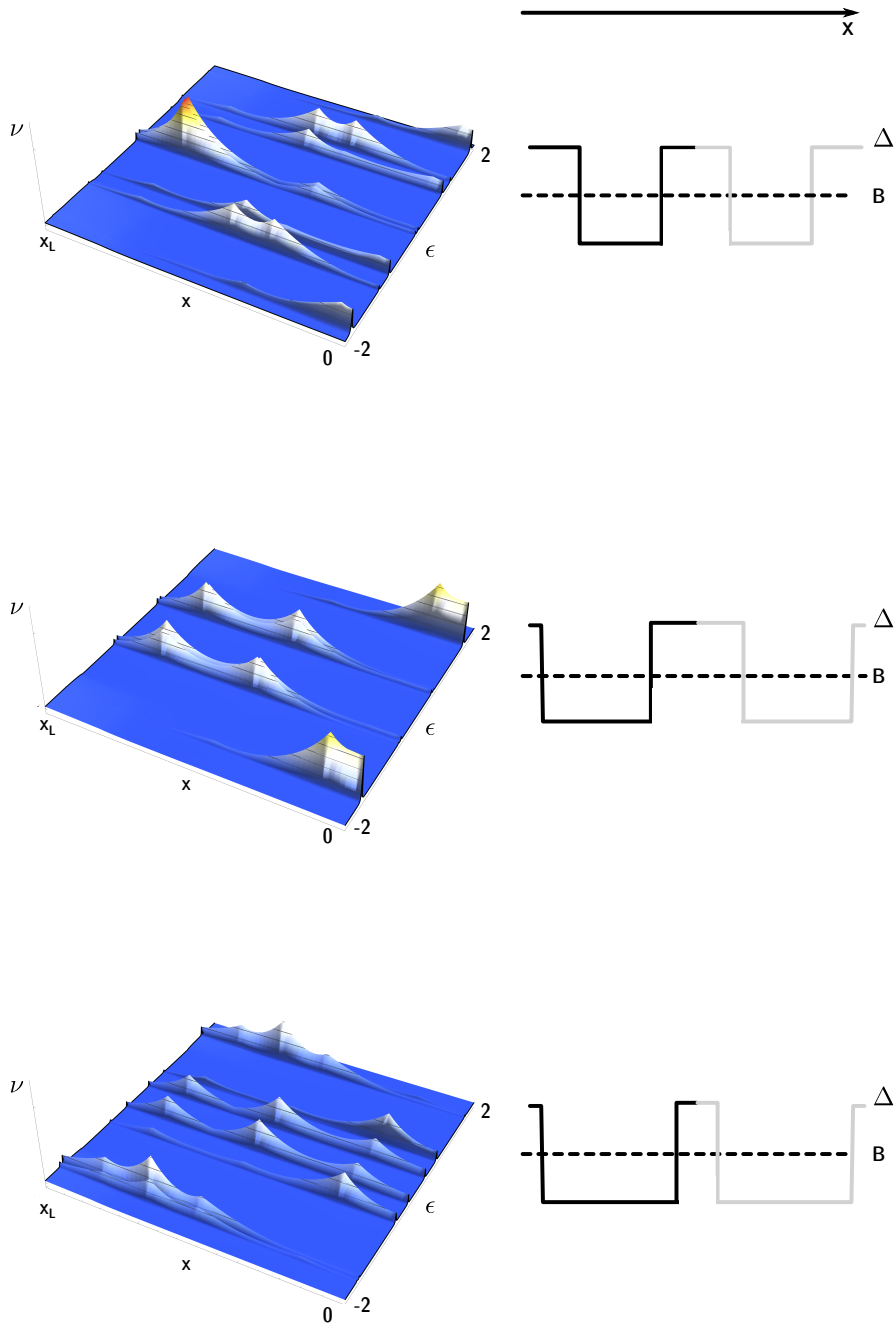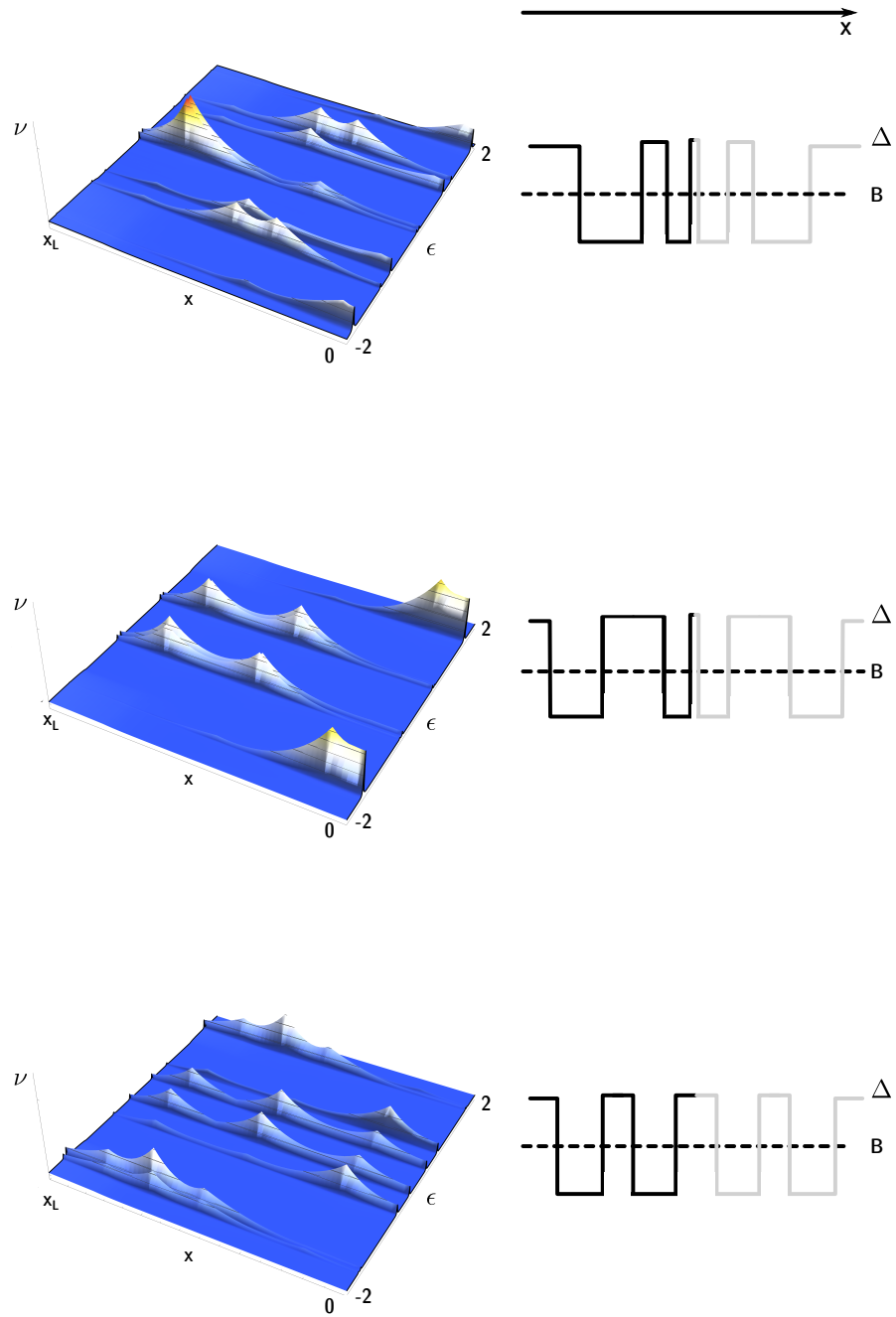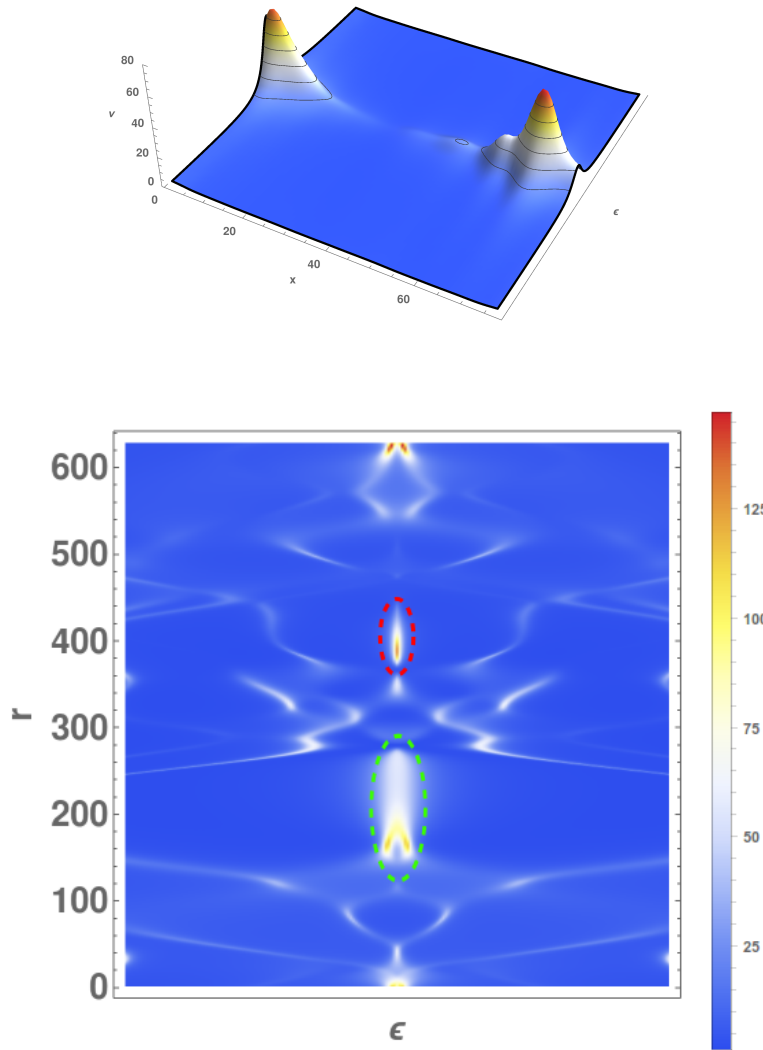
Figure 4.12: Density of states as a function of energy and position for the clean system (left). The corresponding parameter profiles shown are to the right. The left picture shows only one half of the system since it is symmetric (indicated by the black and grey profiles).

117

Figure 4.13: Density of states as a function of energy and position for the clean system (left). The corresponding parameter profiles shown are to the right. The left picture shows only one half of the system since it is symmetric (indicated by the black and grey profiles).

Figure 4.14: Top: Density of states as a function of energy and position in the wire. Two well localised peaks at $x \sim 0$ and $x \sim 70$ are visible. Both peaks remain unchanged for a large range of r values, before disappearing without splitting. Bottom: The density of states at the position of the right peak, as a function of energy and parameter r. The peak stays for a large range of r values (green oval). The Y-shaped structure at $r \sim 150$ indicates that if the length of the domains (or their distance) is insufficiently long, splitting occurs. Notice the sharp peak appearing without prior fusion at $r \sim 400$ (red oval).
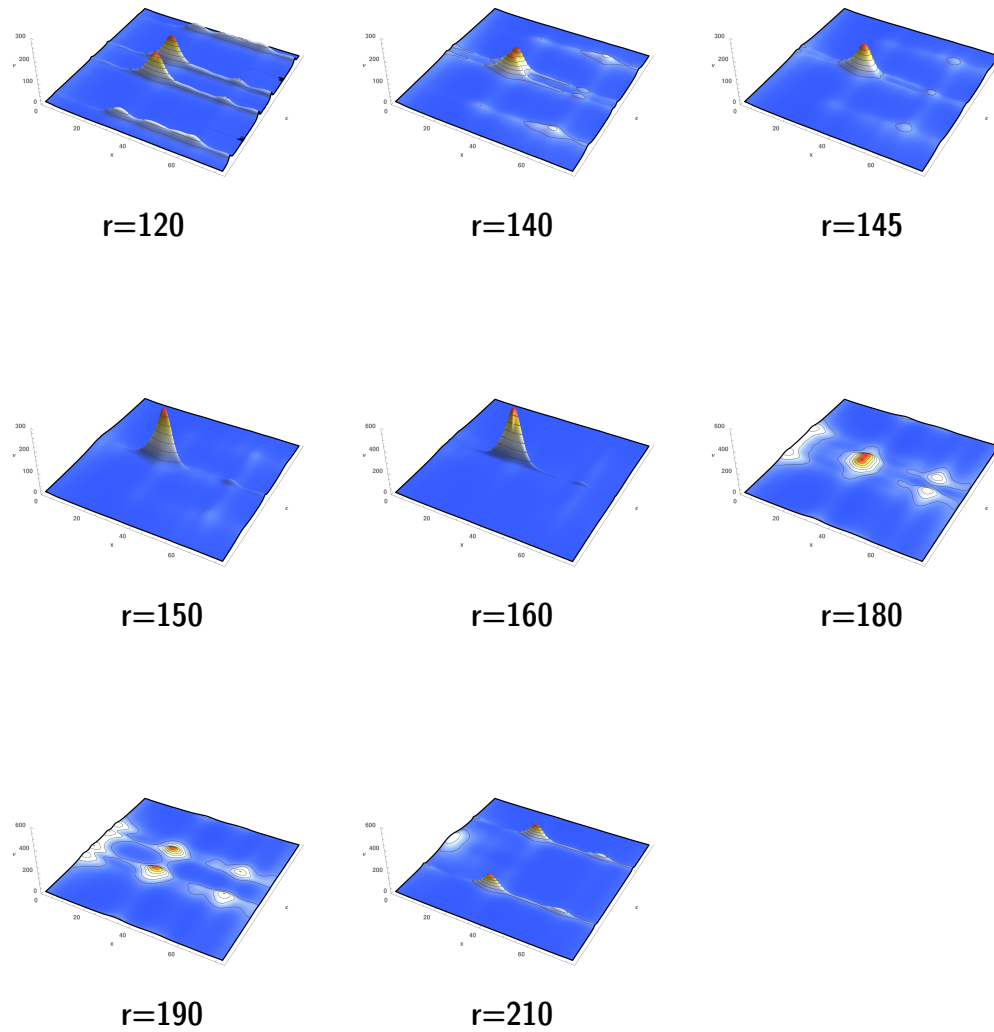
Figure 4.15: A sequence of the density of states as a function of energy and position in the wire is shown. At $x \sim 30$ two close lying Andreev peaks merge into a single peak (at $r = 145$) which eventually splits up again at $r = 190$.
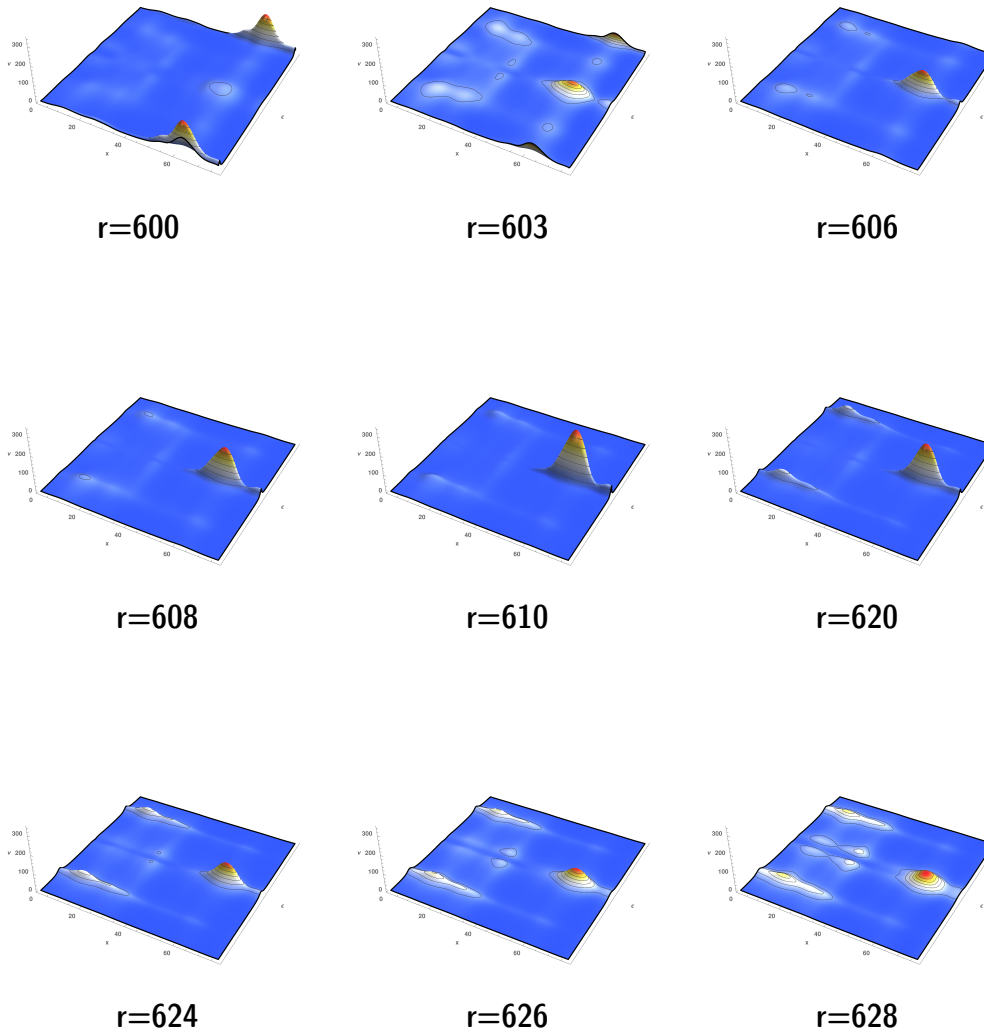
r=600 **r=603** **r=606**

r=608 **r=610** **r=620**

r=624 **r=626** **r=628**

Figure 4.16: A sequence of the density of states as a function of energy and position in the wire is shown. At $r \sim 60$ a zero-energy mode emerges from the spectrum without prior fusion of peaks.
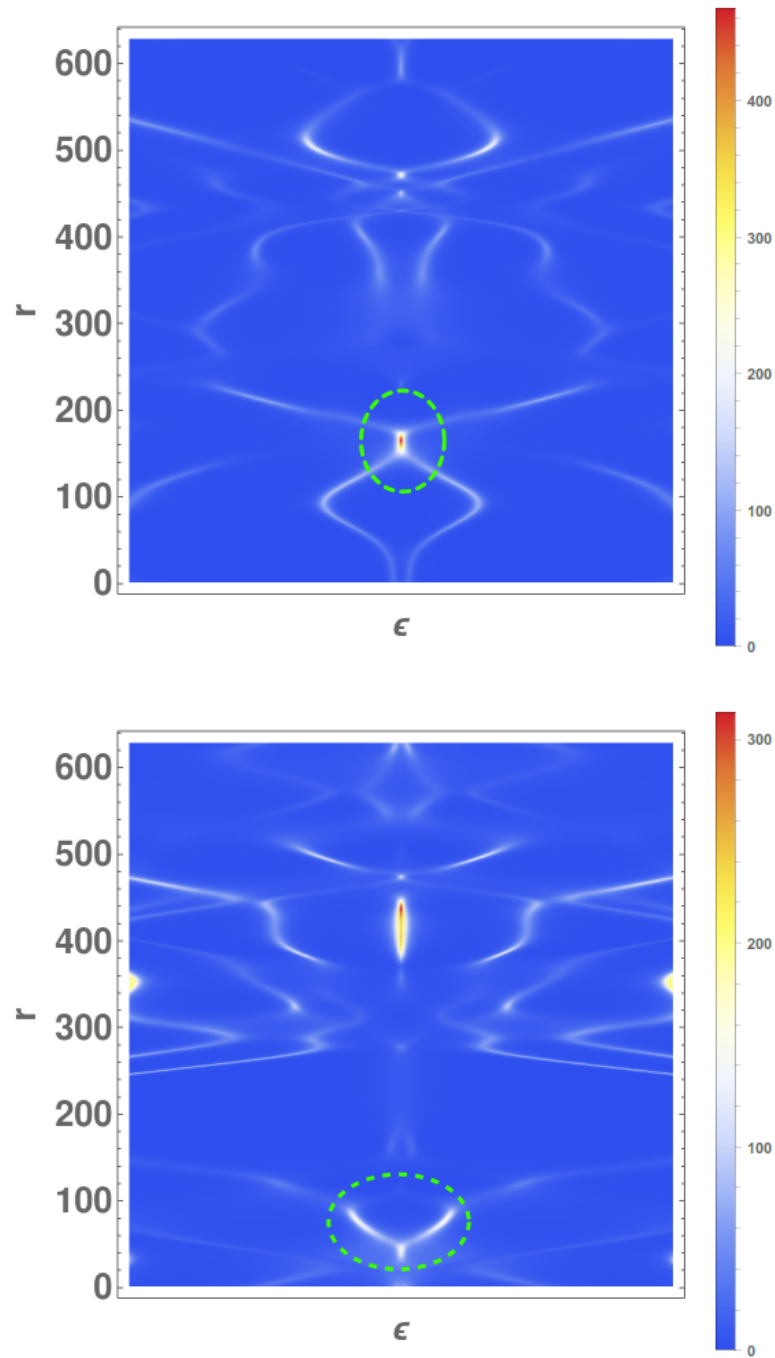
Figure 4.17: The density of states at a fixed selected point in the wire, as a function of energy and parameter r. Top: At $r \sim 150$ two peaks merge into a sharp peak which splits up again at $r \sim 180$ (green oval). Bottom: At $r \sim 50$ a splitting of a peak is clearly visible (green oval).
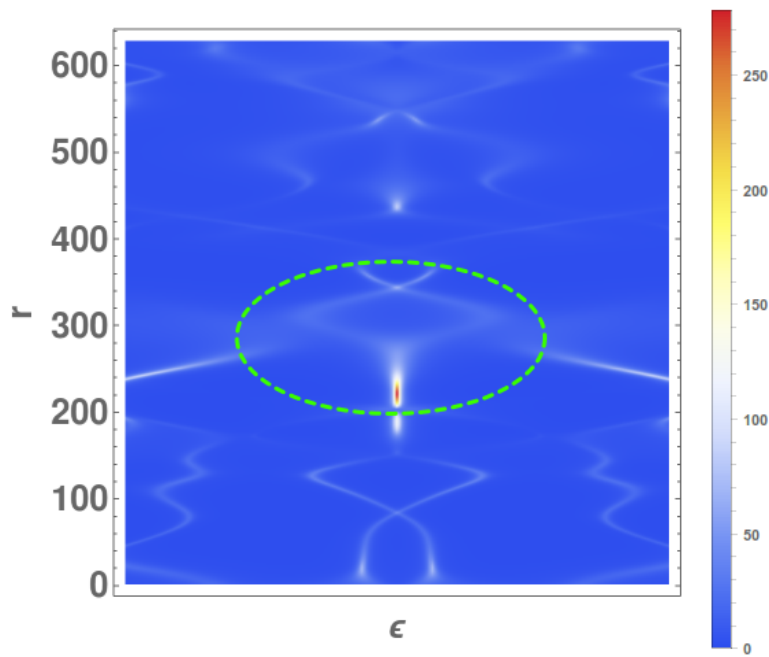
Figure 4.18: The density of states at a fixed selected point in the wire, as a function of energy and parameter r. At $r \sim 250$ a sharp peak is visible that very diffusively splits at $r \sim 300$.

Part III

Appendices

A

Zero-energy bound states

We now derive the number of zero-energy bound states given by the topological invariants derived in sec. 2.3. We focus on the chiral classes, since the proof for class D can be easily derived from more general proof. The pole structure of the Eilenberger equation $\mathcal{Q}$ at zero-energy is determined by the secular matrix (2.24) around zero. Since the spectrum of the terminal Eilenberger functions $\mathcal{Q}_\pm$ is gapped, we can safely neglect their energy dependence. For the sake of simplicity we define $\mathcal{D} \equiv \mathcal{D}(\epsilon = 0)$. As it was proven in sec. 2.3.1, the degree of degeneracy or nullity of the zero-energy secular matrix is always even $(2\mathcal{N})$. Recall that for the chiral classes $\mathcal{N}$ was defined as the nullity of each chiral block. However, we will see below that the actual number of zero-energy states is $\mathcal{N}$ rather than $2\mathcal{N}$. The physical zero-energy modes that contribute to the singularity of the $\mathcal{Q}$-matrix, span only half of the kernel of $\mathcal{D}$. We denote the left null space of $\mathcal{D}$ by Ω_0^L and consider a bra state $\langle\phi_1| = (\phi_1^{(1)}, \phi_1^{(2)})$ thereof, where the spinor structure refers to the chiral basis introduced earlier. By definition $\langle\phi|\mathcal{D} = 0$ and

$$\langle\phi_1|\mathcal{Q}_+ M = -\langle\phi_1|M\mathcal{Q}_-.$$

Due to this property we can define an additional bra state $\langle\phi_2| \equiv \langle\phi_1|\mathcal{Q}_+$ which is also an element of Ω_0^L. This follows from the fact that $\mathcal{Q}_\pm^2 = \mathbb{1}$ and

$$\begin{aligned}
\langle\phi_2|\mathcal{D} &= \langle\phi_1|\mathcal{Q}_+ \left(\mathcal{Q}_+ + \mathcal{Q}_+ M\mathcal{Q}_- M^{\mathrm{T}}\right) \\
&= \langle\phi_1| \left(\mathbb{1} + \mathcal{Q}_+ M\mathcal{Q}_- M^{-1}\right) \\
&= \langle\phi_1| \left(\mathbb{1} - M\mathcal{Q}_-^2 M^{-1}\right) = 0.
\end{aligned}$$

More general, with the projectors

$$P_\pm = \frac{1}{2}(\mathbb{1} \pm \mathcal{Q}_+),$$

satisfying $P_\pm^2 = \mathbb{1}$ and $P_+ P_- = 0$, any state $\langle \phi_\pm | \equiv \langle \phi_1 | P_\pm$ belongs to Ω_L^0. We denote the two projected subspaces of the null spaces Ω_L^0 by $\Omega_L^\pm \equiv \Omega_L^0 P_\pm$. As we will see later, the projectors $P_\pm$ divide Ω_L^0 into two subspaces of equal dimensions, i.e. $\dim \Omega_L^+ = \dim \Omega_L^- = \frac{1}{2}\dim \Omega_L^0 = \mathcal{N}$. Due to the properties of $\mathcal{D}$, the auxiliary $\tilde{\mathcal{D}} \equiv \mathcal{D}\Gamma$ is anti-hermitian and since $\Gamma^2 = \mathbb{1}$, its left null space is identical to Ω_L^0. Hence the right null space of $\tilde{\mathcal{D}}$ is related to the left one by conjugation, $\Omega_R^0 = (\Omega_L^0)^\dagger$. If we define a full basis $\{\langle \Phi_\pm^j|\}$ with $j = 1, \ldots, \mathcal{N}$ in the projected subspaces $\Omega_L^\pm$, these states are related to the corresponding ket states by $|\Phi_\pm^j\rangle = (\langle \Phi_\pm^j|)^\dagger$, which in return can be used construct a full basis $\{|\Phi_\pm^j\rangle\}$ in Ω_R^0. The very construction of this basis vectors shows, that they are not orthogonal since generally $P_- P_+^\dagger \neq 0$, where $P_\pm^\dagger$ are the projectors acting on Ω_R^0. One can however, introduce a dual basis $\{\langle \eta_\pm^j|\}$ in Ω_R^0 which is orthogonal, $\langle \Phi_\sigma^j | \eta_{\sigma'} \rangle = \delta_{\sigma\sigma'}^{jj'}$. Using this dual basis the projectors can be written as

$$P_\sigma = \sum_{j=1}^{\mathcal{N}} |\eta_\sigma^j\rangle\langle \Phi_\sigma^j|, \quad P_\sigma^\dagger = \sum_{j=1}^{\mathcal{N}} |\Phi_\sigma^j\rangle\langle \eta_\sigma^j|.$$

The representation in terms of projectors onto the two subspaces $\Omega^\pm$ turns out to be very convenient once the general pole structure of the Eilenberger function around zero is understood. To this end, we rewrite the boundary equations (2.23) into

$$\mathcal{Q}_R = 1 + 2\mathcal{D}_\epsilon^{-1}(1 - \mathcal{Q}_+),$$
$$\mathcal{Q}_R = -1 + 2(1 + \mathcal{Q}_+)\mathcal{D}_\epsilon^{-1}. \tag{A.1}$$

Chiral symmetry restricts $\tilde{\mathcal{D}}_\epsilon$ as follows,

$$\sigma_3 \tilde{\mathcal{D}}_\epsilon \sigma_3 = -\tilde{\mathcal{D}}_{-\epsilon}, \tag{A.2}$$

where σ_3 operates in the chiral basis. At zero energy the matrix $\mathcal{D}$ is non-invertible due to the presence of zero modes. At finite ϵ the pole structure of $\tilde{\mathcal{D}}$ is therefore given by[1] $\tilde{\mathcal{D}}_\epsilon^{-1} \sim \mathcal{R}/\epsilon$, with the energy dependent residue matrix $\mathcal{R}$. The latter is represented in the

---

[1]Linear in ϵ the matrix $\tilde{\mathcal{D}}_\epsilon = \epsilon \begin{pmatrix} \tilde{\mathcal{D}}_{11} & \tilde{\mathcal{D}}_{12} \\ \tilde{\mathcal{D}}_{21} & \frac{1}{\epsilon}\tilde{\mathcal{D}}_{22} + \tilde{\mathcal{D}}_{22^{(1)}} \end{pmatrix}$. In the limit $\epsilon \to 0$ its convergences is only determined by $\tilde{\mathcal{D}}_{11}^{-1}$ which together with eq. (A.2) leads to the pole structure.

dual basis,

$$\mathcal{R} = \sum_{jj';\sigma\sigma'} |\Phi_\sigma^j\rangle \mathcal{R}_{jj'}^{\sigma\sigma'} \langle \Phi_{\sigma'}^{j'}|, \quad \mathcal{R}_{jj'}^{\sigma\sigma'} = \langle \eta_\sigma^j | \mathcal{R} | \eta_{\sigma'}^{j'} \rangle.$$

We focus on the singular part of the matrix $\tilde{Q}_R$, which according to eq. (A.1) is given by

$$\Gamma \tilde{Q}_R^{\text{sing}} \Gamma = \frac{2}{\epsilon} \mathcal{R}(\mathbb{1} - \mathcal{Q}_+) = \frac{2}{\epsilon}(\mathbb{1} - \mathcal{Q}_+^\dagger)\mathcal{R} = \frac{4}{\epsilon}\mathcal{R}P_- = \frac{4}{\epsilon}P_-^\dagger \mathcal{R},$$

and since $P_-^2 = \mathbb{1}$, we find

$$\tilde{\mathcal{Q}}_R^{\text{sing}} = \frac{4}{\epsilon}\Gamma |\Phi_-^j\rangle \mathcal{R}_{jj'}^{--} \langle \Phi_-^{j'}|\Gamma = \frac{4}{\epsilon}\Gamma P_-^\dagger \mathcal{R} P_-\Gamma.$$

The final expression for the singular part of the propagator is one step away. The definition of the quasi-classical Green's function, eq. (2.5) and the Eilenberger function eq. (2.8) yield that at zero energy and $x = x' = x_R$, the propagator is given by

$$G(x_R, x_R; \epsilon) \sim -\frac{2i}{\epsilon} \mathrm{R}_{jj'}^{--} \hat{v}^{-\frac{1}{2}} \Gamma^\dagger |\Phi_-^j\rangle \langle \Phi_-^{j'}|\Gamma \hat{v}^{-\frac{1}{2}},$$

where we introduced the (diagonal) velocity matrix $\hat{v}$. The spectral decomposition of the Green's function decompose contains two terms, one representing the subgap Andreev levels and a second one outside this gap

$$G(x, x'; \epsilon) = G_{\text{subgap}} + G_{\text{BdG}}.$$

If we denote by $|\psi_E(x)\rangle$ the normalised eigenfunctions of the BdG Hamiltonian and by E_g the gap in the spectrum of the wire, the latter term is given by

$$G_{\text{BdG}}(x, x'; \epsilon) = \left(\int\limits_{E_g}^{+\infty} \mathrm{d}E + \int\limits_{-\infty}^{-E_g} \mathrm{d}E \right) \frac{|\psi_E(x)\rangle\langle\psi_E(x')|}{\epsilon - E}.$$

The contribution of the subgap Andreev levels is given by

$$G_{\text{subgap}}(x, x'; \epsilon) = \sum_{j=-j_{\text{max}}}^{j_{\text{max}}} \frac{|\psi_{E_j}(x)\rangle\langle\psi_{E_j}(x')|}{\epsilon - E_j},$$

where we have used that due to charge-conjugation symmetry $-E_j = E_{-j}$. Now if the systems hosts a Majorana state, it has $E_0 = 0$ and this state is represented by a term

$$\frac{|\psi_0(x)\rangle\langle\psi_0(x')|}{\epsilon},$$

which is of course singular at zero energy. Comparison to the singular part thus leads to the conclusion, that the amplitude of the Majorana particle at the point x_R is given by

$$-\frac{2i}{\epsilon}\mathrm{R}_{jj'}^{--}\hat{v}^{-\frac{1}{2}}u_C^\dagger|\Phi_-^j\rangle = |\psi_0(x_R)\rangle.$$

Amplitudes at arbitrary position x are then obtained by applying the transfer matrix $M(x, x_R)$ to the state $|\psi_0(x_R)\rangle$. We see that the space of physical zero-energy states projected to the point x_R, is given by the linear space spanned by the vectors $\Gamma|\Phi_-^j\rangle$ with $j = 1, \ldots, \mathcal{N}$. Note that only states from the subspace Ω_R^- contribute, while Ω_R^+ does not contribute at all.

We have yet to prove that the $\dim(\Omega_R^\pm) = \dim(\Omega_L^\pm) = \mathcal{N}$. Recall the prototypical setup shown in the lower panel of fig. A.1. Two states $|\phi_L\rangle$ and $|\phi_R\rangle$ left and right of the scattering region, are mapped onto each other by the transfer matrix M. The terminal configurations $\mathcal{Q}_\pm$ are the asymptotics of the position dependent Eilenberger function $\mathcal{Q}(x)$ at $x \to \pm\infty$. A zero energy state $|\phi\rangle$ must satisfy $\mathcal{H}|\phi\rangle = 0$, which according to our definition (2.6) takes the form of a linear matrix differential equation

$$\partial_x|\phi\rangle = -\mathcal{L}_{\epsilon=0}|\phi\rangle. \tag{A.3}$$

The general solution of this equation, $|\phi(x)\rangle = M(x, x_0)|\phi(x_0)\rangle$, can be obtained using the definition of the transfer matrix in eq. (2.16) and an arbitrary state $|\phi(x_0)\rangle$ at some spatial point x_0. If we define the conjugate state $\langle\tilde{\phi}| := \langle\phi|\Gamma$ we find that it solves

$$\partial_x\langle\tilde{\phi}| = \langle\tilde{\phi}|\mathcal{L}_{\epsilon=0}.$$

Now let $|\phi_{R/L}\rangle$ be the states right/left of the scattering region. Both states are related via $|\phi_R\rangle = M|\phi_L\rangle$. Using the flux conservation property of M-matrix (2.18) the above equations is equivalent to

$$\langle\tilde{\phi}_R| = \langle\tilde{\phi}_L|M^{-1}. \tag{A.4}$$

Within our model, the evolution operator $\mathcal{L}_\epsilon$ is position independent outside of the scattering region. We denote by $\mathcal{L}_\pm$ its value at $\epsilon = 0$ in the right/left terminal, respectively. Let $\mathcal{L}_{\sigma=\pm}$ be diagonalised according to eq. (2.12), with $\Sigma = \sigma_3$, i.e the eigenvalues come in pairs $(-\lambda_\sigma^j, \lambda_\sigma^j)$ with positive real parts, where j denotes the joint channel index. Consider

now the right terminal and denote by $\langle\chi^R_{j,\pm}|$ the left eigenstates of $\mathcal{L}_+$, i.e.

$$\langle\chi^R_{j,\pm}|\mathcal{L}_+ = \pm\lambda^j_+ \langle\chi^R_{j,\pm}|.$$

The rows of the diagonalising matrix T_+ are given by the bras and hence by construction,

$$\langle\chi^R_{j,\pm}|\mathcal{Q}_+ = \pm\langle\chi^R_{j,\pm}|. \tag{A.5}$$

If a zero mode $\langle\tilde{\phi}|$ exists, its general form for $x > x_R$ is given by

$$\langle\tilde{\phi}(x)| = \sum_j C_j e^{-\lambda^j_+ x}\langle\chi^R_{j,-}| + C'_j e^{+\lambda^j_+ x}\langle\chi^R_{j,+}|, \quad x > x_R.$$

Since the physical state should decay at $x \to +\infty$, it follows that $C'_j = 0$ for all j (we had chosen the real parts of the eigenvalues to be positive). The support of this expansion is bounded by the scattering region, $\langle\tilde{\phi}_R| \equiv \langle\tilde{\phi}(x_R)|$. Using relation (A.5) it then follows that

$$\langle\tilde{\phi}_R|\mathcal{Q}_+ = -\langle\tilde{\phi}_R|, \quad \langle\tilde{\phi}_L|\mathcal{Q}_- = +\langle\tilde{\phi}_L|. \tag{A.6}$$

By virtue of eq. (A.4), we conclude that these two relations are equivalent to the equation discussed earlier

$$\langle\tilde{\phi}_R|(M\mathcal{Q}_-M^{-1} + \mathcal{Q}_+) = 0. \tag{A.7}$$

In other words, the state $\langle\tilde{\phi}_R|$ belongs to the left kernel of the secular matrix $\mathcal{D}$. More precisely, $\langle\tilde{\phi}_R| \in \Omega^-_L$, since eq. (A.6) leads to $\langle\tilde{\phi}_R|P_- = \langle\tilde{\phi}_R|$. The linear differential equation (A.3) contains bounded and unbounded solutions (illustrated as red and grey curves in fig. A.1). The crucial observation now is that, if we were to consider the unbounded solutions, similar arguments would lead to the same secular equation (A.7), however the eigenstates would satisfy

$$\langle\tilde{\phi}_R|\mathcal{Q}_+ = +\langle\tilde{\phi}_R|, \quad \langle\tilde{\phi}_L|\mathcal{Q}_- = -\langle\tilde{\phi}_L|.$$

Therefore, in this case the state $\langle\tilde{\phi}_R|$ would belong to the complementary subspace Ω^+_L. From the theory of linear differential operators it is known that the number of bounded and unbounded eigenstates is equal. This fact suggests that $\dim(\Omega^+_L) = \dim(\Omega^-_L)$, as claimed.
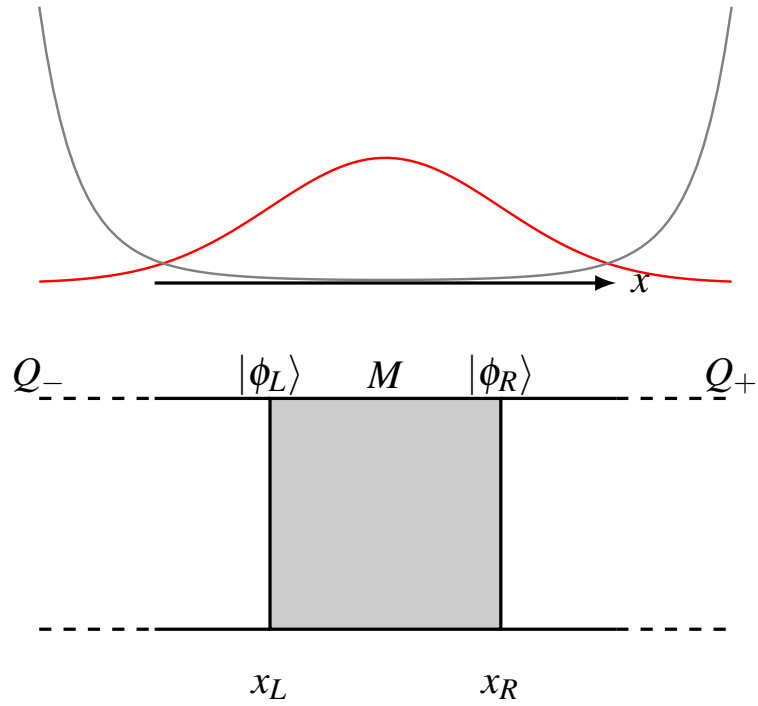
Figure A.1: Top: Schematic illustration of the formal unbound solutions (grey) and bound solutions (red) of the eq. (A.3). Bottom: Schematic illustration of the quantum wire, the scattering region is indicated as a grey square. The states $|\phi_{L/R}\rangle$ at the boundaries $(x_{L/R})$ are related via the transfer matrix M. Within the terminals the $\mathcal{Q}$ matrix converges to $\mathcal{Q}_{\pm}$.

B

Chern characters in terms of the Eilenberger functions $\mathcal{Q}$

In this appendix we derive the Hall conductance and the Chern character c_2 in terms of the Eilenberger functions $\mathcal{Q}$. We begin with the $(2+1)$-dimensional system, and consider a Dirac Hamiltonian $H = \sum_i \sigma_i h_i(k)$, where $h_{x,y} = k_{x,y}$ and $h_3 = m$. By virtue of the Kubo formula the Hall conductance is given by

$$\sigma_{xy} \propto \lim_{\omega \to 0} \omega^{-1} \int \mathrm{d}k_y \mathrm{d}\epsilon \sum_{\alpha,\beta} \left(\frac{1}{\lambda_+^\alpha + \lambda_-^\beta} P_{\alpha\beta} N_{\beta\alpha} \right). \tag{B.1}$$

Here the matrices P and N are related to the evolution operator by

$$P = T_+^{-1} \Gamma J_y \mathcal{Q}_- T_- = -i T_+^{-1} (\partial_{k_y} \mathcal{L}) \mathcal{Q}_- T_-$$
$$N = T_-^{-1} \mathcal{Q}_+ T_+,$$

where we used that $\mathcal{L} = -i\Gamma(\epsilon - \hat{m})$, and $J_y = \partial_{k_y} H$. For the definitions of the subscripts we refer to the main text. The crucial observation is that the eigenvalues always come in pairs (± 1) and the above indices α and β are redundant. The above expression then simplifies to

$$\sigma_{xy} \propto \lim_{\omega \to 0} \omega^{-1} \int \mathrm{d}k_y \mathrm{d}\epsilon \frac{1}{\lambda_+ + \lambda_-} \operatorname{tr} PN.$$

Due to the limit in eq. (B.1), we expand the trace to first order in ω,

$$\begin{aligned}
\operatorname{tr} PN\big|_{\omega=0} &= -i \operatorname{tr} T_+^{-1}(\partial_{k_y}\mathcal{L})\mathcal{Q} \cdot gT_+ \\
&= -i \operatorname{tr} \partial_{k_y}\mathcal{L} \\
&= \operatorname{tr} \Gamma J_y = 0,
\end{aligned}$$

where in the last equation we used that Γ and J_y anti-commute. In addition

$$\begin{aligned}
\operatorname{tr} PN &= -i \operatorname{tr}\left((\partial_{k_y}\mathcal{L})\mathcal{Q}_-\mathcal{Q}_+\right) \\
&= -i \operatorname{tr}\left(\partial_{k_y}(\lambda\mathcal{Q}_\epsilon)(\mathcal{Q}_-\mathcal{Q}_+)\right) \\
&\simeq -i \operatorname{tr}\left((\partial_{k_y}(\lambda\mathcal{Q}_\epsilon))(\mathcal{Q}_\epsilon(\partial_\epsilon\mathcal{Q})-(\partial_\epsilon\mathcal{Q})\mathcal{Q}_\epsilon)\right)\omega \\
&= -2i \operatorname{tr}\left((\partial_{k_y}(\lambda\mathcal{Q}_\epsilon))(\mathcal{Q}_\epsilon(\partial_\epsilon\mathcal{Q}))\right)\omega,
\end{aligned}$$

where we used that the fact that $\mathcal{Q}(\partial_\epsilon\mathcal{Q})+(\partial_\epsilon\mathcal{Q})\mathcal{Q}=0$, as well as $\partial_\omega\mathcal{Q}_{\epsilon-\omega}=-\partial_\epsilon\mathcal{Q}$. If the derivative with respect to k_y acts on the eigenvalues λ, the contribution is vanishing,

$$(\partial_{k_y}\lambda)\operatorname{tr}\partial_\epsilon\mathcal{Q}\omega = 0,$$

since $\operatorname{tr}\mathcal{Q}=0$. We see that

$$\operatorname{tr} PN = -i\lambda \operatorname{tr}(\partial_{k_y}\mathcal{Q})\mathcal{Q}(\partial_\epsilon\mathcal{Q})\omega$$

and therefore conclude

$$\sigma_{xy} \propto \int \mathrm{d}\epsilon \mathrm{d}k_y \operatorname{tr}(\partial_{k_y}\mathcal{Q})\mathcal{Q}(\partial_\epsilon\mathcal{Q}).$$

We now turn to the $(4+1)$-dimensional case. With $\Gamma \cdot J_\mu = -i(\partial_\mu\mathcal{L})$ for $\mu = \Phi, \Theta$ the three matrices appearing in the trace in eq. (2.44) are given by

$$\begin{aligned}
P &= T_3^{-1}\Gamma J_\phi \mathcal{Q}_1 T_1 = -iT_3^{-1}(\partial_\phi\mathcal{L})\mathcal{Q}_1 T_1, \\
N &= T_1^{-1}\mathcal{Q}_2 T_2, \\
V &= T_2^{-1}\Gamma J_\theta \mathcal{Q}_3 T_3 = -iT_2^{-1}(\partial_\theta\mathcal{L})\mathcal{Q}_3 T_3.
\end{aligned}$$

For the definitions of the subscripts we again refer to the main text. Due to the pair structure of the eigenvalues, we see that

$$\operatorname{tr} PNV = \operatorname{tr}\left(\Gamma J_\phi \mathcal{Q}_1 \mathcal{Q}_2 \Gamma J_\theta \mathcal{Q}_3\right) = -\operatorname{tr}\left((\partial_\phi\mathcal{L})\mathcal{Q}_1 \mathcal{Q}_2(\partial_\theta\mathcal{L})\mathcal{Q}_3\right).$$

Since the limit eq. (2.43) involves q_2 and ω_3 we expand the trace in both variables. The

zeroth order term then reads

$$\operatorname{tr} PNV\Big|_{\substack{q_2 = q_3 = 0 \\ w_2 = w_3 = 0}} = \operatorname{tr}(\partial_\phi \mathcal{L})(\partial_\theta \mathcal{L})\mathcal{Q} = -\operatorname{tr}\Gamma\Gamma_\phi \Gamma\Gamma_\theta \frac{\mathcal{L}}{\lambda} = \lambda^{-1} \operatorname{tr}\Gamma_\phi \Gamma_\theta \mathcal{L}$$

$$= \lambda^{-1}(-i\epsilon\operatorname{tr}\Gamma_\phi \Gamma_\theta \Gamma + i\operatorname{tr}\Gamma_\phi \Gamma_\theta \Gamma\hat{m}) = 0,$$

due to the properties of the trace and the Dirac matrices. We set $\omega_2 = q_3 = 0$ which reduces the container subscripts to

$$1 \mathrel{\hat{=}} (k_2, \epsilon),\ 2 \mathrel{\hat{=}} (k_2, \epsilon - \omega),\ 3 \mathrel{\hat{=}} (k_2 - q_2, \epsilon - \omega).$$

The term linear in q_2 in the expansion of the trace also vanishes,

$$\operatorname{tr}(\partial_\phi \mathcal{L})g_1 g_2(\partial_\theta \mathcal{L})\mathcal{Q}_3 \simeq \operatorname{tr}(\partial_\phi \mathcal{L})(\partial_\theta \mathcal{L})(\partial_{q_2}\mathcal{L} + \partial_{q_2}\lambda^{-1})q_2$$

$$= \operatorname{tr}\Gamma\Gamma_\phi \Gamma\Gamma_\theta(ik_2\Gamma\Gamma_2 + \mathcal{L}\times\text{const.})q_2 = 0.$$

So does the term linear in ω, since

$$\operatorname{tr}(\partial_\phi \mathcal{L})\mathcal{Q}_1(\partial_\omega \mathcal{Q}_2)(\partial_\theta \mathcal{L})\mathcal{Q}_3 = \operatorname{tr}\Gamma\Gamma_\phi \mathcal{Q}(\partial_\omega \mathcal{L} + \mathcal{L}\times\text{const.})\Gamma\Gamma_\theta \mathcal{Q}\omega$$

$$= -\operatorname{tr}\Gamma\Gamma_\phi \mathcal{Q}(i\epsilon\Gamma)\Gamma\Gamma_\theta \mathcal{Q} + \operatorname{tr}\Gamma\Gamma_\phi \mathcal{Q}\mathcal{L}\Gamma\Gamma_\theta \mathcal{Q}\omega$$

$$= -i\epsilon\operatorname{tr}\Gamma\Gamma_\phi \mathcal{Q}\Gamma_\theta \mathcal{Q} + \lambda\operatorname{tr}\Gamma\Gamma_\phi \Gamma\Gamma_\theta \mathcal{Q}\omega$$

$$= -i\epsilon\operatorname{tr}\Gamma\Gamma_\phi \mathcal{Q}\Gamma_\theta \mathcal{Q} - \operatorname{tr}\Gamma_\phi \Gamma_\theta \mathcal{L}\omega.$$

The second term in the above expression has already been identified to be of vanishing trace. If we expand the first term, terms of zeroth and first order in $\hat{m}$, $\Gamma_\theta \Gamma\Gamma_\phi(\hat{m})^{n=0,1}$ vanish as discussed earlier. The remaining quadratic part $\Gamma\Gamma_\phi \Gamma_\theta \hat{m}^2$ is proportional to $\Gamma\Gamma_\phi \Gamma_\theta$, since $(\hat{m})^2 \propto \mathbb{1}$, and vanishes as well. In second order we find

$$\operatorname{tr}(\partial_\phi \mathcal{L})(\partial_\theta \mathcal{L})\partial^2_{k_y, \omega}(\mathcal{L}/\lambda) = \operatorname{tr}(\partial_\phi \mathcal{L})(\partial_\theta \mathcal{L})\left((\partial_{k_y}\mathcal{L})\partial_\omega(\lambda^{-1}) + (\partial_{ky}\lambda^{-1})(\partial_\omega \mathcal{L}) + \mathcal{L}(\partial^2_{\omega, k_y}\lambda^{-1})\right)$$

$$= -\operatorname{tr}\Gamma_\phi \Gamma_\theta\left(\Gamma\Gamma_2 \times \text{const.} + \Gamma \times \text{const.}\right),$$

which, as we know by now, vanishes. For mixed derivatives there are three contributions

$$\operatorname{tr}\left[\lambda^2(\partial_\phi \mathcal{Q})\mathcal{Q}(\partial_\omega \mathcal{Q})(\partial_\theta \mathcal{Q})(\partial_{k_y}\mathcal{Q}) + \lambda(\partial_\phi \mathcal{Q})\mathcal{Q}(\partial_\omega \mathcal{Q})\mathcal{Q}(\partial_{k_y}\mathcal{Q})(\partial_\theta \lambda)\right.$$

$$\left. + \lambda\mathcal{Q}(\partial_\phi \lambda)\mathcal{Q}(\partial_\omega \mathcal{Q})(\partial_\theta \mathcal{Q})(\partial_{k_y}\lambda) + \lambda\mathcal{Q}(\partial_\phi \lambda)\mathcal{Q}(\partial_\omega \mathcal{Q})\mathcal{Q}(\partial_\theta \lambda)(\partial_{k_y}\mathcal{Q})\right].$$

The second and third term in the above expression can be simplified, using that

$$\mathcal{Q}\partial_\epsilon \mathcal{Q} + (\partial_\epsilon \mathcal{Q})\mathcal{Q} = 0,$$

leaving us with terms of the form

$$\mathrm{tr}(\partial_i\mathcal{Q})(\partial_j\mathcal{Q})(\partial_h\mathcal{Q}) = \mathrm{tr}\,\mathcal{Q}(\partial_i\mathcal{Q})(\partial_j\mathcal{Q})(\partial_h\mathcal{Q})\mathcal{Q} = -\,\mathrm{tr}(\partial_i\mathcal{Q})(\partial_j\mathcal{Q})(\partial_h\mathcal{Q}),$$

which obviously do not contribute. The last term in the above expression can be expanded in $\mathcal{L}$ and expressed as

$$\mathrm{tr}(a_1(\partial_\omega\mathcal{L})\mathcal{L}(\partial_{k_y}\mathcal{L}) + \mathcal{L}^2(a_2\partial_\omega\mathcal{L} + a_3\partial_{k_y}\mathcal{L}) + \mathcal{L}^3 a_4).$$

The term cubic in $\mathcal{L}$ vanishes since $\mathcal{L}$ squares to a constant, while the quadratic term leaves us with the trace over the derivatives of $\mathcal{L}$, which is vanishing as well. The remaining term splits into $\mathrm{tr}(a_1\Gamma + a_2\Gamma\delta H\Gamma_y)$ which is vanishing as well. Leaving us with

$$\mathrm{tr}\left[\lambda^2(\partial_\phi\mathcal{Q})\mathcal{Q}(\partial_\omega\mathcal{Q})(\partial_\theta\mathcal{Q})(\partial_{k_y}\mathcal{Q})\right].$$

Due to the limit considered in eq. (2.43), it follows that $\lambda_1 = \lambda_2 = \lambda_3$ and therefore, the factor λ^2 is cancelled by the pre-factor in eq. (2.45) and we are left with eq. (2.46).

Bibliography

[1] D. J. Thouless, M. Kohmoto, M. P. Nightingale, and M. den Nijs. Quantized hall conductance in a two-dimensional periodic potential. *Phys. Rev. Lett.*, **49**, 405–408, Aug 1982.

[2] M. Z. Hasan and C. L. Kane. *Colloquium* : Topological insulators. *Rev. Mod. Phys.*, **82**, 3045–3067, Nov 2010.

[3] S. Ryu, A. P. Schnyder, A. Furusaki, and A. W. W. Ludwig. Topological insulators and superconductors: tenfold way and dimensional hierarchy. *New Journal of Physics*, **12** (6), 065010, 2010.

[4] A. Altland and M. R. Zirnbauer. *Phys. Rev. B*, **55**, 1142, 1997.

[5] A. Kitaev. Periodic table for topological insulators and superconductors. *AIP Conference Proceedings*, **1134**(1), 2009.

[6] C. L. Kane and E. J. Mele. Z_2 topological order and the quantum spin hall effect. *Phys. Rev. Lett.*, **95**, 146802, Sep 2005.

[7] C. L. Kane and E. J. Mele. Quantum spin hall effect in graphene. *Phys. Rev. Lett.*, **95**, 226801, Nov 2005.

[8] M. König, S. Wiedmann, C. Brüne, A. Roth, H. Buhmann, L. W. Molenkamp, X.-L. Qi, and S.-C. Zhang. Quantum spin hall insulator state in hgte quantum wells. *Science*, **318**(5851), 766–770, 2007.

[9] A. Kitaev. *Phys. Usp.*, **44**, 131, 2001.

[10] E. Majorana. *Nuovo Cimento*, **5**, 1937.

[11] J. Alicea, Y. Oreg, G. Refael, F. von Oppen, and M. P. A. Fisher. Non-abelian statistics and topological quantum information processing in 1d wire networks. *Nat Phys*, **7**, 412.

[12] V. Mourik, K. Zuo, S. M. Frolov, S. R. Plissard, E. P. A. M. Bakkers, and L. P. Kouwenhoven. Signatures of majorana fermions in hybrid superconductor-semiconductor nanowire devices. *Science*, **336**(6084), 1003–1007, 2012.

[13] A. Das, Y. Ronen, Y. Most, Y. Oreg, M. Heiblum, and H. Shtrikman. *Nature Physics*, **8**, 887, 2012.

[14] R. M. Lutchyn, J. D. Sau, and S. Das Sarma. *Phys. Rev. Lett.*, **105**, 077001, 2010.

[15] Y. Oreg, G. Refael, and F. von Oppen. *Phys. Rev. Lett.*, **105**, 177002, 2010.

[16] G. Eilenberger. Transformation of gorkov's equation for type ii superconductors into transport-like equations. *Zeitschrift für Physik*, **214**(2), 195–213, 1968.

[17] A. Larkin and Y. N. Ovchinnikov. Quasiclassical method in the theory of superconductivity. *Sov Phys JETP*, **28**(6), 1200–1205, 1969.

[18] W. Belzig, F. K. Wilhelm, C. Bruder, G. Schön, and A. D. Zaikin. Quasiclassical green's function approach to mesoscopic superconductivity. *Superlattices and microstructures*, **25**(5), 1251–1288, 1999.

[19] D. Bagrets and A. Altland. *Phys. Rev. Lett.*, **109**, 227005, 2012.

[20] J. Liu, A. C. Potter, K. T. Law, and P. A. Lee. Zero-bias peaks in the tunneling conductance of spin-orbit-coupled superconducting wires with and without majorana end-states. *Phys. Rev. Lett.*, **109**, 267002, Dec 2012.

[21] D. I. Pikulin, J. P. Dahlhaus, M. Wimmer, H. Schomerus, and C. W. J. Beenakker. A zero-voltage conductance peak from weak antilocalization in a majorana nanowire. *New Journal of Physics*, **14**(12), 125011, 2012.

[22] M. Nakahara. *Geometry, topology and physics*. CRC Press, 2003.

[23] M. Zirnbauer. *J. Math. Phys.*, **37**, 4986, 1996.

[24] E. Cartan. Sur une classe remarquable d'espaces de riemann, i. *Bulletin de la Société Mathématique de France*, pages 214–216, 1926.

[25] R. Bott. An application of the morse theory to the topology of lie groups. *Bull. Soc. Math. France*, **84**(251-281), 23, 1956.

[26] A. P. Schnyder, S. Ryu, A. Furusaki, and A. W. W. Ludwig. Classification of topological insulators and superconductors in three spatial dimensions. *Phys. Rev. B*, **78**, 195125, Nov 2008.

[27] X.-L. Qi, T. L. Hughes, and S.-C. Zhang. Topological field theory of time-reversal invariant insulators. *Phys. Rev. B*, **78**, 195424, Nov 2008.

[28] K. v. Klitzing, G. Dorda, and M. Pepper. New method for high-accuracy determination of the fine-structure constant based on quantized hall resistance. *Phys. Rev. Lett.*, **45**, 494–497, Aug 1980.

[29] M. V. Berry. Quantal phase factors accompanying adiabatic changes. *Proceedings of the Royal Society of London A: Mathematical, Physical and Engineering Sciences*, **392** (1802), 45–57, 1984. ISSN 0080-4630.

[30] M. Fruchart and D. Carpentier. An introduction to topological insulators. *Comptes Rendus Physique*, **14**(9–10), 779 – 815, 2013. ISSN 1631-0705. Topological insulators / Isolants topologiques Topological insulators / Isolants topologiques.

[31] M. R. Zirnbauer. Advanced seminar: Topological insulators. University of Cologne, 2010.

[32] F. D. M. Haldane. Model for a quantum hall effect without landau levels: Condensed-matter realization of the "parity anomaly". *Phys. Rev. Lett.*, **61**, 2015–2018, Oct 1988.

[33] B. A. Bernevig, T. L. Hughes, and S.-C. Zhang. Quantum spin hall effect and topological phase transition in hgte quantum wells. *Science*, **314**(5806), 1757–1761, 2006.

[34] B. A. Bernevig and S.-C. Zhang. Quantum spin hall effect. *Physical review letters*, **96** (10), 106802, 2006.

[35] L. Fu and C. L. Kane. Time reversal polarization and a Z_2 adiabatic spin pump. *Phys. Rev. B*, **74**, 195312, Nov 2006.

[36] X.-L. Qi and S.-C. Zhang. Topological insulators and superconductors. *Rev. Mod. Phys.*, **83**, 1057–1110, Oct 2011.

[37] B. A. Bernevig. *Topological insulators and topological superconductors*. Princeton University Press, 2013.

[38] H. Zhang, C.-X. Liu, X.-L. Qi, X. Dai, Z. Fang, and S.-C. Zhang. Topological insulators in bi2se3, bi2te3 and sb2te3 with a single dirac cone on the surface. *Nature physics*, **5** (6), 438–442, 2009.

[39] Y. Chen, J. Analytis, J.-H. Chu, Z. Liu, S.-K. Mo, X.-L. Qi, H. Zhang, D. Lu, X. Dai, Z. Fang, et al. Experimental realization of a three-dimensional topological insulator, bi2te3. *Science*, **325**(5937), 178–181, 2009.

[40] L. Fu, C. L. Kane, and E. J. Mele. Topological insulators in three dimensions. *Physical Review Letters*, **98**(10), 106803, 2007.

[41] C.-K. Chiu, H. Yao, and S. Ryu. Classification of topological insulators and super-conductors in the presence of reflection symmetry. *Physical Review B*, **88**(7), 075142, 2013.

[42] T. Morimoto and A. Furusaki. Topological classification with additional symmetries from clifford algebras. *Physical Review B*, **88**(12), 125129, 2013.

[43] G. Fekete. Particle and atomic physics with eight numerical exactitude. *http://vixra.org/abs/1401.0196*.

[44] J. Bardeen, L. N. Cooper, and J. R. Schrieffer. Microscopic theory of superconductivity. *Physical Review*, **106**(1), 162–164, 1957.

[45] J. Valatin. Comments on the theory of superconductivity. *Il Nuovo Cimento*, **7**(6), 843–857, 1958.

[46] N. Bogoliubov. New method in the theory of superconductivity. iii. *Sov. Phys.-JETP (Engl. Transl.);(United States)*, **7**(1), 1958.

[47] L. P. Gorkov. Microscopic derivation of the ginzburg-landau equations in the theory of superconductivity. *Sov. Phys. JETP*, **9**(6), 1364–1367, 1959.

[48] Abrikosov, Gorkov, and Dzyaloshinski. *Methods of quantum field theory in statistical physics*.

[49] Y. Nambu. Axial vector current conservation in weak interactions. *Phys. Rev. Lett.*, **4**, 380–382, 1960.

[50] R. E. Prange and L. P. Kadanoff. Transport theory for electron-phonon interactions in metals. *Phys. Rev.*, **134**, A566–A580, May 1964.

[51] J. Rammer and H. Smith. Quantum field-theoretical methods in transport theory of metals. *Reviews of Modern Physics*, **58**(2), 323, 1986.

[52] M. Eschrig. Distribution functions in nonequilibrium theory of superconductivity and andreev spectroscopy in unconventional superconductors. *Physical Review B*, **61**(13), 9061, 2000.

[53] A. Altland, B. Simons, and D. T. Semchuk. Field theory of mesoscopic fluctuations in superconductor-normal-metal systems. *Advances in Physics*, **49**(3), 321–394, 2000.

[54] M. Feigel'man, A. Larkin, and M. Skvortsov. Keldysh action for disordered superconductors. *Physical Review B*, **61**(18), 12361, 2000.

[55] A. Zaitsev. Quasiclassical equations of the theory of superconductivity for contiguous metals and the properties of constricted microcontacts. *Zh. Eksp. Teor. Fiz*, **86**, 1742–1758, 1984.

[56] Y. V. Nazarov and Y. M. Blanter. *Quantum transport: introduction to nanoscience*. Cambridge University Press, 2009.

[57] A. Shelankov and M. Ozana. Quasiclassical theory of superconductivity: A multiple-interface geometry. *Physical Review B*, **61**(10), 7077, 2000.

[58] Y. V. Nazarov. Novel circuit theory of andreev reflection. *Superlattices and microstructures*, **25**(5), 1221–1231, 1999.

[59] A. Cottet, D. Huertas-Hernando, W. Belzig, and Y. V. Nazarov. Spin-dependent boundary conditions for isotropic superconducting green's functions. *Physical Review B*, **80**(18), 184511, 2009.

[60] I. Kellett. Circuit theory of mesoscopic superconducting components. 2011.

[61] K.-H. Bennemann and J. B. Ketterson. *Superconductivity: Volume 1: Conventional and Unconventional Superconductors Volume 2: Novel Superconductors*. Springer Science & Business Media, 2008.

[62] N. B. Kopnin and N. Kopnin. *Theory of nonequilibrium superconductivity*. Clarendon Press Oxford, 2001.

[63] T. Giamarchi. *Quantum physics in one dimension*. 2004.

[64] P. A. MELLO. Random matrix theory and maximum entropy models for disordered conductors. *Mesoscopic phenomena in solids*, page 369, 1991.

[65] C. L. Wong and K. Law. Majorana kramers doublets in d x 2- y 2-wave superconductors with rashba spin-orbit coupling. *Physical Review B*, **86**(18), 184516, 2012.

[66] W. Su, J. Schrieffer, and A. J. Heeger. Solitons in polyacetylene. *Physical Review Letters*, **42**(25), 1698, 1979.

[67] T. Kaluza. Sitzungsber. preuss. akad. wiss. berlin (math. phys.) k1, 966 (1921); o. klein. *Z. Phys*, **37**(985), 985, 1926.

[68] S. C. Zhang. The chern–simons–landau–ginzburg theory of the fractional quantum hall effect. *International Journal of Modern Physics B*, **6**(01), 25–58, 1992.

[69] F. Wilczek. Two applications of axion electrodynamics. *Physical review letters*, **58**(18), 1799, 1987.

[70] M. Leijnse and K. Flensberg. Introduction to topological superconductivity and majorana fermions. *Semiconductor Science and Technology*, **27**(12), 124003, 2012.

[71] J. Alicea. New directions in the pursuit of majorana fermions in solid state systems. *Reports on Progress in Physics*, **75**(7), 076501, 2012.

[72] N. Read and D. Green. Paired states of fermions in two dimensions with breaking of parity and time-reversal symmetries and the fractional quantum hall effect. *Physical Review B*, **61**(15), 10267, 2000.

[73] X.-L. Qi, T. L. Hughes, S. Raghu, and S.-C. Zhang. Time-reversal-invariant topological superconductors and superfluids in two and three dimensions. *Physical review letters*, **102**(18), 187001, 2009.

[74] T. D. Stanescu and S. Tewari. Majorana fermions in semiconductor nanowires: fundamentals, modeling, and experiment. *Journal of Physics: Condensed Matter*, **25**(23), 233201, 2013.

[75] L. Fu and C. L. Kane. *Phys. Rev. Lett.*, **100**, 096407, 2008.

[76] G. Moor and N. Read. Nonabelions in the fractrional quantum hall effect. *Nucl. Phys.*, **B360**, 362–396, 1991.

[77] J. B. Miller, I. P. Radu, D. M. Zumbühl, E. M. Levenson-Falk, M. A. Kastner, C. M. Marcus, L. N. Pfeiffer, and K. W. West. Fractional quantum hall effect in a quantum point contact at filling fraction 5/2. *Nature Physics*, **3**(8), 561–565, 2007.

[78] S. D. Sarma, C. Nayak, and S. Tewari. Proposal to stabilize and detect half-quantum vortices in strontium ruthenate thin films: Non-abelian braiding statistics of vortices in a p x+ i p y superconductor. *Physical Review B*, **73**(22), 220502, 2006.

[79] S. Bravyi and A. Kitaev. Universal quantum computation with ideal clifford gates and noisy ancillas. *Physical Review A*, **71**(2), 022316, 2005.

[80] A. Akhmerov. Topological quantum computation away from the ground state using majorana fermions. *Physical Review B*, **82**(2), 020509, 2010.

[81] L. Fu and C. L. Kane. Josephson current and noise at a superconductor/quantum-spin-hall-insulator/superconductor junction. *Phys. Rev. B*, **79**, 161408, Apr 2009.

[82] C. W. J. Beenakker. Search for Majorana fermions in superconductors. *ArXiv e-prints*, December 2011.

[83] E. Rashba. Properties of semiconductors with an extremum loop. 1. cyclotron and combinational resonance in a magnetic field perpendicular to the plane of the loop. *Soviet Physics-Solid State*, **2**(6), 1109–1122, 1960.

[84] J. D. Sau, S. Tewari, and S. Das Sarma. Experimental and materials considerations for the topological superconducting state in electron- and hole-doped semiconductors: Searching for non-abelian majorana modes in 1d nanowires and 2d heterostructures. *Phys. Rev. B*, **85**, 064512, Feb 2012.

[85] A. C. Potter and P. A. Lee. Engineering a $p + ip$ superconductor: Comparison of topological insulator and rashba spin-orbit-coupled materials. *Phys. Rev. B*, **83**, 184520, May 2011.

[86] L. Jiang, T. Kitagawa, J. Alicea, A. Akhmerov, D. Pekker, G. Refael, J. I. Cirac, E. Demler, M. D. Lukin, and P. Zoller. Majorana fermions in equilibrium and in driven cold-atom quantum wires. *Physical review letters*, **106**(22), 220402, 2011.

[87] C. Kraus, S. Diehl, P. Zoller, and M. Baranov. Preparing and probing atomic majorana fermions and topological order in optical lattices. *New Journal of Physics*, **14**(11), 113036, 2012.

[88] A. Bühler, N. Lang, C. V. Kraus, G. Möller, S. D. Huber, and H. P. Büchler. Majorana modes and p-wave superfluids for fermionic atoms in optical lattices. *Nature communications*, **5**, 2014.

[89] M. T. Deng, C. L. Yu, G. Y. Huang, M. Larsson, P. Caroff, and H. Q. Xu. Anomalous zero-bias conductance peak in a nb–insb nanowire–nb hybrid device. *Nano Letters*, **12** (12), 6414–6419, 2012. PMID: 23181691.

[90] H. O. H. Churchill, V. Fatemi, K. Grove-Rasmussen, M. T. Deng, P. Caroff, H. Q. Xu, and C. M. Marcus. Superconductor-nanowire devices from tunneling to the multichannel regime: Zero-bias oscillations and magnetoconductance crossover. *Phys. Rev. B*, **87**, 241401, 2013.

[91] P. Neven, D. Bagrets, and A. Altland. Quasiclassical theory of disordered multi-channel majorana quantum wires. *New Journal of Physics*, **15**(5), 055019, 2013.

[92] P. Neven, D. Bagrets, and A. Altland. In preparation. 2015.

[93] D. A. Ivanov. *Journal of Mathematical Physics*, **43**(1), 126, 2002.

[94] F. Haake. *Quantum Signatures of Chaos*. Springer-Verlag.

[95] C. W. J. Beenakker. Random-matrix theory of quantum transport. *Rev. Mod. Phys.*, **69**, 731–808, Jul 1997.

[96] M. Mehta. *Random Matrices (3rd ed)*. Elsevier/Academic Press, 2004.

[97] R. M. Lutchyn, T. D. Stanescu, and S. Das Sarma. Momentum relaxation in a semiconductor proximity-coupled to a disordered s-wave superconductor: Effect of scattering on topological superconductivity. *Phys. Rev. B*, **85**, 140513, Apr 2012.

[98] J. You, Z. Wang, W. Zhang, and F. Nori. Encoding a qubit with majorana modes in superconducting circuits. *Scientific reports*, **4**, 2014.

[99] O. Motrunich, K. Damle, and D. A. Huse. Griffiths effects and quantum critical points in dirty superconductors without spin-rotation invariance: One-dimensional examples. *Phys. Rev. B*, **63**, 224204.

Lobhudelei

Auch wenn dieser Teil oft als ein Ventil für schmalzige Eulogien missbraucht wird, so gilt: *Ehre wem Ehre gebührt* und daher erspare ich dem Leser nichts.

Zuerst und vor allem möchte ich mich bei Dima Bagrets für die hervorragende Betreuung meiner Doktorarbeit bedanken.

Большое спасибо

Fanny Groll möchte für das ausgezeichnete Büroklima danken. Daniel Wieczorek danke ich für die Einführung in den nun so geliebten *Tischtennissport*. Jonas Larson und Hannes Schenck sei für das kritische Korrekturlesen dieser Arbeit gedankt. Letzterem danke ich ebenfalls für die technische Hilfe beim Fertigstellen dieser Arbeit.

Interdisziplinären Beistand bekam ich von Ismail Kutbay, welcher sich als talentierter Übersetzer wissenschaftlicher Probleme in die Sprache der Geschichts(pseudo)wissenschaften erwies. Michael Becker danke ich für die unzähligen Unterhaltungen (auch wenn nicht alle erwünscht waren) und für die hilfreichen Diskussionen bzgl. der Numerik.

Besonderer Dank gilt meinen langjährigen Freunden von NEP, Andreas Michael und Markus D., Martin Joseph B. sowie Daniel Sascha O.

Heike Barth danke ich zutiefst für die Unterstützung und die Gelassenheit im Umgang mit dem Autor in all den Jahren.

Der größte Dank gilt meiner Familie, vorallem meiner Mutter Ute und meinen Großeltern Hilde und Heinrich.

Danke für alles.

Ich versichere, dass ich die von mir vorgelegte Dissertation selbständig angefertigt, die benutzten Quellen und Hilfsmittel vollständig angegeben und die Stell der Arbeit - einschließlich Tabellen, Karten und Abbildungen -, die anderen Werken im Wortlaut oder dem Sinn nach entnommen sind, in jedem Einzelfall als Entlehnung kenntlich gemacht habe; dass diese Dissertation noch keiner anderen Fakultät oder Universität zur Prüfung vorgelegen hat; dass sie - abgesehen von unten angegebenen Teilpublikationen - noch nicht veröffentlicht worden ist sowie, dass ich eine solche Veröffentlichung vor Abschluss des Promotionsverfahrens nicht vornehmen werde. Die Bestimmungen der Promotionsordnung sind mir bekannt. Die von mir vorgelegte Dissertation ist von Prof. Dr. Alexander Altland betreut worden

_____
Ort, Datum

_____
Patrick Neven

Teilpublikationen:

- P. Neven, D. Bagrets and A. Altland
  Quasiclassical theory of disordered multi-channel Majorana quantum wires
  New Journal of Physics **15(5)** 055019 (2013)

- P. Neven, D. Bagrets and A. Altland
  Topological invariants in terms of quasiclassical Green's functions
  In Bearbeitung